Crystal stability and polymorphism of syndiotactic polystyrene from multiscale simulations

Chan Liu
Theory Group
Max Planck Institute for Polymer Research

Doctoral thesis
Max Planck Graduate Center
mit der Johannes Gutenberg-Universität Mainz

Mainz, 2019

Declaration of Authorship

I declare that the work presented here is original and the result of my own investigations. Formulations and ideas taken from other sources are cited as such.

It has not been submitted, either in part or whole, for a degree at this or any other university.

Location, Date

Signature

Abstract

Syndiotactic polystyrene (sPS) exhibits complex polymorphic behavior upon crystallization. Computational modeling of polymer crystallization has remained a challenging task because the relevant processes are slow on the molecular time scale. As such, a coarse-grained (CG) model is considered in this thesis to extend the range of accessible time and length scales. This CG model, parametrized in vacuum and validated in the melt, shows remarkable transferability properties in the crystalline phase. We performed parallel tempering simulations to compare the melting curve between CG and atomistic models. It shows that the transition temperature obtained from CG simulations is in good agreement with atomistic simulations. Remarkably, the CG model stabilizes the main α and β polymorphs, observed experimentally.

From several parallel tempering simulations, we compare in detail the propensity of polymorphs at the CG and AA level and discuss finite-size as well as box-geometry effects. It leads us to enlarge the simulation box to explore the relative stability of polymorphs without finite-size effects. However, the expected limitations of parallel tempering simulations are found in large systems, motivating us to apply another enhanced sampling method, Metadynamics.

With a proper choice of collective variables, Metadynamics simulations show extremely effective to overcome the barriers between different phases and observe the transitions among them. An efficient reweighting procedure is then applied for reconstructing the free energy surface from the Metadynamics simulations. The resulting free energy landscape helps us to discuss the relative stabilities of these metastable phases and observe the possible transition paths between them.

Contents

1. Background and Motivation

Syndiotactic polystyrene (sPS) has attracted both academic and industrial attention since three decades ago because of its extremely complex crystal polymorphism. *polymorphism* means the ability of a solid material to exist in more than one form or crystal structure. Different polymorphs can exhibit amazingly different properties, which makes the study of polymorphism interesting and essential.

Polymorphic material have several different metastable crystalline states, i.e., several local minima on free energy surface. In experiments, the formations and transitions between difference forms depend much on the experimental conditions and processes, making it difficult to measure their relative stabilities.

With computer simulations, researchers are able to screen a large number of polymorphs and make predictions for new polymorphs [1–3]. For polymeric materials, however, it is still hard to explore the free energy landscapes of polymorphs, since it involves much larger size and much higher barriers. To speed up the simulations and overcome the free energy barriers, we introduce Coarse-graining and enhanced sampling methods in our work. With these advanced methods, the relative stabilities of sPS crystal polymorphs can be explored.

1.1. Physical and theoretical concepts

Computer (molecular) simulations are powerful tools to study microscopic behavior of the system and link the thermodynamic quantities to appropriate averages over atomic details, which are based on the theories of thermodynamics and statistical mechanics.

Thermodynamics describes the thermal macroscopic behavior without atomic details, while statistical mechanics is a formalism to express the many microscopic degree of freedom of a thermal system in terms of few macroscopic quantities. Logically, the bottom-up link between atomic and macroscopic behavior would be in the following sequence [4]:

(i) describe atomic behavior on a quantum-mechanical basis;

(ii) simplify to classical behavior where possible;

(iii) apply statistical mechanics to average over details;

(iv) derive thermodynamics, quantities and phase behavior and other non-equilibrium behavior.

However, the historical development has followed a quite different sequence [4]. Equilibrium thermodynamics was first developed with the definition of entropy as a state function. At that time, no detailed knowledge of atomic interactions existed and thus no connection between atomic interactions and macroscopic behavior could be made.

With the concepts of atoms and molecules, equilibrium statistical mechanics was developed by Boltzmann and Gibbs as the main innovators. However, only after the completion of basic quantum mechanics around 1930, the proper link between microscopic properties and macroscopic thermodynamics was made. The classical statistical mechanics of Gibbs [5] is an approximation to quantum statistics.

1.1.1. Lagrangian and Hamiltonian mechanics

We first introduce classical mechanics, which can describe the motion of a many-body system, and clearly, is a foundation for classical statistical mechanics.

Consider a system described by n degrees of freedom with coordinates $q = q_1, \cdots, q_n$ that evolve in time t. The Lagrangian is defined as the kinetic energy minus the potential energy of the system [6]:

$$\mathcal{L} \equiv \mathrm{K}(\dot{q}) - \mathcal{U}(q), \tag{1.1}$$

where q and $\dot{q}$ are the generalized coordinates and their time derivatives.

The Lagrangian formulation of classical mechanics is based on an extremum principle, i.e., the actual trajectory follow a path for which the action is a minimum [7]:

$$S = \int \mathrm{d}t \mathcal{L}(q, \dot{q}). \tag{1.2}$$

With this principle, we can get the Lagrangian equation of motion:

$$-\frac{\mathrm{d}}{\mathrm{d}t}\left(\frac{\partial \mathcal{L}}{\partial \dot{q}}\right) + \frac{\partial \mathcal{L}}{\partial q} = 0. \tag{1.3}$$

The Hamiltonian formulation is derived from the Lagrangian equations:

$$\mathcal{H}(q, p) \equiv p\dot{q} - \mathcal{L}(q, \dot{q}, t). \tag{1.4}$$

$\mathcal{H}$ is a function of q, p and also of time t.

Instead of a single second-order equation for the coordinates q only, the Hamiltonian

yields two first-order differential equations in terms of q and its conjugate momentum p:

$$\frac{\partial \mathcal{H}}{\partial p} = \dot{q} \tag{1.5}$$

$$\frac{\partial \mathcal{H}}{\partial q} = -\dot{p}. \tag{1.6}$$

In Cartesian coordinates, the Hamiltonian can be written as

$$\mathcal{H}(x, p_x) = \frac{1}{2m} p_x^2 + \mathcal{U}(x). \tag{1.7}$$

and the Hamiltonian equations of motion reduce to Newton's equations

$$\dot{x} = \frac{\partial \mathcal{H}}{\partial p_x} = \frac{p_x}{m} \tag{1.8}$$

$$\dot{p}_x = -\frac{\partial \mathcal{H}}{\partial x} = -\frac{\partial \mathcal{U}(x)}{\partial x}, \tag{1.9}$$

or

$$m\ddot{x} = -\frac{\partial \mathcal{U}(x)}{\partial x}. \tag{1.10}$$

In this case, we can conclude a fact that $\mathcal{H}$ is the total energy of the system of particles, composed of the kinetic energy and the potential energy:

$$\mathcal{H} = \mathrm{K} + \mathcal{U}. \tag{1.11}$$

We know these two formulations of classical mechanics can all yield Newton's equations. This is not surprising as the Hamiltonian formulation was derived from the Lagrangian equations. However, this Hamiltonian expressions can be used to establish the connection with statistical mechanics (see equation 1.27 in Section 1.1.3).

1.1.2. Thermodynamics

In thermodynamics, equilibrium implies reversibility of processes [4]. Processes that occur so slowly that in all intermediate states the system can be assumed to be in equilibrium are called reversible.

However, processes that involve changes of state or constitution cannot take place in equilibrium and always involve some degree of irreversibility. In fact, the second law of thermodynamics makes a qualitative statement about the direction of processes: a system will spontaneously evolve in the direction of increasing excess entropy. This describes non-

equilibrium processes.

Now, firstly, we consider thermodynamics of equilibrium systems. Here we need to introduce some state functions. State functions are properties of the system that depend only on the state of the system and not on its history. State functions are extensive if they are proportional to the size of the system, while intensive state functions are independent of the system size. Volume V is an extensive state function, while pressure p and temperature T are two important intensive state functions.

A thermodynamic system may exchange heat $\mathrm{d}q$, work $\mathrm{d}w$.

$$\mathrm{d}V = -\frac{\mathrm{d}w}{p} \tag{1.12}$$

$$\mathrm{d}S = \frac{\mathrm{d}q}{T} \tag{1.13}$$

The function S is called the entropy, which is an extensive state function. Neither $\mathrm{d}q$ nor $\mathrm{d}w$ is an exact differential: it is possible to extract net heat or work over a closed reversible path. However, $-1/p$ is an integrating factor of $\mathrm{d}w$, yielding the exact differential $\mathrm{d}V$. Similarly, $1/T$ is an integrating factor of $\mathrm{d}q$.

The first law of thermodynamics is the conservation of energy. If the number of particles and the composition does not change, the change in internal energy $\mathrm{d}U$ is due to absorbed heat $\mathrm{d}q$ and to work exerted on the system $\mathrm{d}w$. Hence

$$\mathrm{d}U = T\mathrm{d}S - p\mathrm{d}V. \tag{1.14}$$

Here we show some other important differential relations, like enthalpy:

$$\mathrm{d}H = T\mathrm{d}S + V\mathrm{d}p, \tag{1.15}$$

Helmholtz free energy:

$$\mathrm{d}F = -S\mathrm{d}T - p\mathrm{d}V, \tag{1.16}$$

Gibbs free energy:

$$\mathrm{d}G = -S\mathrm{d}T + V\mathrm{d}p, \tag{1.17}$$

where U, H, F, G are all extensive state functions.

So far we have used the second law of the thermodynamics in the form $\mathrm{d}S = \mathrm{d}q/T$, valid for the systems in equilibrium. However, the full second law include non-equilibrium states:

$$\mathrm{d}S \geq \frac{\mathrm{d}q}{T} \tag{1.18}$$

This qualitative law can be formulated for closed systems for three different cases:

1. In canonical (NVE) system: when neither material nor heat is exchanged with the en-

vironment ($\mathrm{d}q = 0$), the system will spontaneously evolve in the direction of the maximum entropy:

$$\mathrm{d}S \geq 0. \tag{1.19}$$

In equilibrium S is a maximum.

2. In NVT system: when volume and temperature are kept constant ($\mathrm{d}V = 0, \mathrm{d}T = 0$), then $\mathrm{d}q = \mathrm{d}U$ and $T\mathrm{d}S \geq \mathrm{d}U$. This implies that

$$\mathrm{d}F \leq 0. \tag{1.20}$$

The system will spontaneously evolve in the direction of the lowest Helmholtz free energy. In equilibrium F is a minimum.

3. In NPT system: when pressure and temperature are kept constant ($\mathrm{d}p = 0, \mathrm{d}T = 0$), then $\mathrm{d}q = \mathrm{d}H$ and $T\mathrm{d}S \geq \mathrm{d}H$. This implies that

$$\mathrm{d}G \leq 0. \tag{1.21}$$

The system will spontaneously evolve in the direction of the lowest Gibbs free energy. In equilibrium G is a minimum.

1.1.3. Statistical mechanics

Statistical mechanics [5] considers a hypothetical ensemble of a large number of replicas of the system, with the same thermodynamic conditions but different microscopic details. Properties are then obtained by averaging over the ensemble, which is supposed to contain all possible states of the system and be representative for the single system considered over a long time. This latter assumption is the "ergodic" postulate. However, whether a realistic system is "ergodic" is usually a matter of time scale in practice. In many examples of systems, like metastable phases, processes may be so slow that not all possibilities are realized in the observation time. Then the system is not "ergodic" and in fact not in complete equilibrium.

Consider a canonical ensemble of systems with given number of particles and fixed volume, and we assume that the system have ergodic behavior. The system is completely determined by its microstates labeled i with energy E_i, and its thermodynamic state is determined by the probability distribution $\{w_i\}$. Then, what is the most likely distribution of the $\{w_i\}$? We know that all possible ways to realize the ensemble are equally probable. Therefore the most likely distribution of $\{w_i\}$ is the one that maximizes the function

$$H = -\langle \ln w_i \rangle. \tag{1.22}$$

where the $\langle\cdot\rangle$ denote ensemble average. Note that $\sum_i w_i = 1$, hence

$$H = -\frac{\sum_i w_i \ln w_i}{\sum_i w_i} = -\sum_i w_i \ln w_i. \tag{1.23}$$

This function is equivalent to Shannon's definition of information or uncertainty over a discrete probability distribution [8].

The distribution with maximal H depends on the equilibrium conditions, which suggests that the H-function is somehow related to the thermodynamics entropy S of the system, since the second law of thermodynamics states that the entropy of a canonical system is at its maximum when the system is in thermal equilibrium (See equation 1.19). In fact the entropy is proportional to H [4]:

$$S = -k_B \langle \ln w_i \rangle = -k_B \sum_i w_i \ln w_i, \tag{1.24}$$

where k_B is Boltzmann's constant, 1.38066×10^{-23} J/K.

Using the method of Lagrange multipliers, the maximum equilibrium conditions can yield [4]:

$$w_i = \frac{1}{Q} e^{-\beta E_i} \quad \text{or} \quad w_i \propto e^{-\beta E_i} \tag{1.25}$$

where $\beta = 1/k_B T$ and $Q = \sum_i e^{-\beta E_i}$.

Further, one can obtain the relation between Q and the Helmholtz free energy:

$$F = -k_B T \ln Q = -k_B T \ln \left(\sum_i \exp(-E_i/k_B T) \right). \tag{1.26}$$

This relation is often more convenient to use than the relation between the entropy and the expectation of $\ln w_i$ (Equation 1.24). These two are the fundamental relations that couple statistical mechanics and thermodynamics.

In fact, we can have a classical approximation for this function Q:

$$\begin{aligned} Q^{\text{classical}} &= \frac{1}{N! h^{3N}} \int \mathrm{d}\mathbf{p}^N \mathrm{d}\mathbf{r}^N e^{-\beta \mathcal{H}(\mathbf{p},\mathbf{r})} \\ &= \frac{1}{N! h^{3N}} \int \mathrm{d}\mathbf{p}^N \mathrm{d}\mathbf{r}^N \exp\left\{ -\beta \left[\sum_i p_i^2/(2m_i) + \mathcal{U}(\mathbf{r}^N) \right] \right\}, \end{aligned} \tag{1.27}$$

where h is Planck's constant.

From it, we can get the classical expression for the thermal average of the observable A

as

$$\begin{aligned}\langle A\rangle &= \frac{\mathrm{Tr}\exp(-\beta\mathcal{H})A}{\mathrm{Tr}\exp(-\beta\mathcal{H})} \\ &= \frac{\int \mathrm{d}\mathbf{p}^N\mathrm{d}\mathbf{r}^N \exp\left\{-\beta\left[\sum_i p_i^2/(2m_i)+\mathcal{U}(\mathbf{r}^N)\right]\right\} A(\mathbf{p}^N,\mathbf{r}^N)}{\int \mathrm{d}\mathbf{p}^N\mathrm{d}\mathbf{r}^N \exp\left\{-\beta\left[\sum_j p_j^2/(2m_j)+\mathcal{U}(\mathbf{r}^N)\right]\right\}}.\end{aligned} \tag{1.28}$$

Equation 1.27 and 1.28 are the starting point for the application of statistical mechanics to systems of particles that follow classical equations of motions. Molecular Dynamics simulations used in our work is one example of the application, which will be introduced in Section 1.2.

1.1.4. Free energy and potential of mean force

In fact, in the applications of thermodynamics, free energy is much more important than energy. Because it determines phase equilibria, such as melting and boiling points, conformational changes. Generally, it is much more difficult to derive free energy differences than energy differences. The reason is that free energy incorporates an entropic term $-TS$; entropy is given by an integral over phase space, while energy is an ensemble average. In principle, free energy can be evaluated directly from completely equilibrated ensembles that contain all accessible regions of configurational space. In practice, however, there are two kinds of free energies we can calculate.

One of these quantities is the free energy of thermodynamic states, where the configurational space is subdivided into substates. The free energy of each state is determined by the number of configurations observed in each substate. Now, consider a system that can undergo a slow reversible reaction, and in the observation time is either in R state or in P state. Hence in the complete free energy landscape, there are two local minima for R and P, separated by a barrier large enough to observe each state as metastable equilibrium. From Section 1.1.3 (Equation 1.26), we know that

$$F = -k_B T \ln Q, \tag{1.29}$$

with

$$Q = c\int e^{-\beta U(\mathbf{r})}\mathrm{d}\mathbf{r}, \tag{1.30}$$

where the integration is carried out for all particle coordinates over all space, and $c = \frac{1}{N!h^{3N}}$. Thus the free energy difference between them is

$$\Delta F = -k_B T\ln(Q^R/Q^P) = -k_B T \ln\left(\frac{\int_R e^{-\beta U(\mathbf{r})}\mathrm{d}\mathbf{r}}{\int_P e^{-\beta U(\mathbf{r})}\mathrm{d}\mathbf{r}}\right), \tag{1.31}$$

where the integrations are now carried out over the parts of configuration space defined as the R and P regions, respectively.

We know that $Q = Q^R + Q^P$, but $F \neq F^R + F^P$, instead[4],

$$F = w^R F^R + w^P F^P + k_B T(w^R \ln w^R + w^P \ln w^P) \tag{1.32}$$

where $w^R = Q^R/Q$ and $w^P = Q^P/Q$. The latter term is due to the mixing entropy resulting from the distribution of the system over two states.

Another is free energy in a restricted space as a function of one or more defined parameters, which are functions of coordinates, often called "reaction coordinates" or "collective variables" (in enhanced sampling methods, see Section 1.2.3). Here, we note $\xi(\mathbf{r})$ as a function of $\mathbf{r}$, which can connect the R and P regions of configuration space (see Figure 1.1). Then we can integrate over this reaction coordinate to get the partition function Q:

$$Q = c \int \mathrm{d}\xi \int \mathrm{d}\mathbf{r} e^{-\beta U(\mathbf{r})} \delta(\xi(\mathbf{r}) - \xi), \tag{1.33}$$

Now define the potential of mean force (PMF) $U_{\mathrm{PMF}}(\xi)$ as [4]

$$U_{\mathrm{PMF}}(\xi) \equiv -k_B T \ln \left[c \int \mathrm{d}\mathbf{r} e^{-\beta U(\mathbf{r})} \delta(\xi(\mathbf{r}) - \xi) \right], \tag{1.34}$$

so that

$$Q = \int e^{-\beta U_{\mathrm{PMF}}(\xi)} \mathrm{d}\xi \tag{1.35}$$

and

$$F = -k_B T \ln \left[\int e^{-\beta U_{\mathrm{PMF}}(\xi)} \mathrm{d}\xi \right]. \tag{1.36}$$

Thus the potential of mean force is an integral over multidimensional hyperspace.

From Equation 1.36, once the PMF is known, the free energy of a thermodynamic state can be computed by integration over the relevant part of the reaction coordinate. Thus the PMF can be seen as a free energy for the system including the reaction coordinates as degrees of freedom.

From Figure 1.1, we know that the local minima in the free energy landscape are metastable equilibrium states. Also, free energy can measure the energetic cost of a maximally efficient transition from one region to another.

1.2. Computer simulations

Computer simulations have changed the way in which we construct new theories. The simulations can give us a feeling for the physics of the problem and offer results to test

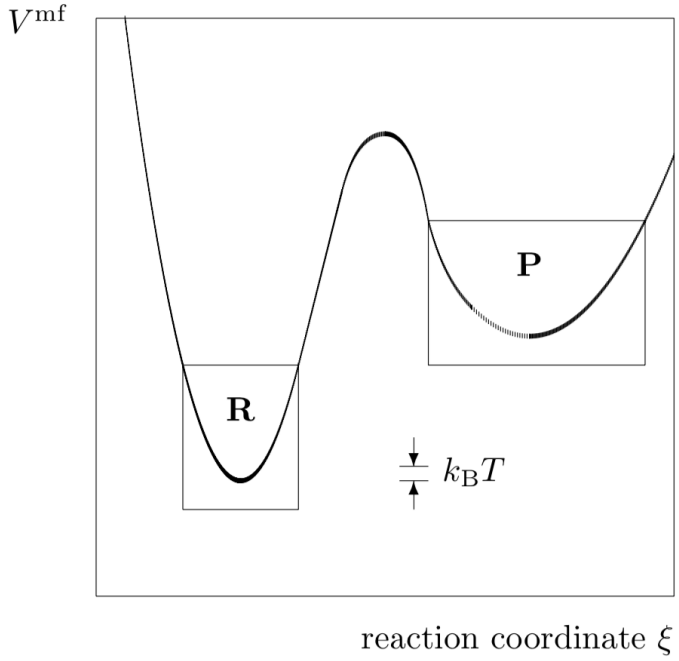

Figure 1.1.: Potential of mean force U_{PMF} in one "reaction coordinate" ξ. There are two regions of configurational space R and P, i.e. two thermodynamic states. Reprinted from [4] with permission of The Licensor through PLSclear(15851).

the quality of the theory to be constructed. Besides, the simulation can help guide experimental work and assist in the interpretation of new results in experiments.

For instance, the traditional approach to study the mechanical properties of materials is based on macroscopic continuum-mechanics theories by classifying the types of macroscopic response for materials [9]. However, these final macroscopic properties of real materials, especially for extremely complex polymeric materials, are determined by microstructural evolution and processing history [10]. To get a deeper understanding for the structure-property relations, one should trace back to atomic scale. Figure 1.2 [11] shows several simulation models at various length scales, which can be used for polymer research. These scales range from Angstroms and picoseconds for the vibrations of atomic bonds up to millimeters and seconds for crack propagation in polymer composites. The basic degrees of freedom used in these models are electrons (quantum chemistry), atoms (atomistic models), groups of atoms (coarse-grained models), entire polymer chains (soft fluids) and volume elements (finite elements).

All these methods have been applied to polymers, with some success but also limitation on their involving scale. The connectivity in a polymer molecule enforces an interdependence between features on different scales. As a consequence, many polymer properties cannot be viewed on one length scale alone. Therefore, it becomes highly desirable to develop multiscale methods [10–14] to bridge these different scales. In our work, we will focus on

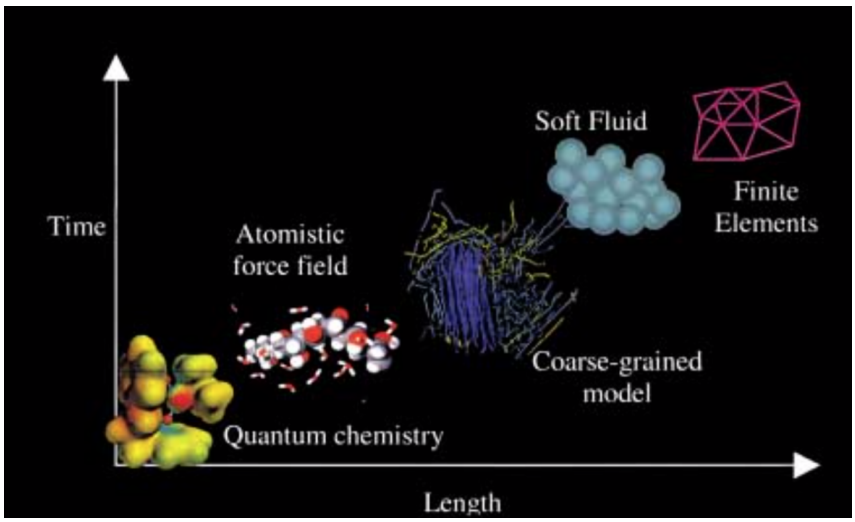

Figure 1.2.: Length scales, associated time scales and computational methods in polymer simulation. Reprinted from [11] with permission of The Licensor through RightsLink(4618950245585).

using molecular dynamics simulations (involving atomistic and coarse-grained models) to study the crystallization and polymorphism of polymeric systems.

1.2.1. Molecular Dynamics simulations

Molecular Dynamics (MD) simulation is a particle-based method, which can simulate the motion of particles (atoms or CG beads) based on classical mechanics, and then study properties of many-body systems based on statistical mechanics.

A general procedure for MD simulations is [15]:

1. Read in the parameters that specify the conditions of the run (e.g., initial temperature, number of particles, density, time step).

2. Initialize the system (i.e., we select initial positions and velocities).

3. Compute the forces on all particles.

4. Integrate Newton's equations of motion. Repeat until the time evolution of the system reach the desired length of time.

5. After completion of the central loop, compute and print the averages of measured quantities, and stop.

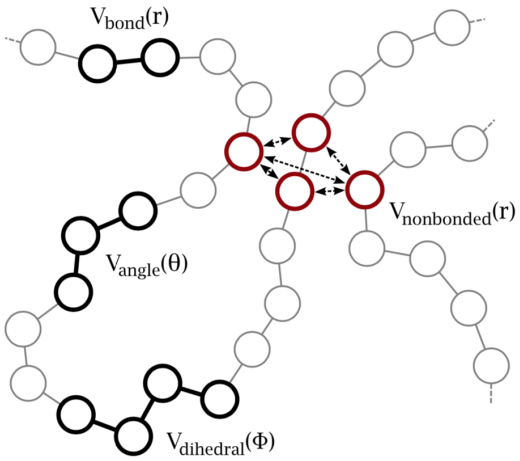

Figure 1.3.: Schematic view of force field terms for a system of linear chain molecules: bonded potentials act on groups of two (bonds), three (angles) or four (dihedrals) neighbors connected by chemical bonds; nonbonded potentials act on particles, which are close to each other in space, but not involved in a joint bonded interaction. This scheme holds for coarse-grained force fields (will be introduced in Section 1.2.2), but it also works for atomistic force fields.

Force fields

To start the simulation, we should assign initial positions and velocities to all particles in the system, and then calculate the force acting on every particle, which is the most time-consuming part of almost all MD simulations. We have to consider the contributions to the force on particle i due to all its neighbors. Here force fields are applied to describe these contributions as functions of the positions of particles, and in polymeric system, which are often separated into bonded and nonbonded interactions, shown in Figure 1.3. The difference between these two types in computation is that bonded interactions apply to intramolecular particles, which is read from the fixed bonded list, whereas pairs of particles involved in nonbonded interactions are intermolecular, whose neighbor list change with time and have to be updated regularly.

In atomistic models, bonded interactions are usually characterized by specific bond lengths r, angles θ, and torsions ϕ between pair, triple and quadruple of atoms respectively. Their potential functions are as follows:

$$U_b(r_{ij}) = \frac{1}{2}k_b(r_{ij} - b_0)^2 \tag{1.37}$$

$$U_a(\theta_{ijk}) = \frac{1}{2}k_\theta(\theta_{ijk} - \theta_0)^2 \tag{1.38}$$

$$U_d(\phi_{ijkl}) = k_\phi(1 + \cos(n\phi - \phi_s)) \tag{1.39}$$

The nonbonded interactions are pairwise additive and a function of the distance r_{ij} between the two atoms of each pair. Pairs that are involved in bonded interactions are usually excluded from the nonbonded interactions. Two types of nonbonded interactions are used in atomistic models: Lennard-Jones interactions and Coulomb interactions, and they are described as follows:

$$U_{LJ}(r_{ij}) = 4\epsilon_{ij}\left[\left(\frac{\sigma_{ij}}{r_{ij}}\right)^{12} - \left(\frac{\sigma_{ij}}{r_{ij}}\right)^{6}\right] \tag{1.40}$$

$$U_C(r_{ij}) = \frac{1}{4\pi\varepsilon_0}\frac{q_i q_j}{r_{ij}} \tag{1.41}$$

Integrating Newton's equations of motion

After computing all forces between the particles based on these potential functions, we can integrate Newton's equations of motion.

One important property of a Hamiltonian system is that the natural time evolution satisfies the symplectic condition [16]. True Hamiltonian dynamics leaves the magnitude of any volume element in phase space unchanged. Moreover, the number of phase-space points inside any volume does not change in time, i.e., the phase-space density is constant, behaving like an incompressible fluid. Hence, to solve Newton's equations of motion, "good" algorithms should be area preserving. Many numerical schemes, in particular those that are not time reversible, do not reproduce this area-preserving property. Those non-area-preserving algorithms will greatly expand the volume of our system after sufficiently long times, which will lead to serious long-term energy drift problems. However, it should be noted that the symplectic condition implies more than just the area-preserving properties, and a "good" algorithm should really satisfy the symplectic condition.

Fortunately, we can check this by a fact that an algorithm that can be written as a sequence of exact time evolutions generated by simple Hamiltonians is necessarily simplectic [17]. An example is the Verlet algorithm [18]. This family of algorithms is simple, robust, time-reversible and symplectic. To derive it, we start with a Taylor expansion of the coordinate of a particle, around time t:

$$r(t + \Delta t) = r(t) + v(t)\Delta t + \frac{f(t)}{2m}\Delta t^2 + \frac{\Delta t^3}{3!}\dddot{r} + \mathcal{O}(\Delta t^4), \tag{1.42}$$

and

$$r(t - \Delta t) = r(t) - v(t)\Delta t + \frac{f(t)}{2m}\Delta t^2 - \frac{\Delta t^3}{3!}\dddot{r} + \mathcal{O}(\Delta t^4). \tag{1.43}$$

Summing these two equations, we obtain

$$r(t+\Delta t)+r(t-\Delta t)=2r(t)+\frac{f(t)}{m}\Delta t^2+\mathcal{O}(\Delta t^4), \tag{1.44}$$

then

$$r(t+\Delta t)\approx 2r(t)-r(t-\Delta t)+\frac{f(t)}{m}\Delta t^2. \tag{1.45}$$

The Verlet algorithm does not use the velocity to compute the new position. However, the velocity can be derived from knowledge of the trajectory:

$$r(t+\Delta t)-r(t-\Delta t)=2v(t)\Delta t+\mathcal{O}(\Delta t^3). \tag{1.46}$$

$$v(t)=\frac{r(t+\Delta t)-r(t-\Delta t)}{2\Delta t}+\mathcal{O}(\Delta t^2). \tag{1.47}$$

Several algorithms are equivalent to the Verlet scheme. The simplest among these is the so-called Leap-frog algorithm [19]. This algorithm evaluates the velocities at half-integer time steps and uses these velocities to compute the new positions:

$$v(t+\Delta t/2)=v(t-\Delta t/2)+\frac{f(t)}{m}\Delta t. \tag{1.48}$$

$$r(t+\Delta t)=r(t)+v\Delta t(t+\Delta t/2). \tag{1.49}$$

In comparison to the Verlet algorithm, the Leap-frog algorithm has the advantage that the velocities explicitly appear in the integration scheme, which allows for a coupling of the system to a thermal bath. This Leap-frog algorithm is the default MD integrator in GROMACS [20]. However, the velocities are not defined at the same time as the positions, and hence we cannot directly compute the total energy in the Leap-frog scheme.

Another algorithm implemented in GROMACS is the velocitity-Verlet algorithm [21], where velocities at the previous half step are not required. From Equation 1.48 in Leap-frog algorithm, we can get

$$v(t+\Delta t/2)=v(t)+\frac{f(t)}{2m}\Delta t. \tag{1.50}$$

and

$$v(t+\Delta t)=v(t+1/2\Delta t)+\frac{f(t+\Delta t)}{2m}\Delta t. \tag{1.51}$$

Then we can get the update of the velocities without the half step:

$$v(t+\Delta t)=v(t)+\frac{f(t+\Delta t)+f(t)}{2m}\Delta t, \tag{1.52}$$

and the update of the positions which just looks like a Taylor expansion:

$$r(t+\Delta t) = r(t) + v\Delta t(t+\Delta t/2) = r(t) + v(t)\Delta t + \frac{f(t)}{2m}\Delta t^2. \tag{1.53}$$

However in velocity-Verlet algorithm, we can compute the new velocities only after we have computed the new positions and the new forces.

Note that other higher-order algorithms are quite accurate for short time, however, they can make the unavoidable exponential error for long times. They are neither time-reversible nor symplectic. Although the Verlet-style algorithm does not conserve the total energy of this system exactly, it does conserve a pseudo-Hamiltonian approaching the true Hamiltonian in the limit of infinitely short time steps due to its time-reversible, area-preserving and symplectic properties.

Temperature and pressure coupling

When we discuss the basic theories for MD in Section 1.1.3, we consider a canonical ensemble. In fact, it is often more convenient to perform simulations in NVT or NPT ensembles. For studying crystallization and polymorphism, we usually use NPT ensembles. To perform MD simulations in ensembles other than the canonical, there are two different solutions. One is mixing Newtonian MD with certain Monte Carlo moves; another one is reformulating the Lagrangian equations of motion of the system.

In the constant-temperature method proposed by Andersen [22], the system is coupled to a heat bath that imposes the desired temperature. The coupling to a heat bath is represented by stochastic impulsive forces that act occasionally on randomly selected particles. These stochastic collisions with the heat bath can be considered as Monte Carlo moves that transport the system from one constant-energy shell to another. Between stochastic collisions, the system evolves at constant energy according to the normal Newtonian laws of motion. Andersen algorithm is proven to indeed generate a canonical distribution [22], however, the dynamics generated by the Andersen thermostat is unphysical with Monte Carlo moves. Therefore, it is risky to use the Andersen method when studying dynamical properties.

Unlike Andersen thermostat, Nose approach [23] is based on the clever use of an extended Lagrangian, which can lead deterministic MD at constant temperature. To construct isothermal MD, Nose introduce an additional coordinate s in the Lagrangian of a classical N-body system:

$$\mathcal{L}_{\text{Nose}} = \sum_{i=1}^{N} \frac{m_i}{2} s^2 \dot{\mathbf{r}}_i^2 - \mathcal{U}(\mathbf{r}^N) + \frac{Q}{2}\dot{s}^2 - \frac{L}{\beta}\ln s, \tag{1.54}$$

where Q is an effective "mass" associated to s, and $L = 3N$. Then we can express the

Hamiltonian of the extended system as

$$\mathcal{H}_{\text{Nose}} = \sum_{i=1}^{N} \frac{\mathbf{p}_i^2}{2m_i s^2} + \mathcal{U}(\mathbf{r}^N) + \frac{p_s^2}{2Q} + L\frac{\ln s}{\beta}. \tag{1.55}$$

Now, introduce $\mathbf{p}' = \mathbf{p}/s$ as the real momentum, while $\mathbf{p}$ is interpreted as a virtual momentum. For other variables, we have $r' = r, s' = s, \Delta t' = \Delta t/s$, and thus s can be interpreted as a scaling factor of the time step. This implies that the real time step fluctuates during a simulation.

Then we get the following conserved quantity:

$$H'_{\text{Nose}} = \sum_{i=1}^{N} \frac{\mathbf{p}_i'^2}{2m_i} + \mathcal{U}(\mathbf{r}'^N) + \frac{s'^2 p_s'^2}{2Q} + L\frac{\ln s'}{\beta}. \tag{1.56}$$

To simplify the Nose equations, Hoover [24] introduced the thermodynamic friction coefficient $\xi = s'p'_s/Q$, leading to H_{Nose}:

$$H_{\text{Nose}} = \sum_{i=1}^{N} \frac{\mathbf{p}_i^2}{2m_i} + \mathcal{U}(\mathbf{r}^N) + \frac{\xi^2 Q}{2} + L\frac{\ln s}{\beta}. \tag{1.57}$$

Note that the logarithmic term $\ln s$ is important to make the Lagrangian have the correct scaling of time, and thus make this approach describe the canonical ensemble correctly.

Most experiments are performed at constant pressure instead of constant volume. To simulate at constant pressure, the volume is considered as a dynamical variable that changes during the simulation. In the same spirit as the temperature coupling, the system can also be coupled to a pressure bath.

GROMACS supports the Berendsen algorithm [25] that scales coordinates and box vectors every step. The Berendsen pressure control algorithm can yield a simulation with the correct average pressure, but it does not yield the exact NPT ensemble.

Another approach for constant-pressure simulations is called Parrinello-Rahman [26], which is similar to the Nose-Hoover temperature coupling, and in theory gives the true NPT ensemble. With the Parrinello-Rahman barostat, the box vectors as represented by the matrix obey the matrix equation of motion:

$$\frac{\mathrm{d}\mathbf{b}^2}{\mathrm{d}t^2} = V\mathbf{W}^{-1}\mathbf{b}'^{-1}(\mathbf{P} - \mathbf{P}_{\text{ref}}), \tag{1.58}$$

where $\mathbf{W}$ is a matrix parameter that determines the strength of the coupling; $\mathbf{P}$ and $\mathbf{P}_{\text{ref}}$ are the current and reference pressures, respectively.

Just like the Nose-Hoover thermostat, the Parrinello-Rahman time constant is not equivalent to the relaxation time used in the Berendsen pressure coupling algorithm. In most cases, one should use a 4–5 times larger time constant with Parrinello-Rahman coupling. If the system is far from equilibrium, the Parrinello-Rahman coupling may result in large box oscillations and crash in the end. In that case, one should increase the time constant, or better use the weak-coupling scheme to reach the target pressure, and then switch to Parrinello-Rahman coupling once the system is in equilibrium.

Periodic boundary conditions

In our work, we are interested in bulk behavior of systems whose surface-to-volume ratio should be sufficiently small to not significantly affect the observed properties. In simulations, the traditional way to minimize the surface effects in a finite system is to apply periodic boundary conditions, where the system is exactly replicated in three dimensions. Thus there are no boundaries of the system, and the simulated system is a unit cell of a periodic lattice.

Using periodic boundary conditions in simulations, we should combine it with the "minimum image convention": Only one image of each particle in the periodic boundary conditions is considered for a pair interaction, where the distance is a minimum over all images. In this case, we need to make sure that the nonbonded interaction has a cut-off which cannot exceed half the box size. In fact, this modification of nonbonded potentials can cause its own artifacts. Sudden jump cutoffs will cause additional noise, while smooth cutoffs can strongly modify the interaction. Thus how to correct the influence of the cutoff need to be considered when developing force fields.

On the other hand, while periodic boundary conditions avoid the artifact from unwanted boundaries in an isolated cluster, they introduce the artifact of periodicity. In periodic boundary conditions each atom interacts not only with atoms in the same unit cell, but also with images of all the cells, including its own periodic images. For large systems, the errors are small, but for small systems with a large number of internal spatial correlation, the periodic boundaries will probably generate more artifacts.

1.2.2. Coarse-graining methods

Nowadays computer simulations on an atomistic level have brought new insight into phenomena on the molecular scale. However for polymeric systems, many processes, like crystallization, occur on length and time scales that are beyond the reach of current detailed atomistic simulations. A common way of addressing this issue is to simplify the system, merging groups of chemically connected atoms into coarse-grained (CG) 'sites" or "superatoms" [27]. The averaged-out detailed degrees of freedom are considered to

be unimportant for properties of interest. These approaches employ information from a more detailed model are called "bottom-up" coarse-graining [28].

In MD simulations, we naturally focus on particle-based, off-lattice CG models. To increase the length and time scales accessible by simulations, CG models have proven to be very efficient. The degree of coarse-graining, i.e., the number of real atoms represented by one CG site, can range from a few beads per monomer up to one bead for many monomers or an elipsoid for a whole chain. The choice of the proper model should be based on the problem considered. Clearly, the smaller the number of atomistic particles being coarse-grained, the less the advantages over the detailed atomistic approaches. If one coarses too many atoms, however, the mesoscopic model will not be capable of describing properties related to details of the local packing.

With the CG mapping, the configuration $\mathbf{R}$ of CG model is determined as a function of the configuration $\mathbf{r}$ of an underlying atomistic model.

$$\mathbf{R}_I = M_I(\mathbf{r}) = \sum_i c_{Ii}\mathbf{r}_i, \tag{1.59}$$

where c_{Ii} are coefficients corresponding to the center of mass or geometry for the associated atomic group.

After determining the CG representation of a particular system, the remaining challenge is to determine the appropriate interactions between the CG sites. The interactions in the CG model should reflect the "correct physics" so that the model is not only highly efficient, but also provides accurate predictions. In many approaches, the approximate CG potential $U(\mathbf{R})$ adopts a similar form to atomistic model, in which each bond, angle, torsion, and pair nonbonded interaction is modeled. This can be represented by [29]

$$U(\mathbf{R}) = \sum_\zeta \sum_\lambda U_\zeta(\psi_\zeta(\mathbf{R}_\lambda)) \tag{1.60}$$

where ζ identifies a particular type of interaction, and ψ_ζ is a scalar variable for a particular set λ. For instance, if ζ corresponds to a type of nobonded pair interaction, then U_ζ is the corresponding pair potential, ψ_ζ is a pair distance for a particular pair of sites.

In fact, the CG potential can also be expressed as [30]

$$U(\mathbf{R}) = \sum_\zeta \int \mathrm{d}x\ U_\zeta(x)\hat{\rho}_\zeta(\mathbf{R}; x), \tag{1.61}$$

where

$$\hat{\rho}_\zeta(\mathbf{R}; x) = \sum_\lambda \delta(\psi_{\zeta\lambda}(\mathbf{R}) - x), \tag{1.62}$$

Then with this potential, the CG force field can be expressed as [31]

$$\mathbf{F} = \sum_{\zeta} \int \mathrm{d}x \phi_{\zeta}(x) \boldsymbol{\mathcal{G}}_{\zeta}(x) \tag{1.63}$$

where $\phi_{\zeta}(x) = -\mathrm{d}U_{\zeta}(x)/\mathrm{d}x$ and $\boldsymbol{\mathcal{G}}$ is a basis vector that defines the direction of forces generated by $U_{\zeta}(x)$.

Usually, CG potentials are derived to reproduce a target structural correlation function (structure-based) or a target force distribution (force-based) calculated from atomistic simulations. The densities $\hat{\rho}_{\zeta}$ and corresponding force field vectors $\boldsymbol{\mathcal{G}}_{\zeta}$, mentioned above, act as basis vectors for structure- and force-motivated approaches, respectively.

Structure-based method

Structure-based method consider a CG model to be consistent with a particular atomistic model for the same system when the two models sample the same distribution of configurations in the CG configuration space [32]:

$$P_R(\mathbf{R}) = p_R(\mathbf{R}), \tag{1.64}$$

where $p_R(\mathbf{R})$ is the probability distribution calculated from atomistic simulations:

$$p_R(\mathbf{R}) = \langle \delta(\mathbf{M}(\mathbf{r}) - \mathbf{R}) \rangle, \tag{1.65}$$

and $P_R(\mathbf{R})$ is determined by CG potential $U(\mathbf{R})$:

$$P_R(\mathbf{R}) \propto \exp\left[\frac{-U(\mathbf{R})}{k_B T}\right]. \tag{1.66}$$

In fact, it is unclear whether there exist exact potentials that will reproduce these target structural correlation functions. But from the Henderson theorem [33], if these potentials exist, they should be unique. Consequently, the appropriate potential for a consistent CG model is uniquely determined by the probability distribution p_R:

$$U^0(\mathbf{R}) = -k_B T \ln p_R(\mathbf{R}) + \text{const.} \tag{1.67}$$

From Equation 1.34 in Section 1.1.4, we know that the potential U^0 is a many-body potential of mean force (PMF). Then the force field generated from this potential, named as many-body mean force (MF), may be expressed as a conditioned canonical ensemble average of the atomistic forces:

$$\mathbf{F}_I^0(\mathbf{R}) = \langle \mathbf{f}_I(\mathbf{r}) \rangle_{\mathbf{R}}, \tag{1.68}$$

where $\mathbf{f}_I(\mathbf{r})$ is net "atomistic force" on site I in configuration $\mathbf{r}$.

We know that the many-body PMF is not a conventional potential energy function, but should more properly be considered a configuration-dependent free energy that contain not only energetic, but also entropic effects. However, this PMF is a many-body potential since it is determined from a many-body distribution function, and generally, it cannot be readily decomposed into simpler independent factors.

Consequently, we approximate the CG potential into a sum of different simple type of interactions, as Equation 1.60. For structure-based methods, that means we should reproduce the correlation functions separately, i.e., $p_\zeta(x)$. For a particular interaction ζ, we have

$$U_\zeta^0(x) = -k_B T \ln p_\zeta(x). \tag{1.69}$$

Strictly speaking, the PMF for a particular correlation cannot be directly used as a potential energy function for the corresponding interaction. In some cases, however, it can be a good approximation, if the free energy of this interaction is dominated by the energy and so the entropy could be neglected. The method using this equation directly is called Direct Boltzmann Inversion [34].

In more complex systems, however, the Direct Boltzmann Inversion will fail to reproduce the target structural distributions. Then performing a simulation with this potential $U_\zeta^0(x)$, it will yield a corresponding $P_\zeta^0(x)$, which is different from the target $p_\zeta(x)$. Hence to reproduce a particular correlation more accurately, we usually use Iterative Boltzmann Inversion (IBI) method [35], which employ iterative nonlinear optimization techniques to systematically refine the CG potential. In IBI method, $U_\zeta^0(x)$ is served as the initial guess for the iterative procedure. Then the potential can be refined iteratively with a correction proportional to the difference:

$$U_\zeta^{i+1}(x) = U_\zeta^i(x) - k_B T \ln \left(\frac{P_\zeta^i(x)}{p_\zeta(x)} \right). \tag{1.70}$$

It usually takes less than ten iterations before reproducing a target $p_\zeta(x)$ within an acceptable error.

Force-based method

The second group of CG methods is "Force-Matching" (FM) method, based on the idea of matching the force distributions on the CG beads with the ones on the mapping points. This method was first reported [36] to build realistic effective force fields for atomistic systems from ab initio calculations. Then the FM method was further extended to derive realistic CG force fields from the underlying atomistic forces, named as "Multiscale Coarse-grained" (MS-CG) approach [37, 38].

The MS-CG method directly determines an approximate potential by minimizing the force-matching functional, $\chi^2[U]$:

$$\chi^2[\mathbf{F}] = \frac{1}{3N}\left\langle \sum_I |\mathbf{f}_I(\mathbf{r}) - \mathbf{F}_I(\mathbf{M}(\mathbf{r}))|^2 \right\rangle \tag{1.71}$$

where the $\langle\cdot\rangle$ denote ensemble average. $\mathbf{f}_I(\mathbf{r})$ is the net force on site I with atomistic force field (for atomistic configuration $\mathbf{r}$), while $\mathbf{F}_I(\mathbf{M}(\mathbf{r})$ is the force on the same site with the trial CG force field (for the mapped configuration $\mathbf{R} = M(\mathbf{r})$).

From Equation 1.68, $\chi^2[U]$ can be re-expressed as

$$\chi^2[\mathbf{F}] = \chi^2[\mathbf{F}^0] + \left\|\mathbf{F}^0 - \mathbf{F}\right\|^2, \tag{1.72}$$

where $\|\mathbf{F}^0 - \mathbf{F}\|^2 \geq 0$. Thus the force field, which provides the unique global minimum of χ^2, is determined from the many-body MF.

From Equation 1.63, χ^2 becomes a quadratic function of the coefficients ϕ, and the MS-CG force field can be determined as the solution to a simple linear least squares problem [39]:

$$\chi^2(\phi) = \chi^2(0) - 2\sum_\zeta b_\zeta \phi_\zeta + \sum_\zeta \sum_{\zeta'} \phi_\zeta G_{\zeta\zeta'} \phi_{\zeta'}, \tag{1.73}$$

where

$$b_\zeta = \frac{1}{3N}\left\langle \sum_I \mathbf{f}_I(\mathbf{r}) \cdot \boldsymbol{\mathcal{G}}_{I;\zeta}(\mathbf{M}(\mathbf{r})) \right\rangle \tag{1.74}$$

and

$$G_{\zeta\zeta'} = \frac{1}{3N}\left\langle \sum_I \boldsymbol{\mathcal{G}}_{I;\zeta}(\mathbf{M}(\mathbf{r})) \cdot \boldsymbol{\mathcal{G}}_{I;\zeta'}(\mathbf{M}(\mathbf{r})) \right\rangle \tag{1.75}$$

Now the coefficients minimizing χ^2 can be determined from the normal system of linear equations [40]:

$$\sum_{\zeta'} G_{\zeta\zeta'} \phi_{\zeta'} = b_\zeta. \tag{1.76}$$

In fact, $G_{\zeta\zeta'}$ can be interpreted as the inner product of basis vectors, i.e., $G_{\zeta\zeta'} = \boldsymbol{\mathcal{G}}_\zeta \odot \boldsymbol{\mathcal{G}}_{\zeta'}$, which quantifies correlations between different interactions in mapped configurations. Similarly, $b_\zeta = \boldsymbol{\mathcal{G}}_\zeta \odot \mathbf{F}^0$ is the projection of the many-body MF onto the corresponding basis vector. Consequently, it follows that the normal equations for the MS-CG approximate force field $\mathbf{F}$ can be expressed:

$$\boldsymbol{\mathcal{G}}_\zeta \odot \mathbf{F} = \boldsymbol{\mathcal{G}}_\zeta \odot \mathbf{F}^0. \tag{1.77}$$

This equation emphasizes that MS-CG equations determine the projection of the MF onto basis set $\{\boldsymbol{\mathcal{G}}_\zeta\}$, making that the MS-CG force field and the many-body MF have the

same inner product with each basis vector. Thus in MS-CG method, the force correlation functions b_ζ provide a clever and compact means for characterizing the many-body MF.

Conditional reversible work

These two groups of methods we mentioned above can be called "parameterized" methods. They are both derived from many-body potential of mean force, and then find ways to approximate this many-body potential into a sum of different simple type of interactions. In the end, they provide CG potentials able to reproduce these target quantities, i.e., structural distributions or force distributions. However, it cannot be guaranteed that these models can predict other non-target properties, or the target properties at a different state point from the parameterized one. In fact, the nonbonded interactions have a more critical impact on this transferability. For nonbonded interactions, so-called "derived" methods [41] exhibit a better transferability, which use the direct atomistic interactions between the mapped atom groups to derive the CG interaction potentials. These potentials have a clear physical meaning, representing a distance-dependent pair interaction (free) energy.

In this work, the CG model we used, named as Fritz model [42], is derived from Conditional Reversible Work (CRW) methods [43], which is one of "derived" methods. Figure 1.4 shows the concept of reversible work, in which the six connected spheres represent hexane (united atom) and two methylene groups are mapped into a single CG site. As CRW describes a distance-dependent pair interaction between two CG sites, constraint simulations with atomistic force field are performed, in which two sites are held at fixed distance r. Then the pair potential of mean force (pPMF) was calculated by

$$U_{\mathrm{PMF}}(r) = \int_{r_m}^{r} \mathrm{d}s \langle f_c \rangle_s + 2k_B T \ln r, \tag{1.78}$$

where f_c is the constraint force between the two CG mapping points, $\langle \cdot \rangle_s$ is a constrained ensemble average at distance s, and r_m is the maximum distance between the two mapping points. We know during simulations only the distance between the two sites is constrained, free rotation of the connecting vector remains possible and larger volume elements are sampled at larger distance. This can lead to an entropy contribution to the averaged constraint force, thus the second term on the right-hand are added to subtract out this contribution.

The resulting $U_{\mathrm{PMF}}(r)$ is the upper one in Figure 1.4, which include indirect contributions of all the interactions between all the atoms in the two molecules. While in the lower part, we exclude the nonbonded interactions between the two sites in the atomistic force field, and then obtain $U_{\mathrm{PMF}}^{\mathrm{excl}}(r)$ that contains only indirect interactions. Thus the difference between these two potentials results in an effective potential $U^{\mathrm{eff}}(r)$ that does not contain

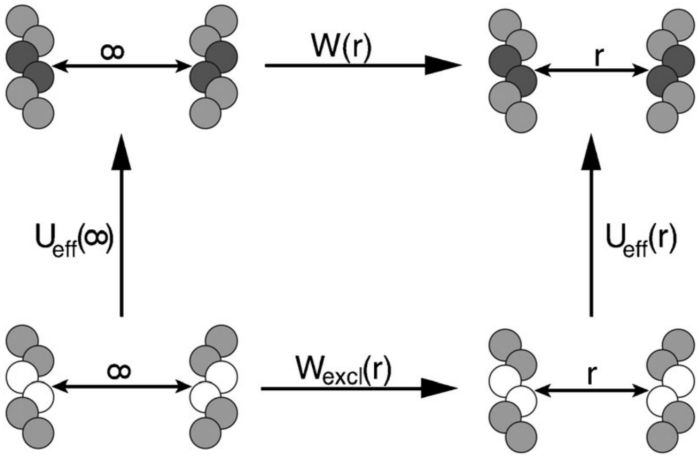

Figure 1.4.: Thermodynamic cycle used to compute the conditional reversible work potential U^{eff}. Top: $U_{\text{PMF}}(r)$ include indirect contributions of all the interactions between all the atoms in the two molecules. Bottom: $U_{\text{PMF}}^{\text{excl}}(r)$ contains only indirect interactions, excluding the nonbonded interactions between the two sites. The CRW potential is then obtained from the difference between these two potentials. Reprinted from [43] with permission of The Licensor through Copyright Clearance Center (4618961237152).

indirect contributions any more.

$$U^{\text{eff}}(r) = U_{\text{PMF}}(r) - U_{\text{PMF}}^{\text{excl}}(r). \tag{1.79}$$

By means of this procedure, we compute reversible work $U^{\text{eff}}(r)$ to introduce interactions between two atom groups in the natural chemical environment of the respective atom groups. By sampling the surrounding environment, the resulting effective potential excludes the indirect interactions but accounts for the proper weight of the relative orientation [41].

Such an approach has been used before to derive united-atom models for small molecules [44] and develop CG nonbonded interactions for polyethylene [45]. As mentioned above, Fritz [42] developed a CG model of PS employing the CRW method. In our work, we will use Fritz CG model to speed up our simulations for studying crystallization and polymorphism of syndiotactic polystyrene. The detail and the transferability evaluation of this model will be discussed in Chapter 2.

1.2.3. Enhanced sampling methods

The idea behind Molecular Dynamics simulations is that we can study the average behavior of a many-particle system simply by computing the natural time evolution of that system numerically and averaging the quantity of interest over a sufficiently long time. This idea is based on "ergodic hypothesis", which has been introduced in Section 1.1.3.

If the system has ergodic behavior, it visits all regions of configuration space. In principle, we assumed that realistic systems have ergodic behavior [4]. But in the currently accessible simulation time, whether all relevant regions of configuration space will indeed be accessed is another matter. Ergodicity may become a problem in many examples of systems in practice, like metastable phases. Some phenomena of interest, like phase transition, will also be rare events on the finite time scales.

The reason behind this is that there are large free energy barriers between these phases. We know free energy landscape always has a global minimum, but also can have a very complex structure with multiple local minima, separated by barriers of various heights. If the barriers between different local free energy minima are large, once the system fall in one of these local minima, it would be difficult to cross the high barriers and access to other regions. When the observation time is limited, the system may easily remain trapped in certain regions of configuration space and leave many relevant regions unexplored.

Thus we need to perform enhanced sampling in MD simulations to overcome the barriers and accelerate rare events. These methods can be classified into tempering-based and collective-variable-based approaches.

Tempering approaches

"Tempering" refers to a class of methods based on increasing the temperature of an MD system to overcome barriers, which relies on the assumption: The rate at which activated (barrier-crossing) events happen is strongly dependent on the temperature. In fact, tempering enhanced methods can be seen as extensions of simulated annealing procedure [46]. Initially, the system is heated at a temperature high enough that the simulation can easily overcome high free-energy barriers. Then the temperature is decreased to smoothly bring the simulation to a local energy minimum. However, the resulting ensemble will strongly depend on the cooling speed, thus possibly providing a biased result.

A better way is to build a ladder of intermediate temperatures between the high temperature and the target (low) temperature. Instead of simulating a single system, we simulate these replicas at the same time and swap coordinates between two neighboring replicas at certain steps with acceptance probability:

$$\alpha = \min\left(1, e^{\left(\frac{1}{k_B T_j} - \frac{1}{k_B T_i}\right)[U(x_j) - U(x_i)]}\right). \tag{1.80}$$

This method is called "parallel tempering" or "replica exchange" [47, 48], requiring that all replicas can traverse the entire ladder. The efficiency of this method is based on the evaluation of the round trip time. Parallel tempering has the advantage that all the replicas can be analyzed to generate meaningful results, e.g., to predict the melting curve of a molecule. However, when using this procedure, one should care for the potentials of

the model, especially empirically parametrized potentials, which often has temperature-transferability problem.

The difference between the replicas is not restricted to be a change in temperature. Any control parameter can be changed, and even the expression of the Hamiltonian can be modified [49]. In fact, a scaling of the Hamiltonian by a factor λ is equivalent to a scaling of the temperature by a factor λ^{-1}. Although Hamiltonian replica exchange relies on unphysically modified ensembles which have no interest, it turns in a smaller modification but more effectiveness than simple parallel tempering.

Note again, all these method relies on an assumption that the dynamics of the most modified ensemble is ergodic, which is not always correct. An example is using parallel tempering to accelerate the sampling over an entropic barrier [50]. Since the height of an entropic barrier grows with the temperature, in this condition the barrier in the most modified ensembles are unaffected.

Collective-variable biasing approaches

In Section 1.1.4, the term "collective variable" (CV) has been introduced as one way to evaluate free energy landscape:

$$F(\boldsymbol{z}) = -k_B T \ln\langle\delta[\boldsymbol{\theta}(\boldsymbol{x}) - \boldsymbol{z}]\rangle. \tag{1.81}$$

Here we use a new symbol $\boldsymbol{z}$ as CV space, and $\boldsymbol{\theta}(\boldsymbol{x})$ as the functions mapping $\boldsymbol{x}$ to $\boldsymbol{z}$. The local minima in the free energy landscape are metastable equilbrium states. In fact, the motivation of evaluating free energy with CVs is to observe the transition between these metastable states along some pathway in the CV space. In many actual cases, however, the standard MD trajectories remain close to only one minimum and very rarely visit others. To observe the rare events, we can perform MD simulations biased on those CVs to overcome the free energy barriers in the CV space.

There are two classes of biasing. One way is to directly compute the gradient of the free energy at local points throughout CV space, called "gradient" methods. The canonical method in this class is "thermodynamic integration" [51].

If one would like MD to explore CV space in the vicinity of $\boldsymbol{z}$, but unfortunately, the system always drifts away from $\boldsymbol{z}$ rather quickly, there would be no way to directly estimate the likelihood of observing the system visit $\boldsymbol{z}$. However, if one knows on average which direction and how strongly the system would like to move if initialized at $\boldsymbol{z}$, it would be possible to measure the gradient of the free energy, $(\partial F/\partial \boldsymbol{z})$, or called "local mean force". From these local mean forces, one can use numerical integration to reconstruct free energy F:

$$F(\boldsymbol{z}) - F(\boldsymbol{z}_0) = \int_{\boldsymbol{z}_0}^{\boldsymbol{z}} \left(\frac{\partial F}{\partial \boldsymbol{z}}\right) \mathrm{d}\boldsymbol{z}. \tag{1.82}$$

Another way is to introduce an additional bias potential and force the system to explore the hard-to-visit regions of CV space. Imagine we have an MD system with bare potential $U(\boldsymbol{x})$, and we add a bias potential $V(\boldsymbol{x})$ to generate a biased total potential:

$$U_b(\boldsymbol{x}) = U(\boldsymbol{x}) + V(\boldsymbol{x}). \tag{1.83}$$

The probability at the CV-point $\boldsymbol{z}$ with this biased potential is [52]

$$\begin{aligned} P_b(\boldsymbol{z}) &= \int \mathrm{d}\boldsymbol{x}\delta[\boldsymbol{\theta}(\boldsymbol{x}) - \boldsymbol{z}]P_b(\boldsymbol{x}) \\ &= \frac{e^{-\beta[F(\boldsymbol{z})+V(\boldsymbol{z})]}}{\int \mathrm{d}\boldsymbol{z}\ e^{-\beta[F(\boldsymbol{z})+V(\boldsymbol{z})]}}. \end{aligned} \tag{1.84}$$

Then we can reconstruct the unbiased statistics from the biased simulations:

$$P(\boldsymbol{z}) = P_b(\boldsymbol{z})e^{\beta V(\boldsymbol{z})} \left\langle e^{-\beta V[\boldsymbol{\theta}(\boldsymbol{x})]} \right\rangle, \tag{1.85}$$

Umbrella sampling [53] is a standard way of using bias potential to overcome free energy barriers. Usually, the bias potential is a simple harmonic spring that tethers the trajectory to a reference point $\boldsymbol{z}_i$ in CV space:

$$V_i(\boldsymbol{z}) = \frac{1}{2}\kappa|\boldsymbol{\theta}(\boldsymbol{x}) - \boldsymbol{z}_i|^2 \tag{1.86}$$

The points $\{\boldsymbol{z}_i\}$ and the value of κ are chosen to make sure that each window overlaps with nearby windows.

From Equation 1.85, we obtain the unbiased statistics $P_i(\boldsymbol{z})$ for each window:

$$P_i(\boldsymbol{z}) = P_{b,i}(\boldsymbol{z})e^{\frac{1}{2}\beta\kappa|\boldsymbol{z}-\boldsymbol{z}_i|^2} \left\langle e^{-\frac{1}{2}\beta\kappa|\boldsymbol{\theta}(\boldsymbol{x})-\boldsymbol{z}_i|^2} \right\rangle, \tag{1.87}$$

In general, the weighted-histogram analysis method (WHAM) [54] is then used to renormalize the probabilities in each window into a single composite probability.

Instead of a set of fixed biases, Metadynamics [55, 56] builds an adaptive bias potential during the simulations:

$$U_b(\boldsymbol{x}) = U(\boldsymbol{x}) + V(\boldsymbol{x}, t). \tag{1.88}$$

The key element of Metadynamics is that the bias is built as a sum of Gaussian functions centered on the points already visited:

$$V[\boldsymbol{\theta}(\boldsymbol{x}), t] = w \sum_{t'=\tau_G, 2\tau_G, \cdots} \exp\left(-\frac{|\boldsymbol{\theta}[\boldsymbol{x}(t)] - \boldsymbol{\theta}[\boldsymbol{x}(t')]|^2}{2\delta\boldsymbol{\theta}^2} \right). \tag{1.89}$$

Here, w is the Gaussian height, $\delta\boldsymbol{\theta}$ is the Gaussian width, and τ_G is the frequency at

which the Gaussians are added.

In Metadynamics, the Gaussian hills will slowly fill the local free energy minimum and climb out of it to another minima, just like the sand filling the pool. Sooner or later, the accumulated Gaussians will fill out all minima and get a uniform sampling of CV space. Ideally, if the sampling of the entire CV space is uniform, we can get free energy directly by making a negative of bias potential [57]:

$$F(\boldsymbol{z}) = -V(\boldsymbol{z}) \tag{1.90}$$

In fact, however, in Metadynamics the instantaneous distribution $P_b(\boldsymbol{x}, t)$ can be written as:

$$\begin{aligned} P_b(\boldsymbol{x}, t) &= \frac{e^{-\beta[U(\boldsymbol{x})+V(\boldsymbol{\theta}(\boldsymbol{x}),t)]}}{\int \mathrm{d}\boldsymbol{x}\ e^{-\beta[U(\boldsymbol{x})+V(\boldsymbol{\theta}(\boldsymbol{x}),t)]}} \\ &= P(\boldsymbol{x}) \cdot e^{-\beta V(\boldsymbol{\theta}(\boldsymbol{x}),t)} \cdot \frac{\int \mathrm{d}\boldsymbol{z}\ e^{-\beta F(\boldsymbol{z})}}{\int \mathrm{d}\boldsymbol{z}\ e^{-\beta[F(\boldsymbol{z})+V(\boldsymbol{z},t)]}} \\ &= e^{-\beta[V(\boldsymbol{\theta}(\boldsymbol{x}),t)-c(t)]} \cdot P(\boldsymbol{x}) \end{aligned} \tag{1.91}$$

This equation hints that $V(\boldsymbol{z}, t)$ will converge to the exact free energy surface plus a time-dependent constant:

$$V(\boldsymbol{z}, t) = -F(\boldsymbol{z}) + c(t), \tag{1.92}$$

where

$$c(t) = \frac{1}{\beta} \log \frac{\int \mathrm{d}\boldsymbol{z}\ e^{-\beta F(\boldsymbol{z})}}{\int \mathrm{d}\boldsymbol{z}\ e^{-\beta[F(\boldsymbol{z})+V(\boldsymbol{z},t)]}}. \tag{1.93}$$

Hence standard Metadynamics leads to a fluctuating estimate of the free energy. The difference between the Metadynamics estimate of the free energy and the true free energy are related to the diffusion coefficient of the collective variables and to the rate at which the bias is grown.

The possible way to decrease this error is to decrease the growth rate of this bias. Well-tempered Metadynamics [58, 59] optimize it by modulating the Gaussian height:

$$w = w_0 \tau_G e^{-\frac{V(\boldsymbol{\theta},t)}{k_B \Delta T}}. \tag{1.94}$$

With this rescaling Gaussian height, the bias deposition rate decreases as $1/t$. With a progressively damped bias, the Well-tempered version of Metadynamics can converge to an exact well-defined limit. By tuning ΔT in between, one can regulate the extent of free energy exploration. When $\Delta T \to 0$, ordinary MD is recovered, while $\Delta T \to \infty$ corresponds to standard Metadynamics.

With well-tempered Metadynamics, the bias does not converge to the negative of the free

energy but to a fraction of it (also plus the function $c(t)$).

$$V(\boldsymbol{z},t) = -\frac{\Delta T}{T+\Delta T}F(\boldsymbol{z}) + c(t). \tag{1.95}$$

Although Well-tempered Metadynamics can reduce the error compared with standard one, the problem of estimating local convergence still remains. Tiwary [60] provide a time-independent estimator for $F(\boldsymbol{z})$:

$$F(\boldsymbol{z}) = -\left(\frac{\gamma}{\gamma-1}\right)V(\boldsymbol{z},t) + \frac{1}{\beta}\log\int \mathrm{d}\boldsymbol{z}\exp\left[\frac{\gamma}{\gamma-1}\beta V(\boldsymbol{z},t)\right], \tag{1.96}$$

where $\gamma = \frac{T+\Delta T}{T}$, called "biasing factor". This estimator depends on two time-dependent functions, However, after an initial transient, the time dependencies of the two functions will cancel out exactly. This estimator allows us to assess the convergence and measure the statistic error of the simulations [61–63].

By inserting it to Equation 1.93, one can obtain

$$c(t) = \frac{1}{\beta}\log\frac{\int \mathrm{d}\boldsymbol{z}\exp\left[\frac{\gamma}{\gamma-1}\beta V(\boldsymbol{z},t)\right]}{\int \mathrm{d}\boldsymbol{z}\exp\left[\frac{1}{\gamma-1}\beta V(\boldsymbol{z},t)\right]}, \tag{1.97}$$

This is another way to reweight the results of Metadynamics by recovering $c(t)$ and then reconstructing the unbiased statistics from Equation 1.91:

$$P(\boldsymbol{z}) = P_b(\boldsymbol{z})e^{-\beta[V(\boldsymbol{\theta}(\boldsymbol{x}),t)-c(t)]}, \tag{1.98}$$

If one observe disagreement between free energies directly from the bias potential and through reweighting, it is a clear signal that the simulations has not converged. In addition, this reweighting by calculating $c(t)$ can also be used to obtain the free energy landscape for some set of CVs $\boldsymbol{z}'$ that are not biased:

$$P(\boldsymbol{z}') = P_b(\boldsymbol{z}')e^{-\beta[V(\boldsymbol{\theta}(\boldsymbol{x}),t)-c(t)]}, \tag{1.99}$$

1.3. Polymorphism of syndiotactic polystyrene

In material science, polymorphism is the ability of a solid material to exist in more than one form or crystal structure. An example is carbon that in its two main polymorphs, graphit and diamond, exhibits amazingly different properties. The possible variations in physical properties make the study of polymorphism essential for quality control in manufacture.

The screening of polymorphs was traditonally performed experimentally in spite of the large costs involved. With computer simulations, researchers are able to screen a large number of polymorphs and make predictions for new polymorphs. In pharmaceutials, there are considerable works [1–3] on predicting polymorphism based on the search of local minima on the free energy surface. The computed free energy landscape can reflect and predict the emerging complexity of the crystal structures. However, active phamaceutical ingredients are usually small, organic molecules.

For polymeric materials, it is more difficult to explore the free energy landscapes of polymorphs, since it involves much larger size and much higher barriers. In fact, most semicrystalline polymers possess only one type of unit crystal cell, while syndiotactic polystyrene (sPS) is well-known for its complex crystal polymorphism.

1.3.1. Experimental results

In experiments, five different crystalline forms of sPS have been reported. They have two types of molecular chain conformations in crystalline regions depending on the crystallization conditions, as shown in Figure 1.5. The α [64–67] and β [68, 69] forms with trans-planar-zigzag conformation can be obtained by cooling the melt or by heating the glass, whereas the other three helix-forming crystalline phases, γ [70, 71], δ [72–74] and ε [75–77] are generated by solution processing. The α and β forms of sPS are further classified into the limiting disordered forms (α' and β') and limiting ordered forms (α'' and β'') [64, 66, 68, 78]. In particular, melt crystallization procedures generally produce the limiting ordered α'' and limiting disordered β' models [78]. The limiting disordered α' model is obtained by annealing the amorphous sample [78], whereas the limiting ordered β'' model is generated by crystallization from solution, when the solvent is rapidly removed at higher emperatures above 150 °C [68]. Two of the helical crystalline phases (δ and ε) can only be generated by guest removal from co-crystalline phases. The δ_e form is transformed into the solvent-free γ form by annealing above 130 °C [70, 72, 78].

In this work, we only focus on thermally-induced forms, α and β. They share same chain conformation but with different packing structures of these chains. The crystallization of the α and β forms from the melt strongly depends on experimental parameters including [64, 68, 78–82]:
(i) the maximum temperature of the melt and the time of the melt at that temperature;
(ii) the crystallization temperature and the crystallization time (i.e. cooling rate);
(iii) the crystalline form of the starting material (i.e. thermal history).

Form these works, there are two important results [79, 80]:
(i) From the same high temperature, fast cooling will result in the α form, whereas slow cooling can yield the β form;
(ii) At the same slow cooling rate, the crystallization from the melt at lower temperatures

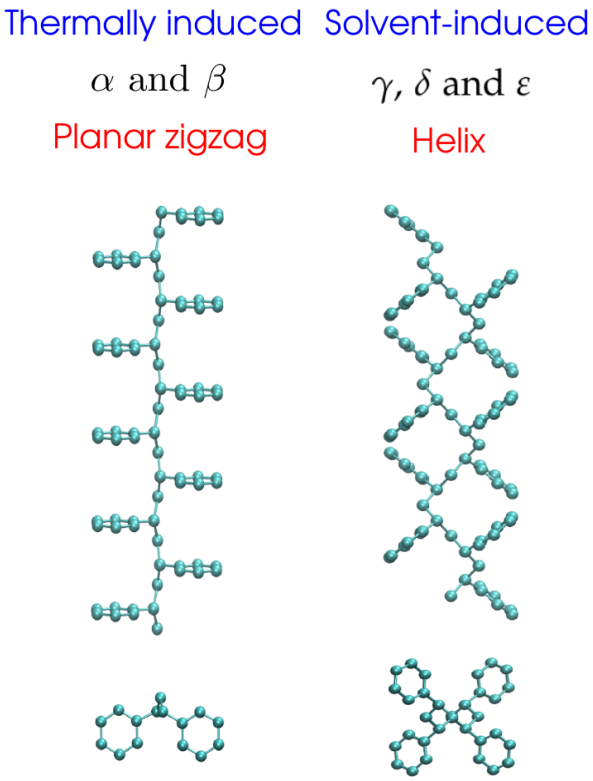

Figure 1.5.: Five different crystalline forms: two crystalline phases (α and β) with trans-planar chains; three crystalline phases (γ, δ and ε) with the s(2/1)2 helical chains.

(lower than 230 °C) leads to the α form, while higher than 260 °Cfavors the β form. When between 230 and 260 °C, mixtures of α and β forms are obtained.

These results suggest that when sPS molecules possess sufficient mobility due to the high temperature and the enough cooling time, β form is the main mechanism of packing. When the chains are stiffened (at low temperature) or possess a reduced molecular mobility (fast cooling), α form become an alternative mechanics, while packing of β-form is more inhibited. This preliminarily indicates that the crystallization of the α form is a result of a kinetically controlled process, while the β form being the thermodynamically stable form. However, the free energy difference between these two forms is unclear yet. These findings illustrate that the experimentally-observed structures depend much on the experimental processing, making conclusions about their thermodynamic equilibrium difficult.

1.3.2. Some related simulations

Several molecular simulation studies have been performed to better understand the nanoporous cavity structures formed by crystalline syndiotactic polystyrene. Tamai and his coworkers [83] studied the size, shape and connectivity of the cavities in the crystal α, β and δ forms. Some other properties were also studied, such as diffusion of gases [84, 85], reorientational motion of guest solvents [86, 87], and sorption of small molecules [88–90]. While these studies helped understand the behavior of specific forms of sPS crystals, they did not address the crystallization process or the relative stability of the polymorphs. With atomistic model, they can only reach several nanoseconds and can not observe self assembly and spontaneous polymorph interconversion, due to their metastability.

The simulation of polymer crystallization remains challenging because these processes are slow on the molecular time scale. In addition, the high barriers between polymorphs can also result in sampling issues. Hence we use CG models to significantly speed up the simulations and employ enhanced sampling methods to overcome the free energy barriers and observe the transition between polymorphs. So far several CG models for polystyrene have been reported, but all works with these CG models focus on reproducing melt properties. From them, we will choose a proper one to reproduce sPS crystals and further polymorphs. The detail of all these CG models will be shown in Section 2.1.

2. Crystallization Simulations

In this thesis, we will focus on exploring polymorphic behavior of syndiotactic polystyrene (sPS by Molecular Dynamics simulations. Before that, however, we should ensure our simulation model can crystallize. As mentioned in Section 1.2.2, the simulation of polymer crystallization and melting is a challenging task because these processes are slow on the molecular time scale. To increase the length and time scales accessible by simulations, coarse-grained (CG) models have proven to be very efficient. However, a key question is whether the resulting CG force fields can be transferable between different thermodynamic conditions, and more importantly, between different phases, i.e., melts and crystals.

In Section 2.1, we will describe the CG model used in this thesis. Then we attempt to employ it to reproduce the crystallization process and melting curve by annealing simulations (Section 2.2) and parallel tempering (PT) simulations (Section 2.3). Both CG and atomistic (AA) simulations are performed with PT method to compare the crystallization process and transition temperature. Note that for efficiency we applied backmapping procedure (See Appendix A) to obtain a crystalline structure at AA level from a CG snapshot, which is used as an initial configuration in atomistic simulations. In Section 2.4, we further assess the transferability of the CG model by discussing the local and packing properties in crystals for both two models.

Note that the results and figures in Section 2.2 and 2.3 are re-used from the author's publication [91].

2.1. Coarse-grained polystyrene models

Several CG models for polystyrene have been reported, but so far all of them focus on reproducing melt properties. We aim to find a proper one which keeps the tacticity informations and is expected to have better transferability to crystals.

2.1.1. Tacticity of polystyrene

As we mentioned in Section 1.3, our research object is syndiotactic polystyrene. The chemical structure of polystyrene is shown in Figure 2.1. The phenyl rings in a polystyrene

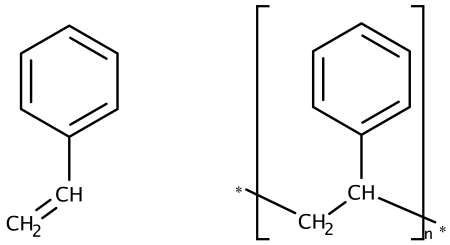

Figure 2.1.: Chemical structure of styrene (Left) and of polystyrene (right), which is obtained by polymerization of styrene monomers.

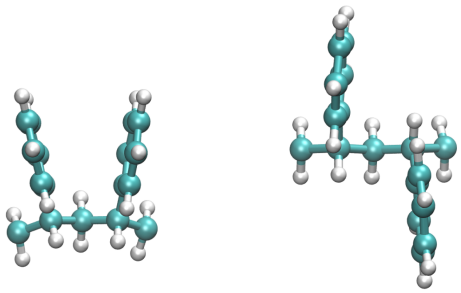

(a) meso diad **(b)** racemo diad

Figure 2.2.: Types of diads in polystyrene chains. In a *meso* diad both phenyl rings are in the same side, while *racemo* diad in the opposite sides.

chain are attached together with a hydrogen atom to a carbon atom. This phenyl group and the adjacent hydrogen atom cannot swap their positions, neither in real systems nor in atomistic simulations, due to steric hindrance. That makes the rings keep "up" or "down", when one face all rings by straightening and rotating the chain as Figure 2.2. If all rings in a chain point to the same side, it is called isotactic, while the rings pointing to alternating sides, that is syndiotactic. In atactic chains, the rings are randomly pointing.

It is noteworthy that tacticity can affect the physical properties of the polymer. For instance, isotactic and syndiotactic polystyrene can crystallize, while atactic one only exhibits amorphous structures. In addition, isotactic and syndiotactic polystyrene exhibit different polymorphic behavior. Hence the tacticity information is necessary to keep in the simulating model, if one want to study polymorphism of sPS. The distribution of local degrees of freedom as bonds, angles and torsions would be differed by the tacticity. To keep the tacticity information, the type of "diads" should be recorded when coarse-graining, that is, recording the relative orientation of two neighboring rings. In a *meso* diad both phenyl rings are in the same side, while *racemo* diad in the opposite sides, which are shown in Figure 2.2.

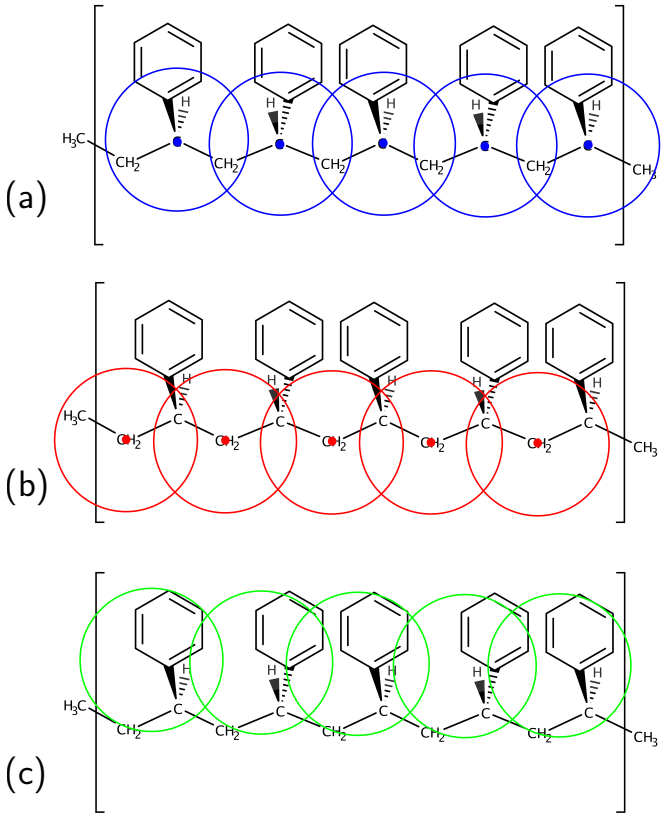

Figure 2.3.: Three models use a 1:1 mapping scheme, but center the beads in different ways: (a) on the backbone carbons to which the phenyl rings are attached [92]; (b) on methylene carbons [93]; (c) on the real center of mass of the monomer [94].

2.1.2. Mapping scheme

The degree of coarse-graining could range from a few beads per monomer up to one bead for many monomers or even an elipsoid for a whole chain. We have to choose the proper degree for the problem of interest. To study the polymorphism, clearly, the model should involve the informations of the side chains, as the orientation of the side chain determines the difference among all phases. As we mentioned before, there are several CG models of polystyrene, which make different choices of mapping schemes depending on the questions and properties of interest.

1:1 mapping scheme

Several models use a 1:1 mapping scheme, i.e. one bead for one monomer, but in different ways [92–94] (see Figure 2.3).

Sun and Faller [92, 95] center the beads on the backbone carbons to which the phenyl rings are attached, shown in Figure 2.3 (a). In this model, they use a single type of bead to

only describe atactic PS without detailed information about chain stereosequence. Their study focused on dynamics of polystyrene melt, which needs hundreds of monomers and several microseconds and is not accessible by fully atomistic simulations.

Milano and Mueller-Plathe [93] center the beads on methylene carbons (Figure 2.3 (b)). This model uses two bead types to represent different types of diads, i.e. *meso* and *recemo*. Then the bonded potentials include three different bond types (*mm*, *mr*, *rr*) and six angle types (*mmm*, *mmr*, *mrm*, *mrr*, *rmr*, *rrr*) without any effective torsional potential. Their aim is to generate well-equilibrated atomistic amorphous phases of high molecular weight polymers by backmapping from simulations of this CG model. Thus the stereosequence information can deduce the positions of side chains and make the backmapping possible. However, their study still focus on melt properties of atactic PS. Note that this CG model, without inclusion of torsional terms, is found unable to well reproduce the distribution of torsional angles of syndiotactic chains.

Both of the two models are derived by Iterative Boltzmann Inversion (IBI) method (See Section 1.2.2) and show efficient for studying melts. However, Carbone and coworkers [96] found that Milano model, derived by IBI method at 500 K, have problem with thermodynamic transferability. This CG potential results in a deviation in thermal expansion behavior from experiment or atomistic simulation, especially below 430 K. Following that, they aim to develop a more temperature-transferable IBI-CG potential for PS and add a linear modification in the potential when doing the structure-based iterations until the target pressure is reached [94]. In addition, they center the beads in a different way, i.e., on the real center of mass of the monomer (Figure 2.3 (c)). Furthermore, this model also uses two bead types to represent different types of diads, but their nonbonded and torsional potentials are averaged over all the possible combinations of diads. With this CG model, they cool system from 500 K to 400 K and reproduced the thermal expansion behavior very well, compared with atomistic simulations and experiments. They claimed that this good reproduction probably benefits from the mapping schemes, i.e., putting the CG bead center on the real center of mass, which can include more phenyl ring information in an indirect way, while the phenyl-phenyl interactions and the ring reorientations are found more important in structural changes when the temperature decreases.

On the whole, all these models aim to reproduce melt properties of atactic polystyrene. In our case, the single-bead representations for a polystyrene monomer are probably not sufficient to reproduce the structures of syndiotactic polystyrene and further observe its polymorphism, as they lack the necessarily direct degrees of freedom, i.e. phenyl rings.

2:1 mapping scheme

As mentioned above, more direct phenyl rings information is necessary to explore the polymorphism of sPS. Therefore, we seek CG models with higher resolution, i.e., two beads represent one monomer (2:1).

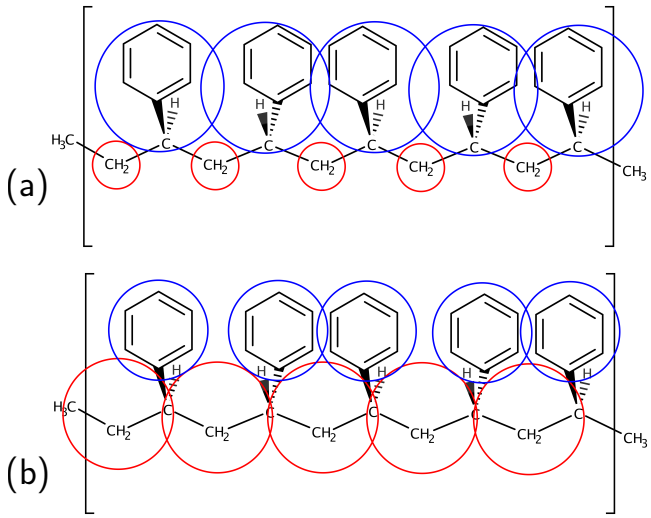

Figure 2.4.: Two Harmandaris models [97, 98] use a 2:1 mapping scheme, but in different ways.

Harmandaris and coworkers [97, 98] devised two different two-bead-per-monomer models. In their first model [97] (Figure 2.4(a)), the CH_2 group of the backbone chain is represented by one CG bead, whereas the remaining CH group of the monomer in the backbone and its pendant phenyl ring are represented by another CG bead. In their second model [98] (Figure 2.4(b)), the phenyl ring is represented by one CG bead, while the other bead represents the CH_2 of the backbone as well as a contribution from each one of the two neighboring CH groups.

Both models have two beads per monomer to keep sufficient structural details including tacticity and the information of phenyl ring positions, but in both models, these beads are connected linearly without side groups. This can avoid deriving improper dihedral potentials to keep the stereochemistry fixed. However, in the first model, there is a large difference between the size and relative mass of the the two CG beads. The mass ratio is about 1:6.5, and this asymmetry in mass has a strong effect for the dynamical behavior of the CG chains. If real masses are assigned to each CG bead, then for the fast motion of the bead A, a comparatively small time step must be used. Otherwise, the steepness of the potentials would result in unrealistically large collision forces. To overcome these drawbacks, the second model has a more suitable size and mass balance between the two beads, and now the mass ratio is 1:2.8.

Both models can well reproduce the static properties of short atactic PS chains, e.g., internal distances, radius of gyration, end-to-end distance. However, the softer nonbonded repulsive potentials and beads closer in size make the second mapping scheme better reproduce the pair distribution function, which leads to a better agreement in the local chain conformations and melt packing with atomistic simulations.

Moreover, the second mapping scheme groups the phenyl rings as a separate bead, which can reproduce tacticities more accurately and makes it easier to observe and study polymorphism. Based on this second mapping scheme, Fritz and coworkers [42] developed a new CG force field, using the conditional reversible work (CRW) method [43] (See Section 1.2.2) to derive the nonbonded interactions instead of the purely repulsive LJ-type potentials in the Harmandaris second model [98]. With CRW method, this new model show better transferability for temperatures and phases. The detail about this new force field for the model will be presented in next section.

4:1 mapping scheme

Rossi and coworkers [99] choose an even lower level of coarse-graining scheme: each monomer is represented by four small MARTINI [100] beads, with three beads representing the phenyl rings and one bead for the aliphatic part (see Figure 2.5). In the MARTINI approach, interaction parameters are determined by reproducing thermodynamic properties — densities and free energies of partitioning. They offer a large number of chemical building blocks and aim for a wide range of applications without the need to re-parametrize the model each time. However, as little structural input is taken into account, MARTINIT can fail in reproducing some of specific structural characteristics of polymer systems. In Rossi models [99], they adopt a more "hybrid" approach for polystyrene. As polystyrene has more complex structural features, both structural and thermodynamic properties are used as a target during the parameterization. Compared with the schemes mentioned above, this mapping scheme can preserve the planar structure of the phenyl rings, which is expected to better reproduce the polymorphism of sPS. However, during the parameterization, both two models here do not retain any information about the local tacticity of the original atomistic sequence. These models only reflect the average property of atactic chains, which makes the models unsuitable to our work.

2.1.3. The CG Fritz model

Among those mapping schemes mentioned in Section 2.1.2, the CG model of Fritz *et al.* [42] is considered to be more suitable to study polymorphism of sPS. It maps each monomer onto two CG beads of different types, denoted A for the chain backbone and B for the phenyl ring (see Figure 2.6). This model is derived from all-atom (AA) model of Mueller-Plathe [101], and its force field includes the bonded and nonbonded interaction potentials in a tabulated form and are derived separately.

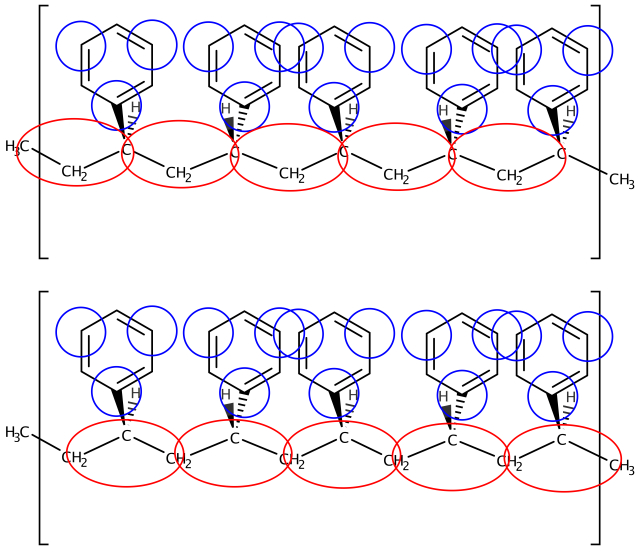

Figure 2.5.: Mapping schemes 4:1. In Rossi models [99], each monomer is represented by four small MARTINI [100] beads, with three beads representing the phenyl rings and one bead for the aliphatic part.

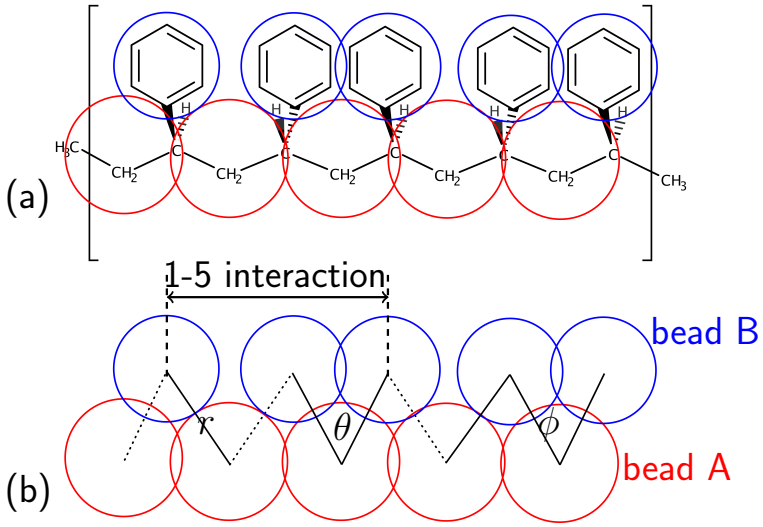

Figure 2.6.: Fritz CG model [42]. (a) Same mapping scheme with the Harmandaris second model [98] (b) The CG model represents PS by a linear chain, where the beads are connected by CG bonds A–B. The bonded force fields include bond r, angle θ and dihedral angle ϕ potentials, and also 1-5 interactions.

Bonded interactions

Figure 2.6 shows that the CG model represents PS by a *linear* chain, where the beads are connected by CG bonds A–B. There are no bonds between the A beads, and the close connection between them is reproduced indirectly by the angular potentials θ_{ABA}. As mentioned above, using linear chain instead of including side chains can avoid improper dihedral potentials, which can make the development more complicated.

Bonded potentials of the CG model are derived by direct Boltzmann-inversion of the distributions generated from atomistic simulations of isolated PS chains with 25-mers in vacuum using stochastic dynamics at 503 K. Fritz *et al.* [42] proved that only the type of diad is defining the type of potential and the influence of neighboring diads can be neglected. Thus these isolated dimers simulations allow us to develop CG force fields separately for *meso* and *racemo* diads, and in principle, allow us to study isotactic and syndiotactic melts with this CG model. To differ these potential parameters for different diads, each bead type is separated further into two different types, i.e., $\mathrm{A}^{\mathrm{meso}}$, $\mathrm{A}^{\mathrm{racemo}}$, B^{up}, $\mathrm{B}^{\mathrm{down}}$.

It is worth noting that the torsions in the CG model have two different orientations, where the potentials, ranging from -180 to 180 degree, are mirrored around 0 degree. Those "up" or "down" informations (mentioned in Section 2.1.1) also depend on the reference direction. Considering that, a direction should be assigned to the chains by numbering the beads with the following scheme: $A_1, B_1, A_2, B_2, A_1, B_1, A_2, B_2, \cdots$, where $A_1B_1A_2B_2$ and $A_2B_2A_1B_1$ are forward direction, while $A_1B_2A_2B_1$ and $A_2B_1A_1B_2$ are backward direction. Only in this way, these "up" or "down" informations and their responding torsion types are distinguishable. For example, in a syndiotactic polystyrene chain, $A_1B_1^{up}A_2B_2^{down}$ and $A_1B_2^{down}A_2B_1^{up}$ share one dihedral potential, while $A_2B_2^{down}A_1B_1^{up}$ and $A_2B_1^{up}A_1B_2^{down}$ share another one (see Figure 2.7). In the following work, we only use the parameters of syndiotactic polystyrene whose chains only consist of racemic diads.

From Equantion 1.69, we can give the bond, angle and dihedral angle potentials as

$$U_b^{\mathrm{CG}}(r,T) = -k_BT \ln p^{\mathrm{CG}}(r,T), \tag{2.1}$$

$$U_a^{\mathrm{CG}}(\theta,T) = -k_BT \ln p^{\mathrm{CG}}(\theta,T), \tag{2.2}$$

$$U_d^{\mathrm{CG}}(\phi,T) = -k_BT \ln p^{\mathrm{CG}}(\phi,T). \tag{2.3}$$

In the Harmandaris second model [98], bonded interactions up to torsions (1-4 neighbors) were taken into account. All longer ranged CG interactions starting from 1-5 upwards were modeled by repulsive nonbonded interactions. However, Fritz *et al.* [42] found that 1-5 interactions affect the form of the distributions of other degrees of freedom, while

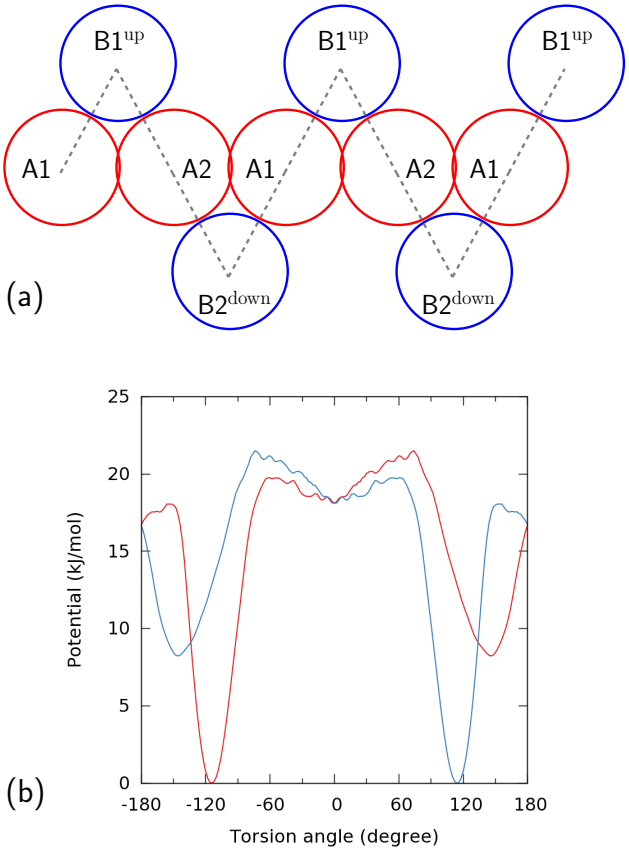

Figure 2.7.: Dihedral potentials have two mirrored orientations. (a) The chain direction should be assigned by numbering the beads with the following scheme: $A_1, B_1, A_2, B_2, A_1, B_1, A_2, B_2, \cdots$, where $A_1B_1A_2B_2$ and $A_2B_2A_1B_1$ are forward direction, while $A_1B_2A_2B_1$ and $A_2B_1A_1B_2$ are backward direction. (b) An example for sPS, $A_1B_1^{up}A_2B_2^{down}$ and $A_1B_2^{down}A_2B_1^{up}$ share one dihedral potential, while $A_2B_2^{down}A_1B_1^{up}$ and $A_2B_1^{up}A_1B_2^{down}$ share another one.

the 1-6 interactions and beyond do not change the peak positions of the distributions anymore and only change the peak heights slightly. Furthermore, this influence of the interaction range can be only to a small extent corrected by the nonbonded potentials in CG model, which means they cannot replace the 1-5 bonded interactions. Consequently, they develop the CG bonded potentials including 1-5 interactions:

$$U_{1-5}^{\mathrm{CG}}(r,T) = -k_B T \left[\ln p_{1-5}^{\mathrm{target}}(r,T) - \ln p_{1-5}^{\mathrm{correct}}(r,T)\right]. \tag{2.4}$$

The 1-5 interaction potentials are distance-dependent pair potentials. $p_{\mathrm{target}}^{1-5}(r,T)$ is the 1-5 distributions from the atomistic model. This distributions include the influence of the intermediate interactions up to 1-4, and thus they eliminate it by adding a correction function of $p_{1-5}^{\mathrm{correct}}(r,T)$.

As mentioned above, Boltzmann Inversion methods are temperature dependent, not only due to the prefactor $-k_B T$ but also due to the temperature dependent distribution functions p. In practice, if the potentials applied to other temperatures, one has to evaluate the transferability (See Section 2.4.1).

Nonbonded interactions

The nonbonded potentials are derived by the conditional reversible work (CRW) method [43], which has been introduced in Section 1.2.2. They are obtained from constrained dynamics at 503 K with the atomistic model of two chain segments with three or four monomers in vacuum. In these runs the atoms mapping to a pair of beads A or B were held at fixed distance r. The pair potential of mean force (PMF), U_{PMF}, was calculated by

$$U_{\mathrm{PMF}}(r) = \int_{r_m}^{r} \mathrm{d}s \langle f_{\mathrm{c}} \rangle_s + 2k_{\mathrm{B}} T \ln r, \tag{2.5}$$

where k_{B} is the Boltzmann constant, T is the temperature, f_{c} is the constraint force between the two CG mapping points, $\langle \cdot \rangle_s$ is a constrained ensemble average at distance s, and r_m is the maximum distance between the two mapping points.

The effective, nonbonded A–A interaction potential is next obtained from

$$U^{\mathrm{eff,A-A}}(r) = U_{\mathrm{PMF}}^{\mathrm{A-A}}(r) - U_{\mathrm{PMF}}^{\mathrm{excl,A-A}}(r) \tag{2.6}$$

where the second PMF, $U_{\mathrm{PMF}}^{\mathrm{excl,AA}}$, is along the same coordinate r but excludes all direct A–A atomistic interactions while maintaining all other interactions with and between neighboring parts of the oligomers. A similar procedure is applied to A–B and B–B. As the phenyl rings are separated from backbone, unlike 1:1 mapping schemes, these specific types for describing orientation and tacticities do not influence the nonbonded interactions. Therefore, the nonbonded potentials are developed from the sampling of

atomistic pairs of oligomers with isotactic tacticity, but used for all tacticities.

This CRW method is different from most other structure-based CG methods [97, 98], which use structures of equilibrated atomistic melts as target structures and fit the non-bonded potentials in order to reproduce these target structures. One advantage of this deriving approach is that it is computationally inexpensive since it is based on the atomistic simulation of trimers in a vacuum. More importantly, this approach is expected to have better transferability since it use the direct atomistic interactions between the mapped sites embedded in the surrounding environment (neighboring beads).

To evaluate the temperature transferability of this model, Fritz [42] performed a series of simulations in the range of temperatures between 403 and 523 K with atomistic and CG model. This CG model was found to correctly describe the melt packing and to reproduce the density of atactic PS melts in this range of temperatures. Moreover, this model was employed to calculate excess chemical potentials [102] and further employed in hierarchical simulations of polystyrene surfaces [103]. All these application indicate that this CG model has an excellent transferability not only to reproduce bulk-like melt packing characteristics.

2.2. Annealing simulations

For now, Fritz model had only been validated on melt properties of atactic PS. However, our work focus on studying the polymorphism of syndiotactic PS crystals, so we should firstly test its ability to crystallize. The initial system is an sPS melt that contains 9 chains, each comprising 10 monomers. Annealing simulation is performed from $T = 500$ K to $T = 250$ K, with a total cooling time of 250 ns. This is then followed by a heating procedure back to $T = 500$ K at the same rate. To make the system stable, the simulation box is kept rectangular under isotropic-pressure coupling. Note that these annealing simulations and the following parallel tempering simulations were all performed using the molecular dynamics package GROMACS 4.6 [20].

We use nematic order parameter P_2 (see the detail in Section 4.1) to characterize the order degree of the system during the cooling, heating, recooling, and reheating processes, where 1 means totally ordered, while 0 means disordered. The evolution of order parameter P_2 is displayed in Figure 2.8. It shows that in the first cooling, we have not obtained the totally ordered structures. When heating it after that, in principle, the system should go back to melt, but on the contrary, it gets more ordered. Also, in the recooling process, the system go back to melt in the beginning, then go up to completely ordered state. This shows a significant hysteresis, apparently due to the fast annealing rate. In experiments, the time scale of cooling systems usually reach several minutes, which is currently unreachable in MD simulations, even with a CG model.

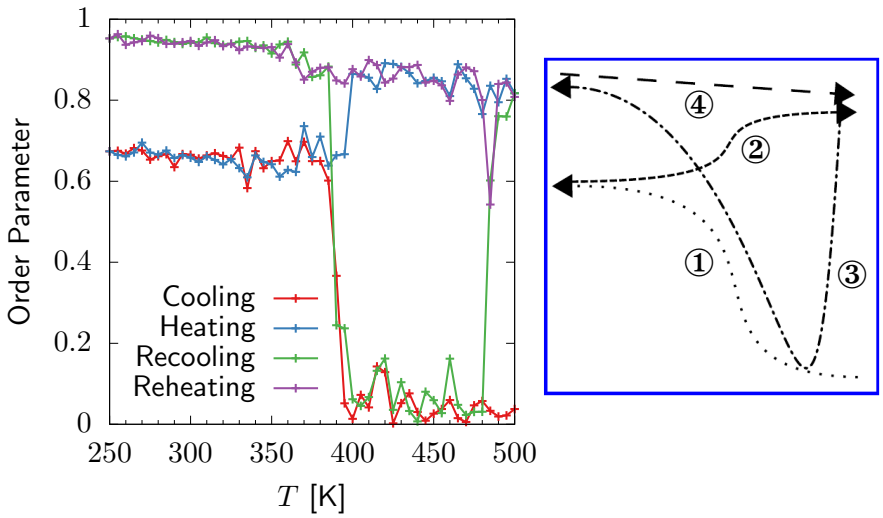

Figure 2.8.: Evolution of structural order parameter (where a value of 1 is completely ordered and 0 is disordered) during the cooling, heating, recooling and reheating CG-MD simulations.

Remarkably, with repeat cooling and heating in CG simulations, we can observe the highly-ordered conformations (see Fig. 2.9). It is the first time to observe a syndiotactic PS crystal in a CG level, which benefits from the direct informations of side chains retained in this CG model.

2.3. Parallel tempering simulations

To further evaluate this CG model, we employ parallel tempering (PT) method [47] in the CG and atomistic (AA) simulations. From Section 1.2.3, we know that parallel tempering is an enhanced sampling method, which is a better way to overcome the cooling rate problem in annealing simulations. Instead of simulating a single system by decreasing the temperature, we simulate the replicas at a ladder of temperatures and swap neighboring This method can help us to predict the melting curve without hysteresis.

In atomistic simulations, however, it is still difficult to generate crystalline phases, even with PT method. Thus backmapping procedure (See Appendix A) is used to generate a highly ordered atomistic configuration from a CG snapshot, which is taken as an initial structure in both of the PT simulations (See Fig. 2.9). The backmapping just offers a single snapshot, the atomistic simulations still have major sampling hurdles (Section 3.3). With this initial structure, however, we can roughly obtain a phase transition behavior and a transition temperature. With order parameter P_2, Figure 2.10 (a) shows that both AA and CG PT simulations display a phase transition, and the transition temperatures are both around 450 K. It indicates that this CG model can reproduce the phase transition

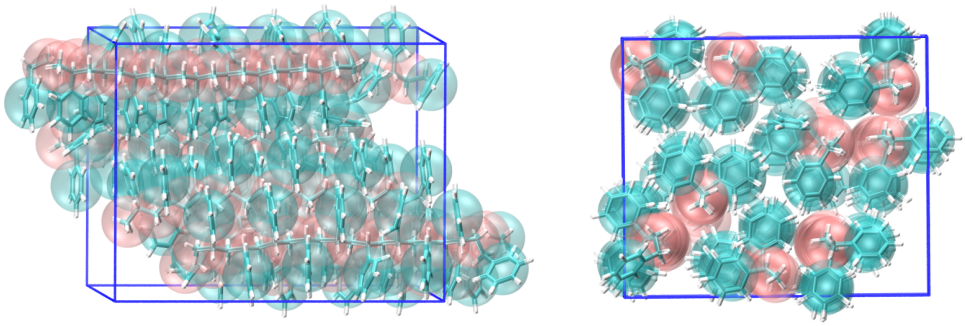

Figure 2.9.: Backmapping: Reconstruct an atomistic high-ordered configuration from a CG snapshot.

of sPS roughly at the correct temperature and hints at remarkable transferability of the CG model between the melt and the crystal.

Some differences, however, appear between these two models at low temperatures. Figure 2.10 (b) and (c) show multiple peaks in the order-parameter distributions of the AA model, while only three peaks are found in the CG model. From the result, we conclude that due to the simplification of side chains, the CG model is more likely to exhibit high-ordered structures instead of some intermediate phases. Furthermore, the simplification leads the packing of phenyl rings unknown and may further cause an inappropriate packing in atomistic system from backmapping procedures. Due to the inappropriate packing, the resulting structures are not stable in atomistic system and do not have a chance to relax upon the simulations. Meanwhile, the atomistic simulations cannot reconstruct the high-ordered phases during the simulation time, owing to the sampling limitation (Section 3.3).

2.4. Transferability to crystals

Coarse-grained models usually have state dependent potentials because averaged-out degrees of freedom are weighted differently at different temperatures. In most cases, the CG models can only be used within a certain temperature range around the developed one and have to be redeveloped for other temperatures. Fritz [42] have validated the temperature transferability of this CG model between 403 and 523 K. However, in our simulations, this model is expected to apply to a much broader temperature range, from 250 K to 550 K. More importantly, our systems are not limited to melts but also involve crystalline phases. The agreement in transition temperature have preliminarily indicated the transferability of this CG model between the melt and the crystal. To further evaluate the transferability to the crystals, we show the local and packing properties of crystalline phases at 250 K obtained from CG PT simulations and compare them with atomistic

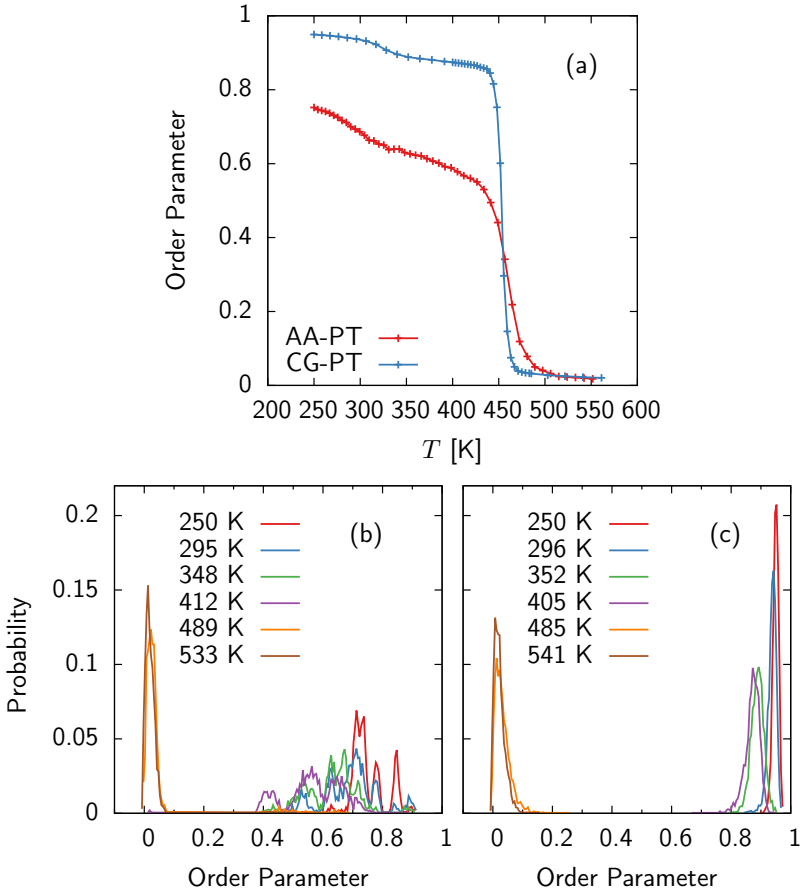

Figure 2.10.: (a) Structural order parameter as a function of temperature calculated from AA and CG PT simulations. Structural order-parameter distributions at different temperatures: (b) AA and (c) CG.

models.

2.4.1. Local properties

It has been mentioned in Section 2.1.3 that bonded potentials are derived from the isolated atomistic chains in vacuum. With consideration of the influence of the interaction range, 1-5 interactions are added in the bonded potentials, which leads to a very good reproduction for melts.

In Figure 2.11, the local distributions of crystals are compared between AA and CG simulations. Note that the local distributions of the AA model is calculated by projecting the AA degrees of freedom onto the CG variables (same way for radial distributions functions in Section 2.4.2). From Figure 2.11, we find that although the local distributions of crystals show large differences from melts, the crystal distributions from CG simulations are very close to the atomistic models. There are small deviations between the CG and atomistic distributions in the degrees of freedom that connect B beads, i.e., BAB angles and B-B 1-5 distances, which can also be found in CG melts [42]. The possible reason is that B beads are slightly more influenced by surroundings, as the phenyl rings are more exposed to the interchain influences than the backbone. In addition, the small shoulders existing in atomistic models probably come from the backmapping and sampling issues.

The good agreement between the distributions of CG and atomistic crystals confirms that the development of CG potentials by sampling isolated chains in vacuum and the distinction between tacticities is successful. The correct reproduction of local distributions in the CG model leads to a consistency between the atomistic and the CG model for the chain stiffness and the overall chain dimensions.

2.4.2. Packing properties

The local packing of the chains is examined by calculating radial distribution functions (RDF), which describe the particle density as a function of the distance. In Figure 2.12, RDFs between A-A, B-B pairs in sPS crystals at 250 K and melts at 500 K are shown. As the crystals are ordered phases, they exhibits sharper distributions than melts. The nonbonded potentials derived from CRW methods, whose target is not structural distributions, however, make a very good reproduction of RDFs in both melts and crystals.

As mentioned before, Fritz [42] obtain a very good agreement of density between 403 and 523 K with atomistic and CG model, but their simulations were not related to crystalline phases. Here we show the density evolutions as the function of temperature with the phase transition phenomenon obtained from atomistic and CG PT simulations (Figure 2.13). It shows a large difference between the two models for the crystals, where the CG densities are much higher than atomistic ones. In the figure, the CG density evolution exhibits a

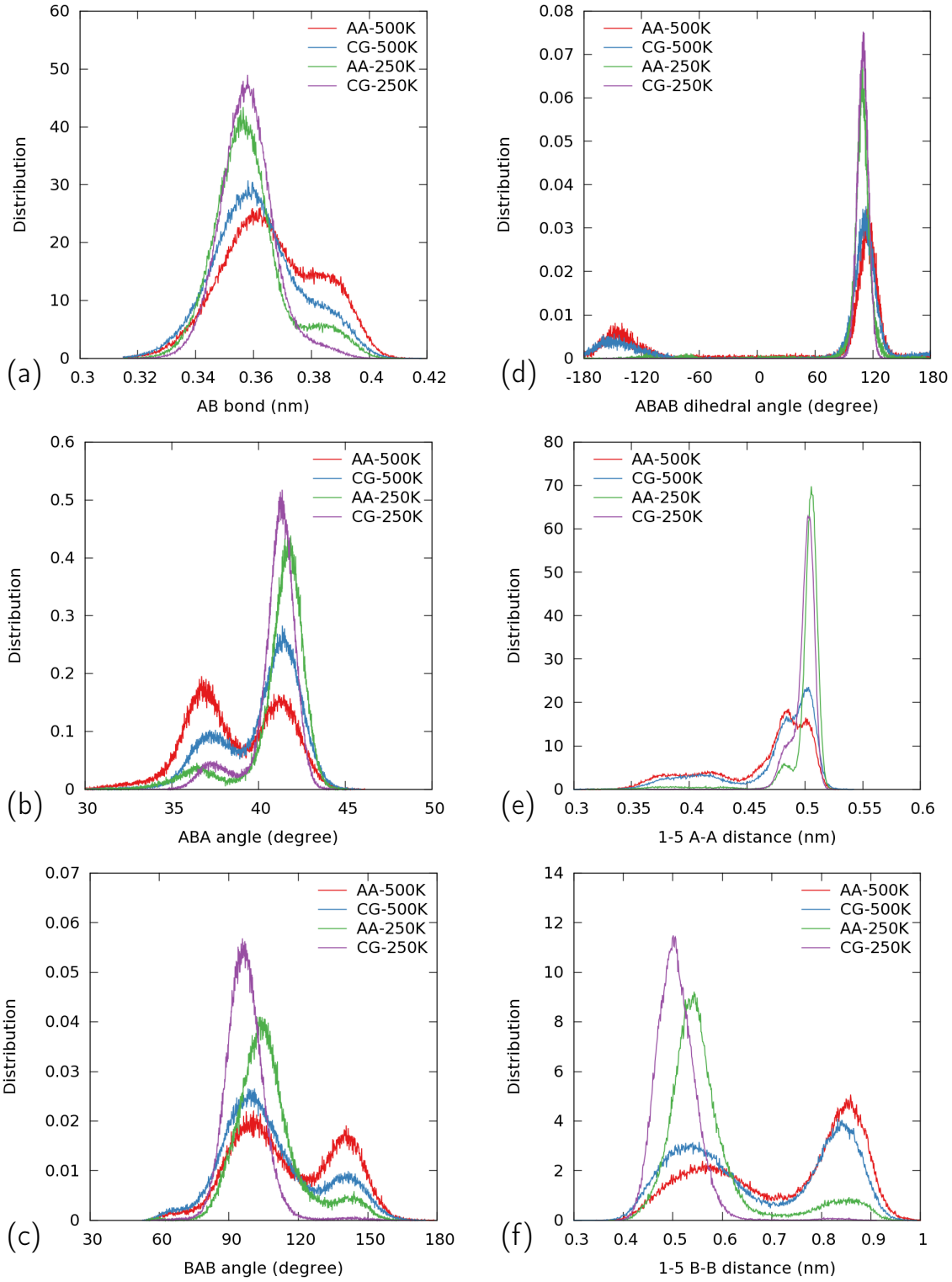

Figure 2.11.: Distributions of bonds (a), ABA angles (b), BAB angles (c), ABAB dihedrals (d), A-A 1-5 distances (e), and B-B 1-5 distances (f): comparison between AA and CG models at 500 K (melt phases, developed temperature) and 250 K (crystalline phases). All these distributions are obtained from the above PT simulations.

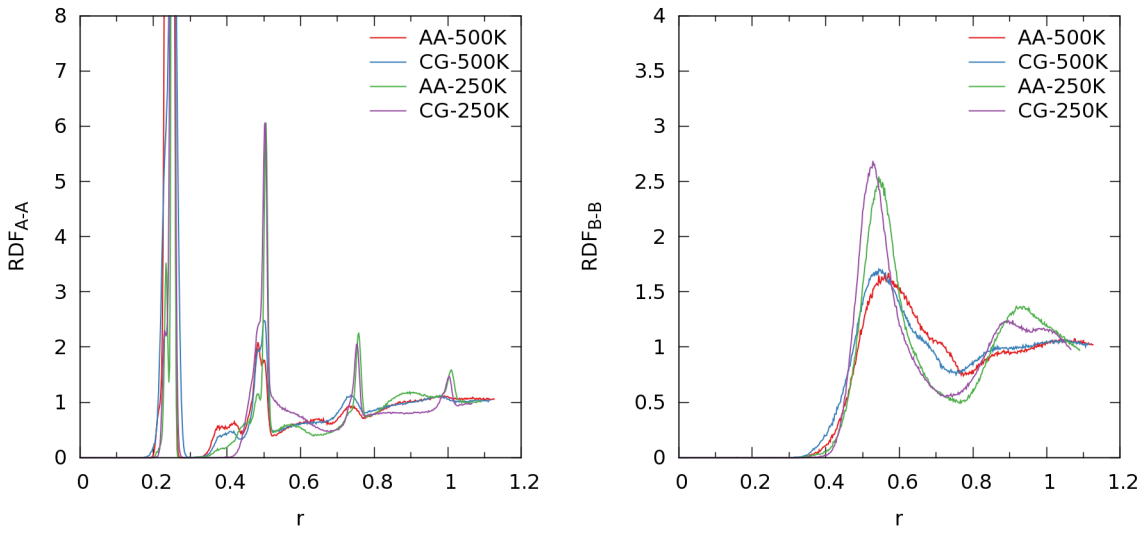

Figure 2.12.: Radial distributions functions between A-A, B-B pairs in sPS crystals at 250 K and melts at 500 K.

clear phase transition along the temperatures, while in the atomistic simulations, there is no any sign for it. The possible reason for on transition sign in AA model may still lie in the backmapping and sampling issues in atomistic simulations. However, the large difference of density shown in the crystals between the two models is caused by the inaccurate packing of phenyl rings in the CG model. Because the density is found much dependent on polymorphs, we will discuss more details in next chapter.

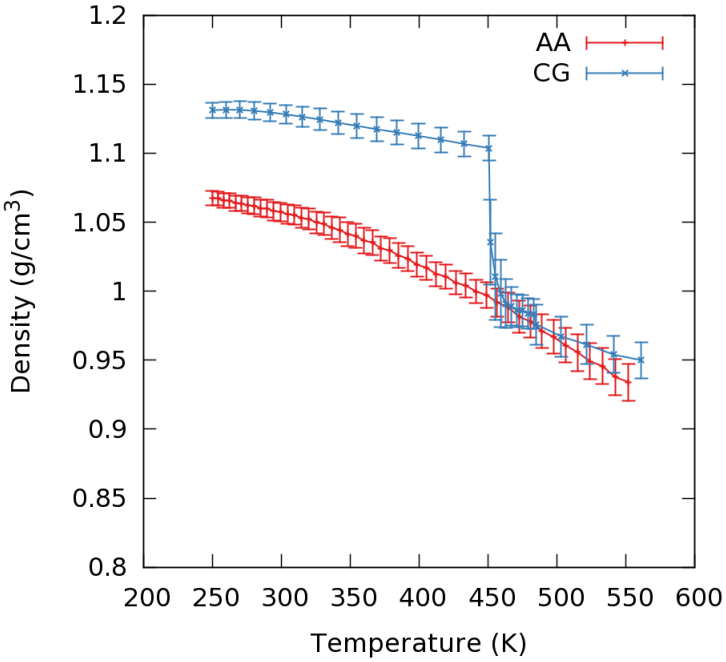

Figure 2.13.: Density evolutions obtained from atomistic and CG PT simulations.

3. Polymorphs from Parallel Tempering Simulations

In Chapter 2, it was shown that the CG Fritz model can reproduce the phase transition of sPS roughly at the correct temperature. Furthermore, the local intra-molecular distributions of CG crystals also have a good agreement with atomistic crystals. This overall hints at remarkable transferability of the CG model between the melt and the crystal. In this chapter, we will further characterize the ability of this CG model to reproduce different forms observed in experiments.

Note that the results and figures in Section 3.1 are re-used from the author's publication [91].

3.1. Small system

In this section, we will focus on three forms (α, β, and δ form) listed in Table 3.1. We perform atomistic (AA) and CG parallel tempering simulations from these different crystal structures. Note that these initial structures are obtained from experimental data with atomistic positions, then mapped into CG configurations (i.e., no backmapping is used here). Due to the small size, we have to use isotropic pressure coupling and fix the box angles to make the simulation-box stable enough during the PT simulations. Hence the box shape is fixed according to the experimental unit cell. Figure 3.1 shows that the choice of box geometry leads to qualitatively different thermodynamics, which we will analyze in detail below.

Table 3.1.: Main crystal structures of s-PS studied in this work, along with the number of crystal units, number of chains and number of monomers for each chain in the MD simulation.

Crystal	a (Å)	b (Å)	c (Å)	γ (°)	Space group	Conformation	N_{unit}	$N_{chain} \times N_{mon}$
α [66]	25.82	26.26	5.03	119.9	$P3$	$TTTT$	1×1×5	9×10
β [69]	8.79	28.61	5.04	90.0	$P2_12_12_1$	$TTTT$	3×1×5	12×10
δ [72]	17.38	11.73	7.81	115.0	$P2_1/a$	$(TTGG)_2$	3×2×3	12×12

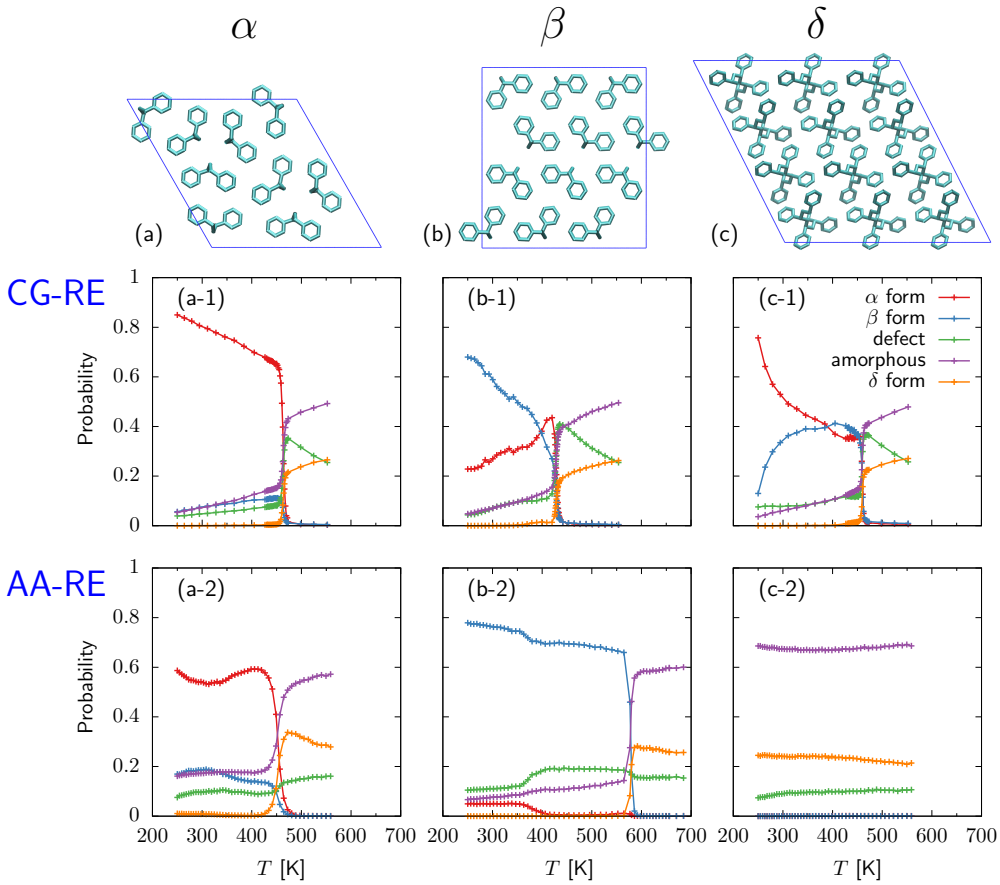

Figure 3.1.: From top to bottom: Initial crystal structures for (a) α, (b) β and (c) δ polymorphs; probability of polymorphs as a function of temperature obtained from CG and AA REMD simulations.

The probabilities of different phases shown in Figure 3.1 are calculated by our procedure, which is to identify the forms for each segment (i.e., two monomers) based on its local environments (detail is shown in Appendix B). From this figure, we observe the stabilization of α and β crystalline forms. Here, "defect" means that the segment exhibits crystalline features, but does not belong to any form. Besides, the helical chain segments are found unstable and non-existent after parallel tempering simulations, thus they are not further classified and all of them are called δ form for convenience.

3.1.1. α form

Figure 3.1 (a) shows the initial α form configuration, which contains 9 chains of 10 monomers each. RE simulations were performed for both the CG and AA models for 1200 ns and 300 ns, respectively. Figures 3.1 (a-1) and (a-2) show the polymorph distributions in the temperature range $250 - 550$ K. At both resolutions in this box geometry, the α form is not only stable but also predominant, with a transition temperature around 460 K.

As mentioned above, the initial structure of atomistic simulations is directly obtained from experiments, not from backmapping. Figure 3.2 shows the order parameter distributions starting from α form. Clearly, the distributions of atomistic simulations have only two main peaks, same as in the CG case, which is significantly different from the distributions starting from the backmapping procedure (See Figure 2.10 (b)). In simulations from α form, the order parameter is always close to 1 at low temperature, while from backmapping the order parameter will drop to 0.8 or lower. Figure 3.2 further supports the assumption that the differences between CG and AA models shown in Figure 2.10 probably come from backmapping issues, i.e., improper packing of phenyl rings. On the other hand, it also hints that even using parallel tempering methods, atomistic simulations still have sampling problems and cannot reconstruct the high-ordered states.

Figure 3.3 (a) shows the initial CG configuration, set up in an α'' form, as determined by X-ray diffraction experiments [66]. The limiting-ordered α'' form is characterized by a specific positioning of triplets of chains, i.e., one triplet is oriented in one direction, while the other two in the opposite directions. The limiting disordered α' form, on the other hand, has a statistical disorder between these two orientations of triplets of chains. Figure 3.3 (b) shows a representative snapshot obtained from CG-RE simulations at 250 K. We find that all the triplets of chains sampled from the CG model always display the same arrangement of triplets—characteristic of α'—while α'' does not seem stable in the CG model.

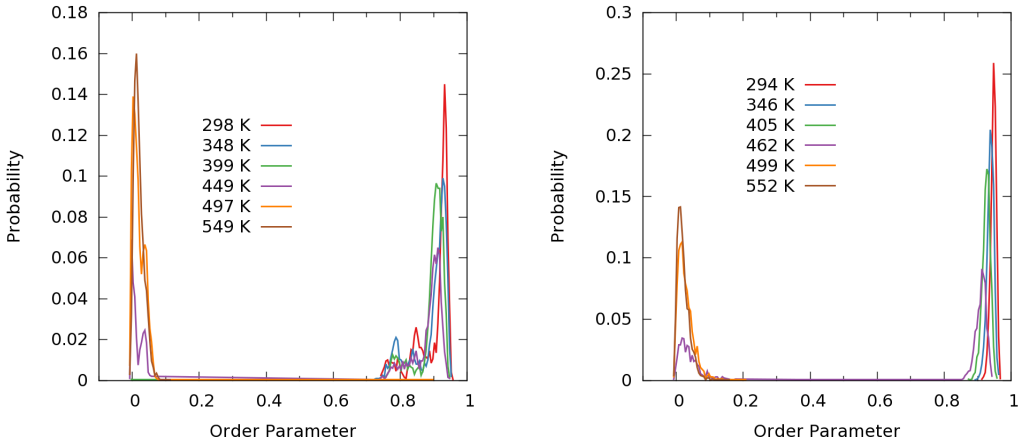

Figure 3.2.: Structural order-parameter distributions as a function of temperature: AA (Left) and CG (Right) simulations starting from α form.

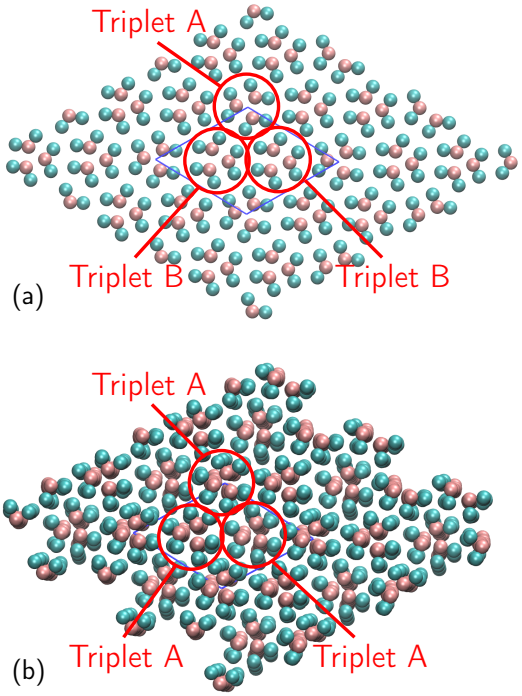

Figure 3.3.: (a) The initial α'' configuration. (b) A representative CG-RE snapshot sampled at 250 K, belonging to the α' form.

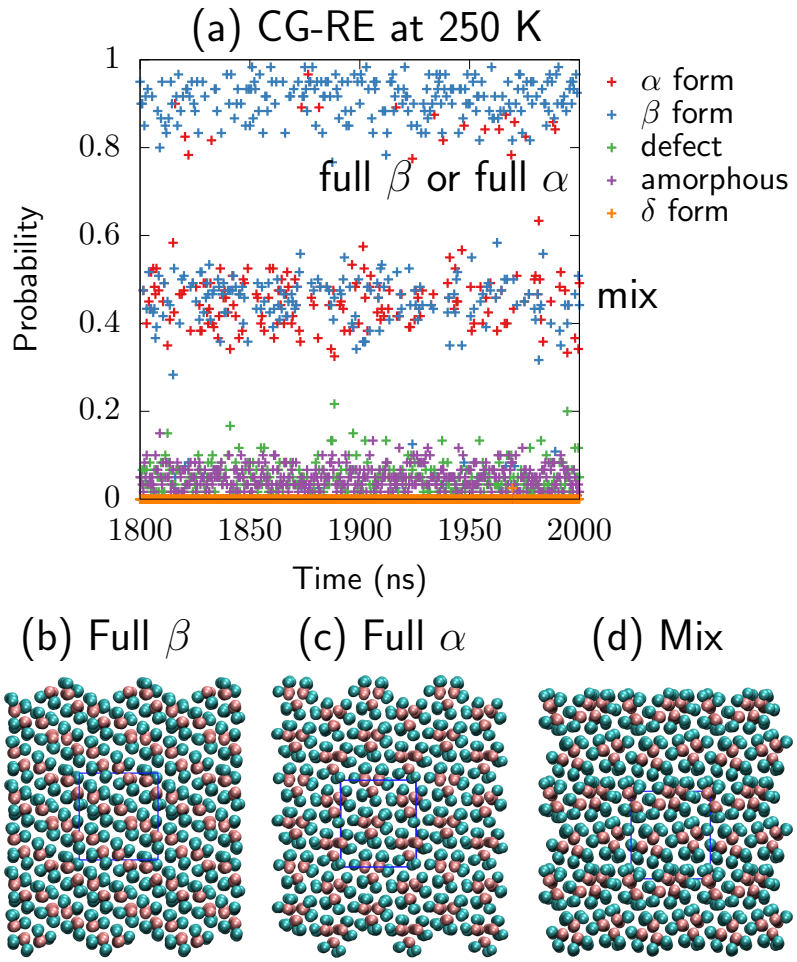

Figure 3.4.: Three polymorphs are observed in CG-RE simulations starting from β form. (a) Distributions of polymorphs in the last 200 ns of the CG-RE simulations at 250 K. (b) Full β, (c) full α, and (d) mixture at 250K.

3.1.2. β form

Figure 3.1 (b) shows the initial β configuration, containing 12 chains of 10 monomers each. We performed PT simulations for the CG and AA models for 2000 ns and 200 ns, respectively. The CG model predominantly stabilizes a mixture of α and β forms below the transition temperature (see Figure 3.1 (b-1)). While many configurations are made of full α or β forms, we also find a significant population that incorporates both, denoted "mix" (Figure 3.4). The presence of α/β mixtures breaks the long-range order expected in homogeneous phases and resembles an intermediate form between the two polymorphs. In fact, the mixtures of α and β forms are often observed experimentally [64, 68, 78–82]. From these experiments, the mixture states are also considered metastable. Thus our results are consistent with the experiments, and in addition offer a structural description of the interface.

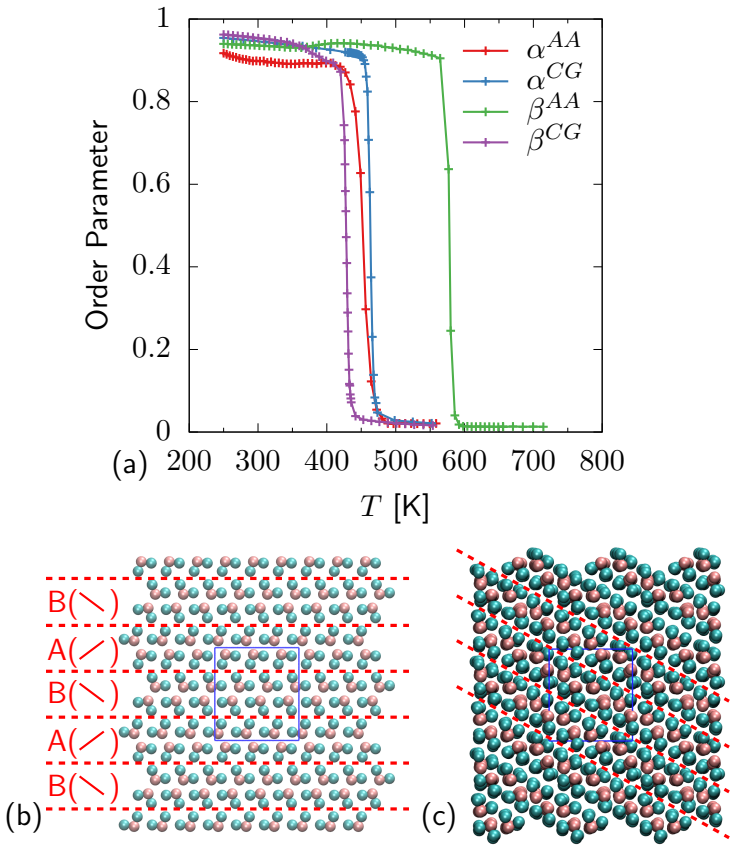

Figure 3.5.: (a) Structural order parameter as a function of temperature calculated from CG and AA REMD simulations. (b) The initial β'' configuration. (c) Representative snapshot obtained from CG-RE simulations at 250 K.

However, atomistic simulation starting from β form exhibit a totally different behavior. No transitions are observed during this AA-PT simulation, and β forms show extremely stable in atomistic model, the same behavior being observed for the α forms. From these two atomistic simulations, we conclude that both forms are stable in the atomistic model, but sampling challenges make it difficult to observe the transitions and more possible phases.

Figure 3.5 (a) shows the order parameter as a function of temperature calculated from CG and AA REMD simulations. Comparing the two resolutions, we find that the transition temperatures agree when simulated in the α-compatible box shape, but not for β. In the CG simulations, the transition temperature of the β^{CG} is around 430 K, roughly 20 K lower than the α form. The AA model shows a similar transition temperature for α (430-450 K), but a significantly more stable β form, with a transition temperature around 600 K.

Experimentally, the crystalline form of melt-crystallized samples is mainly related to the maximum temperature at which the melt is heated up and how long it is kept at that state point. Crystallization of a melt leads preferentially to the α (β) crystals when cooled from

Table 3.2.: Density of s-PS polymorphs (g/cm^3).

Crystal	experiment	AA simulation	CG simulation
α	1.034	1.075	1.098
β	1.08	1.078	1.208
δ	0.977	-	-

low (high) temperatures [79, 80] (See section 1.3.1). The AA model is thus in qualitative agreement with the preferential behavior for β found experimentally.

For CG model, however, it is worth noting that a number of α and mixture phases exist in β^{CG} simulations, which may affect the transition temperature of the system and make it difficult to directly compare the transition temperature. To further study the β form in CG simulations, we compare β configurations that are representative of our CG-RE simulations with the β'' form observed experimentally [69]. Figure 3.5 (b) shows that there are two kinds of bilayers, indicated as A(/) and B(\). The two bilayers are characterized by different orientations of the lines connecting two adjacent phenyl rings inside each chain. The regular succession of bilayers ABAB gives rise to the ordered β'' form, also showing that these two orientations are not parallel to the layer lines. On the other hand, CG configurations have bilayers parallel to the layer lines (Figure 3.5 (c)).

In Section 2.4.2, Figure 2.13 has shown that the density transferability seems poor for crystals. Now the densities of different forms from these new simulations are listed in Table 3.2 and compared with experimental data. It shows that the density depends significantly on the different forms. While the temperature transition of β form shown in Figure 3.5 (a) resulted from the average effect of different phases, here the density of β is calculated only from β phases, discriminated from others. The results show that the AA simulations reproduce the experimental values satisfactorily. The CG results are somewhat larger: While the α form in CG simulations remains in reasonable agreement with both references, the β form is markedly higher.

These results hint at structural deficiencies for the β form in the CG model, both in terms of limited packing orientations (Figure 3.5) and higher density. The possible reason is that in the CG model, the phenyl rings are mapped into spherical beads, which makes difference from π-stacking between the planar side chains in the atomistic model. In addition, the packing of phenyl hydrogens (e.g., T-like stacking) may also affect the resulting phases. It is not yet clear how one would improve the CG model to incorporate these features, without resorting to an entirely new modeling strategy, such as the explicit incorporation of polarization [104].

3.1.3. δ form

Figure 3.1 (c) shows the initial δ form configuration, containing 12 chains with 12 monomers each. RE simulations at the CG and AA level were performed for 1600 ns and 200 ns, respectively. Figure 3.1 (c-1) shows that the δ form is not stable at low temperatures at the CG level—α and β form coexist instead. This phenomenon is consistent with experimental studies, in which δ form (in fact, all helical forms) only stabilize in solvent and will not be stable without solvents during thermal processes. Moreover, the system favors the α form over β at low temperature. In summary, we found that all these CG simulations result in different probabilities of these phases. We suggest that these differences may arise from the limited chain numbers and the fixed box shapes. Experimental results have claimed that formation of the α form may be a kinetically-controlled process [105]. Thus the simulation from δ favors the α form, possibly because the shape of the simulation box is more congruent with the former.

At the AA level, we observed no crystallization (Figure 3.1 (c-2)). Although we do expect the system to eventually crystallize, we suppose that our atomistic simulations—even using PT—did not allow to offer long-enough timescales to reconstruct the crystalline phases. All these atomistic simulations, in which no dynamical exchange among α and β or no crystallization are observed, further suggest the sampling challenge of polymer crystals at an AA resolution. More details of the limitation of PT simulations will be shown in Section 3.3.

3.1.4. Melt structure

From Figure 3.1, we can observe that at high temperatures the system consists of amorphous, defects, and a minor population of δ-type configurations. Note again that δ-type phases here refer to the presence of helical chain segments, while defect correspond to chain segments that are planar but falling out of the α and β forms. A comparison of the melt populations between the two resolutions shows the larger occurrence of planar conformations (i.e., defect) at the CG level. On the other hand, amorphous and helical conformations have a somewhat higher population at the AA level. This indicates that the CG model of sPS tends to favor planar arrangements, due to the simplification of side chains, while the AA model tends to generate more disordered phases because of the complex packing of the phenyl hydrogens. Again, the packing of the phenyl rings may play a role, in accordance with the high density found for β.

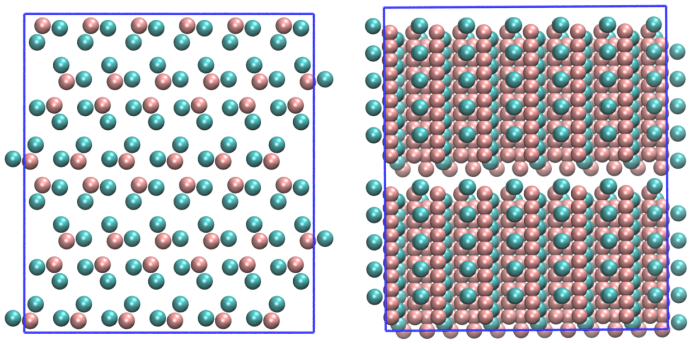

(a) A large system with 96 chains in two layers (β form), whose shape is close to a cubic.

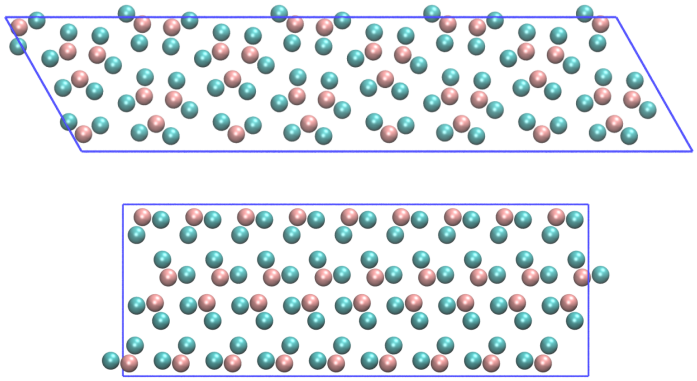

(b) Two large systems with 36 chains. Top: α form; Bottom: β form.

Figure 3.6.: Two PT simulations with large sizes.

3.2. Large system

In the previous sections, we demonstrated that the thermodynamic-based CG model applied here can crystallize and stabilize the main crystalline forms of sPS. However, the results show that the choice of box geometry leads to qualitatively different thermodynamics. Now we consider larger systems, in which the components of box cell are much larger than the twice of cutoff, allowing us to use anisotropic pressure coupling and free angle of box (only for box angle γ, in Table 3.1). Given the sampling difficulties already met at the AA level when using small system size, we only consider CG simulations. Here we performed two PT simulations (See Figure 3.6). One is a system with 96 chains of 10 monomers each, running for 700 ns. This system has two layers, making the simulation box much closer to a cubic shape. Another PT simulation, running for 800 ns, uses two initial structures, α and β form, in replicas alternatively. They all have 36 chains and 10 monomers each, only in one layer. Note that 36 is the smallest possible number of chains that produce the perfect α and β forms simultaneously, as the α unit cell has 9 chains, while β has 4 chains.

Figure 3.7 shows that two simulations with large sizes exhibit different behaviors during crystallization, especially for the transition temperatures. Compared with the small sys-

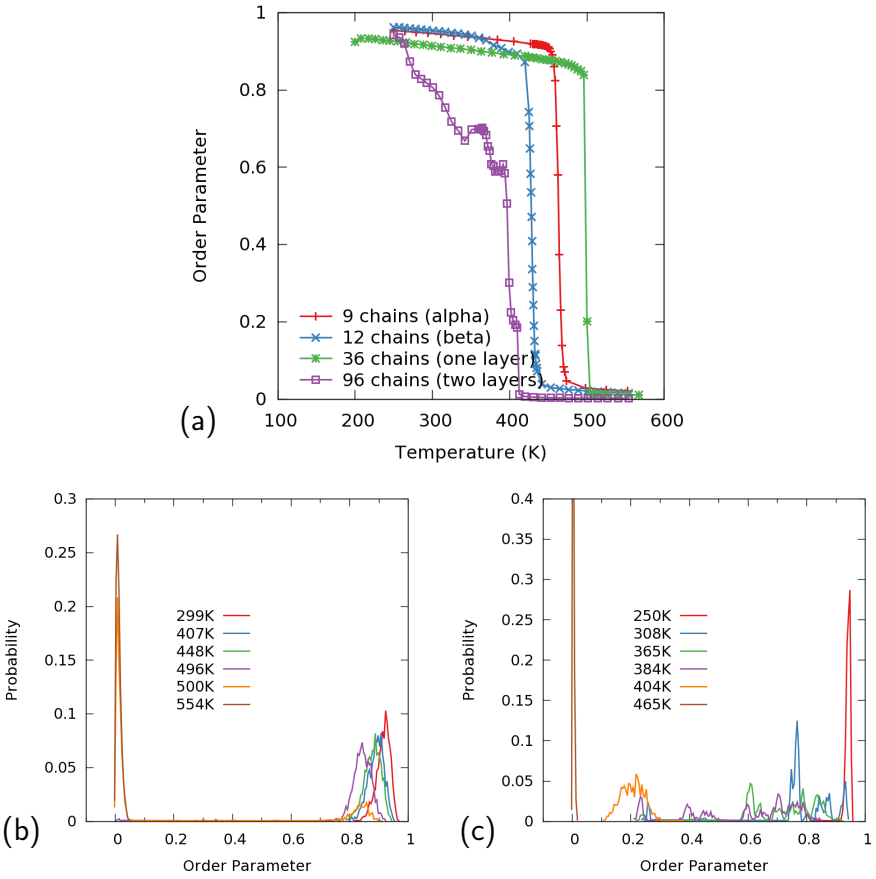

Figure 3.7.: (a) Structural order parameter as a function of temperature calculated from two simulations with large sizes, compared with the small systems. Structural order-parameter distributions at different temperatures: (b) monolayer large system (36 chains) and (c) bilayer large system (96 chains).

tem, the transition temperature of the bilayer system is a slightly lower (∼400 K), while the monolayer system is a bit higher (∼500 K) on the contrary. Moreover, Figure 3.7 (b) shows that the monolayer displays similar order-parameter distributions as in the earlier CG-PT simulations (Figure 2.10 and 3.2). We only observe peaks around 1 and 0, no other intermediate structures existing. However, in the bilayer system (Figure 3.7 (c)), the order-parameter distributions at different temperatures show more structural heterogeneity.

To understand the reason behind these differences, we plot the form probabilities and observe the trajectories during these two simulations. From Figure 3.8 (Left), we see the proportion of α segments is a bit higher than β at low temperature. This result seem inconsistent with experiments, which associates a higher stability to the β form. In fact, full α or β forms, which are observed in the small systems, do not exist in the bilayer system. Figure 3.8 (Right) shows one snapshot starting from the β form, where α, β and

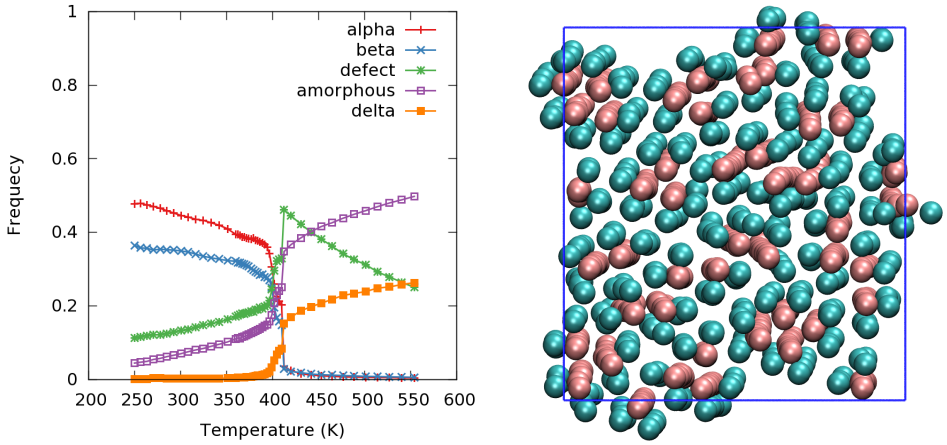

Figure 3.8.: Left: Distributions of polymorphs as a function of temperature obtained from the simulations of the bilayer system; Right: A representative snapshot sampled at 250 K. The mixture phases are stable in this system, while no full α and β forms are observed.

the mixed phases exist simultaneously in the crystalline state. It is worth mentioning that we also performed another simulation starting from the α form (72 chains in two layers), and obtained a similar result—only intermediate phases are observed and the same proportion of α and β forms are shown in these intermediate phases. These results of the bilayer system indicate that they do not depend on the chosen box geometry, but they also cannot stabilize any perfect form, α or β. We suggest that all these phenomena come from the tail effects between the two layers. Due to the short length of the chains, the nonbonded interactions between the two layers significantly affect the stability of α and β forms and make the system tend to the mixed phases. For this reason, we performed another simulation with only one layer, whose simulation box is not limited to an approximate cubic shape.

The monolayer large system, using two initial structures in replicas alternatively, exhibits a completely different behavior. Figure 3.9a shows the averaged probabilities of each type of segments in the first 200 ns (Left) and the last 200 ns (Right). In the beginning of the simulation, we found that the temperature region (under transition temperature) is separated into two parts. All replicas of β tend to travel to a lower temperature region, while α replicas go to a higher region. During the exchange process, the α form disappears gradually, and only the full β form and some intermediate phases remain (Figure 3.9b).

Combining Figure 3.8 and Figure 3.9, now we may explain the difference of the transition temperatures obtained from the two simulations. As mentioned in Section 3.1, we suggest that the transition temperature significantly depends on different phases. Apparently, these two large systems exhibit extremely different phases, which should be the main reason for the different resulting transition temperatures. In addition, compared with β^{CG} (430 K), the transition temperature in the monolayer system (500 K) is closer to the

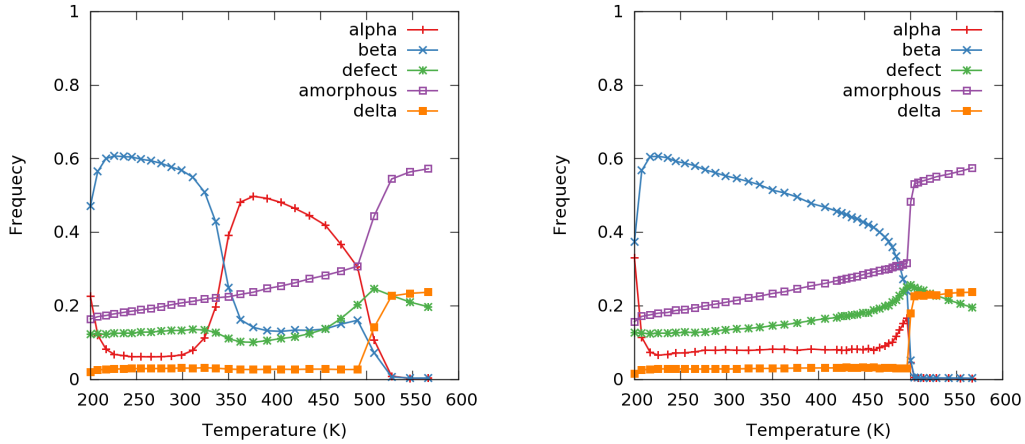

(a) Distributions of polymorphs as a function of temperature obtained from the simulations of the monolayer system. Left: calculated from the first 200 ns of the simulations; Right: from the last 200 ns of the simulations.

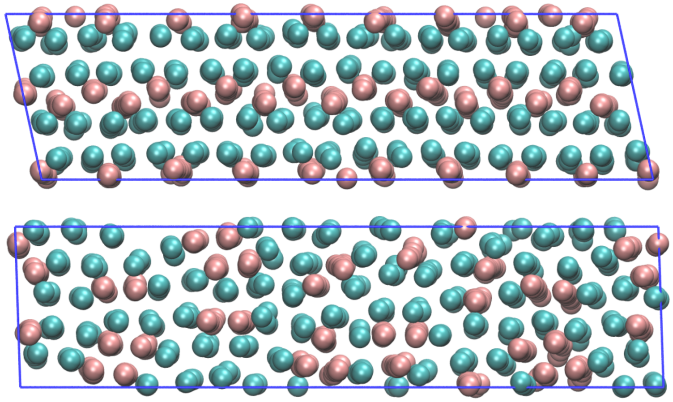

(b) Two representative snapshots sampled at 250 K. Only full β form and some mixture phases exist in the end, and α form disappear gradually.

Figure 3.9.: The resulting structures from PT simulations with 36 chains in one layer.

β^{AA} (600 K) (See Figure 3.5 (a)). This probably results from the fact that the β form dominates in β^{AA} and the monolayer systems, while in β^{CG} many other phases exist. However, the difference between β^{AA} and the CG large systems (monolayer) may comes from many reasons, the size effects, the sampling issues in AA model, and the inaccurate packings in CG model.

3.3. Limitation of parallel tempering simulations

In the previous sections, it has been mentioned that atomistic simulations show a critical sampling issue, even with PT methods. In this section, we will discuss more details about the limitation of PT simulations.

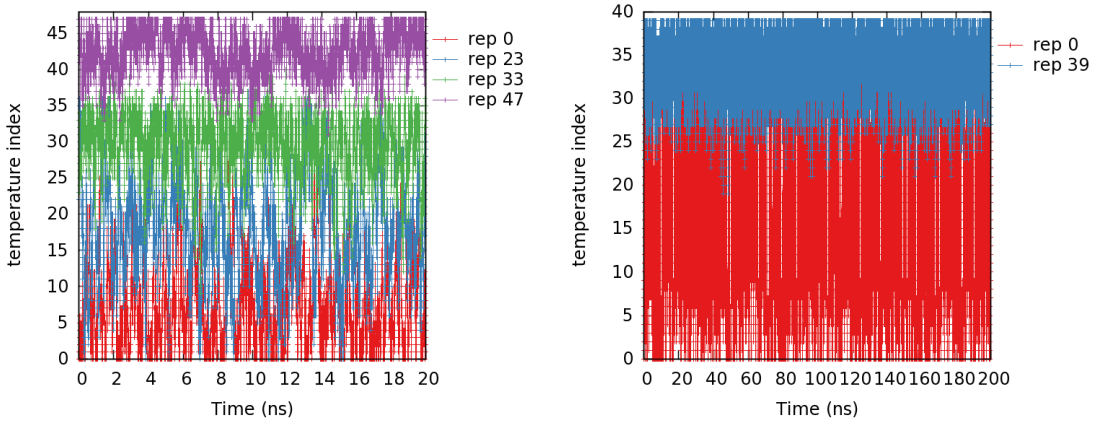

Figure 3.10.: The diffusions in temperature space of the representative replicas in small systems (9 chains). Left: AA-PT simulations; Right: CG-PT simulations.

As introduced in Section 1.2.3, PT methods can be seen as an extension of annealing simulations. The configurations at low temperatures exchange with the ones at high temperatures allow us to explore more possible states, just like a large number of repetitions for cooling and heating processes. At convergence, we can obtain a melting curve without hysteretic behavior (i.e., no cooling rate affect the result). However, it is often hard to confirm the convergence of PT simulations. With increase of the replica number, the computation is increasingly expensive, making the convergence increasingly difficult.

In small system (α form, 9 chains), there are 40 replicas whose temperatures range from 250 K to 550 K in CG-PT simulations, while 48 replicas for the same range in AA-PT simulations. In atomistic simulations, the exchange probabilities are all around 0.6. For the CG model, however, the exchange probabilities are $\sim$0.9 for the region around the transition temperature, and $\sim$0.4 otherwise. Here, we have to add more replicas around the transition temperature, otherwise the exchange probabilities will drop to 0 due to the high barrier between crystals and melts at the CG level.

Even with the high probabilities, Figure 3.10 shows that the temperature diffusion is not satisfactory. As mentioned in Section 1.2.3, the temperature diffusion is a key to validate the efficiency of PT methods. Ideally, it requires that all replicas can traverse the entire temperature ladder. From Figure 3.10, the atomistic simulations are further proven ineffective. Even the transition temperature seem roughly reasonable, the sampling is far from ergodic.

The same also happens in CG model, especially for the large systems (36 chains, Figure 3.11). Here the figure also shows two stages of temperature diffusion, the first 200 ns and the last 200 ns. Combined with Figure 3.9, we assume that the three regions of temperature diffusion, shown in the first 200 ns, may correspond to amorphous, α, and β form (from top to bottom), respectively. Similarly, in the last 200 ns, the three regions correspond to amorphous, β, and (little) mixture phases. These separated regions hint at

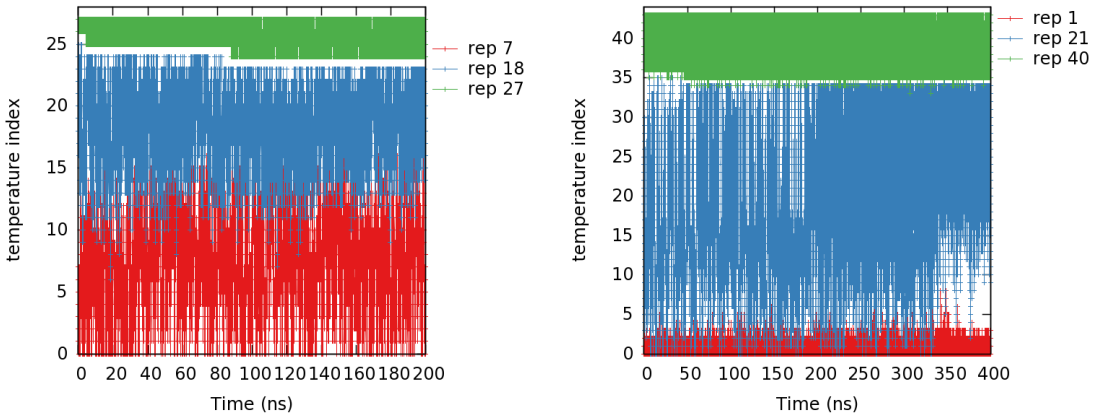

Figure 3.11.: The diffusions in temperature space of the representative replicas in the large system (36 chains). Left: the first 200 ns; Right: the last 200 ns.

the transitions between different phases being extremely weak in large system. For the large system, we expect to find more possible configurations during the PT simulations, but in fact, only few configurations are observed.

In assumption, PT method should allow us to overcome high free-energy barriers by heating the system. However, it fails to cross the first-order phase transition in our work. The limitations show that PT method is not always sufficient, which has also been discussed in other works [50, 57].

The limitation results in an inadequate sampling, from which we cannot truly explore the relative stability of these phases. Hence, in the following parts, we will employ another enhanced sampling method, Metadynamics.

4. Developing Collective Variables

Since the limitation of parallel tempering has been shown in Section 3.3, we now move to another enhanced sampling method, Metadynamics [55, 56] (introduced in Section 1.2.3). This method, unlike parallel tempering, relies on collective variable (CV) biasing, which requires the preliminary identification of a set of CVs. As introduced in Section 1.1.4, CVs are functions of coordinates, and used to describe the process of interest in a reduced space. With the chosen CVs, the free energy landscape can be calculated by

$$F(\boldsymbol{z}) = -k_B T \ln\langle\delta[\boldsymbol{\theta}(\boldsymbol{x}) - \boldsymbol{z}]\rangle, \tag{4.1}$$

where $\boldsymbol{z}$ is the CV space, and $\boldsymbol{\theta}(\boldsymbol{x})$ is a function mapping $\boldsymbol{x}$ to $\boldsymbol{z}$. In fact, for different CV-based methods, the free energy surface is reconstructed by extending this equation in different ways (See Section 1.2.3).

In Metadynamics, sampling is enhanced by adding a bias potential that acts on the selected CVs and force the system to climb the free energy barriers and explore other regions of CV space. The bias is built as a sum of Gaussian functions walking along the CVs. Hence the efficiency of Metadynamics is strongly influenced by the choice of the CVs. A poor choice for CVs can render the results useless for understanding the nature of actual metastable states (i.e., different metastable forms in this work) and the transitions among them.

Ideally the CVs should satisfy three properties [106]:
1. In the CV space, metastable states and transition states must be clearly distinguished as separate regions.
2. The CV space must not contain hidden barriers which are important for transitions and can describe all relevant "slow" processes.
3. The CVs should be limited in numbers, otherwise it will lead a high-dimensional space and take a considerable time to fill the free energy surface.

For the first requirement, as CVs are chosen to provide a low-dimensional description of some important processes among different states, one cannot describe a process without being able to discriminate states. However, it is not always easy to find CVs to do this. The configurations of two metastable states may sample partially overlapping regions of CV space, making ambiguous to which state one representative configuration should be assigned, and thus making the calculated barrier inaccurate. Another possibility is that two representative configurations actually belong to the same state.

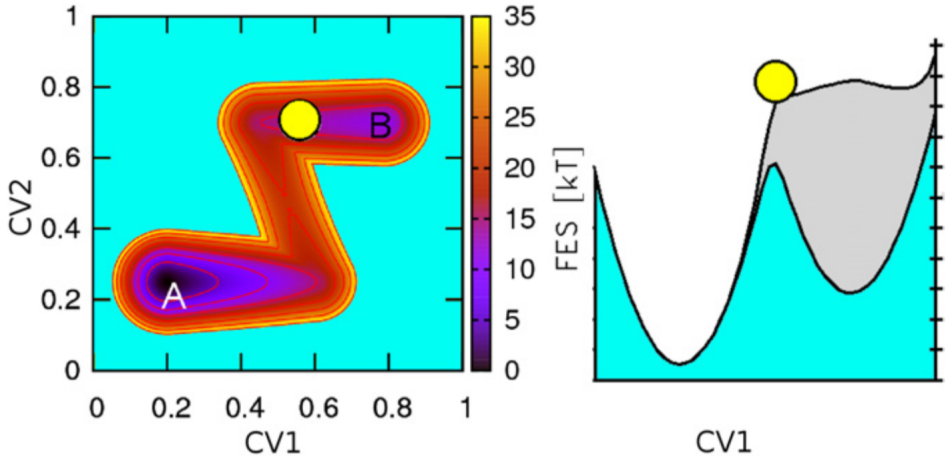

Figure 4.1.: The effect of neglecting a relevant variable. Left: 2D Z-shaped potential. Right: the trajectory of a Metadynamics simulation generated using only CV1, causing strong hysteresis in the constructed free energy. Reprinted from [106] with permission of The Licensor through Copyright Clearance Center (4618980295024).

In the development of CVs, one should balance the second and third requirements. In some simple cases, once we find a set of CVs satisfy the first requirement (i.e., distinguish the difference states), the transitions are easily observed in Metadynamics simulations. If so, for saving the simulating time, we will not consider more CVs. In some cases, however, the chosen CVs seem good enough to distinguish all relevant states, but no transition observed. An example [106] shown in Figure 4.1 is the Z-shaped two-dimensional free energy. If a Metadynamics simulation is performed, biasing only CV1 and neglecting CV2, the simulation is not able to perform a transition from B to A in due time, and Metadynamics goes on overfilling this minimum. This problem just comes from neglecting CV2, even though CV1 has already separated these two states very well. Thus the "slow" process along CV2 is truly important in this case, and we have to use two CVs. From this example, we assume that if there is a significant free energy barrier hiding along some variables we neglected, a Metadynamics simulation may not be able to cross it. Even if the transition is finally observed, the height of the accumulated Gaussians will largely exceed the true barrier height (hysteretic behavior). In the end, the free energy surface calculated from the simulations will be far from the "correct" one.

In practice, unfortunately, these significant barriers are not pre-known, and there is no a priori instruction for finding the proper set of CVs. In many cases we have to proceed by trial and error, attempting several Metadynamics simulations with different combinations of variables. If a "hysteretic behavior" (no or little transitions) is observed in the free energy reconstruction, it may signal the lack of a relevant CV.

In the following of this chapter, we will introduce all CVs tried in this work and make a preliminary evaluation of these CVs by the first requirement (distinguishablity). We first run standard MD simulations (with CG model at 300 K) from different initial structures,

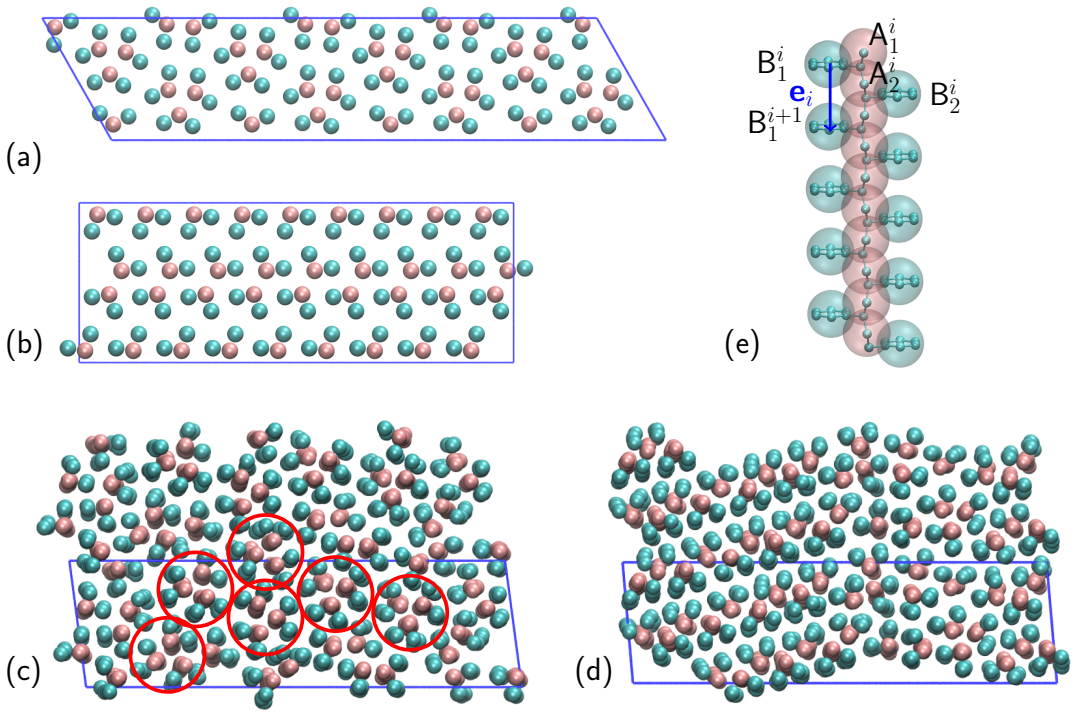

Figure 4.2.: (a) α phase, (b) β phase, (c) "mix1" phase, (d) "mix2" phase, (e) chain conformation of ordered states. "mix1" is close to α phase and "mix2" is close to β. All these four phases exhibit the same chain conformation.

i.e., α, β, "mix1", "mix2" and amorphous (each involves 36 chains of 10 monomers), and generate the equilibrium trajectories for these phases. Then we check if the introduced CVs can distinguish these five phases. Figure 4.2 shows the first four phases. α and β are the main stable phases observed in experiments, while "mix1" and "mix2" are the intermediate phases. In fact, due to the complexity of the system, many other intermediate phases may be discovered during Metadynamics. It is unclear whether the CVs which are testified to differ these five phases can distinguish others. Hence, after the preliminary evaluation in equilibrium trajectories, we will further perform Metadynamics with some combinations of these CVs to check if they can satisfy all three requirements, especially the second one (See Section 5.1).

In this work, we used PLUMED 2.4 [107] to post-process an existing trajectory.

```
plumed driver --plumed plumed.dat --itrr traj.trr
```

To run PLUMED, an input file "plumed.dat" need to be provided. This file will involve constructing one or more collective variables and some analysis of these collective variables. Oftentimes in a complex system, states can only be differed by a global distribution, and thus simple local CVs (e.g. one specific angle or distance somewhere locally) will not be useful. Instead of that, we calculate a number of collective variables for each reference atom or group with its surrounding environment, and then average (or filter)

these local variables for the whole system. In PLUMED, these complex CVs are called "MultiColvars", which can be used to calculate a number of different collective variables. For a guidance, we will show the relevant commands of PLUMED for each CV.

4.1. Order parameter P_2

The nematic order parameter P_2 [108, 109], evaluating order degree of the vectors along the molecule chains, is often used to distinguish crystalline and amorphous phases and thus can detect the crystal growth. In previous work, P_2 has been used to exhibit the melting curves as a function of temperature. In our system, since one racemic diad (i.e., two monomers) is a repeat unit, the evaluated vectors are the ones between two neighboring diads. For instance, identify an orientation vector $\mathbf{e}_i$, pointing from CG bead B_1^i to bead B_1^{i+1} (see Figure 4.2(e)). Similar orientation vectors can be calculated for bead A_1, A_2 and B_2. Then normalize them to unit vectors

$$\mathbf{e}_i = \frac{\mathbf{r}_{i+1} - \mathbf{r}_i}{|\mathbf{r}_{i+1} - \mathbf{r}_i|}. \tag{4.2}$$

For two given orientation vectors $\mathbf{e}_i$ and $\mathbf{e}_j$, the order parameter between them is calculated as follows:

$$P_2^{ij} = \frac{3}{2}(\mathbf{e}_i \cdot \mathbf{e}_j)^2 - \frac{1}{2}. \tag{4.3}$$

Note that, in Chapter 2, we average over all possible P_2^{ij} in whole system as the end result. When we use order parameter P_2 in PLUMED, however, we give a cutoff for each reference vector $\mathbf{e}_i$, averaging all P_2^{ij} in this local environment first. From that, we can get a number of local order parameters, and then average them again for whole system. Local order parameter will require more computation time (the neighbor list updating and repeated calculation for P_2^{ij}), but includes more local details. If one focus on crystal growth, one can filter these local parameters, instead of averaging them, to detect the formation of "baby nuclei" (i.e., a preliminary, local nucleation) [110] .

In PLUMED, P_2 is calculated by a POLYMER_ANGLES action:

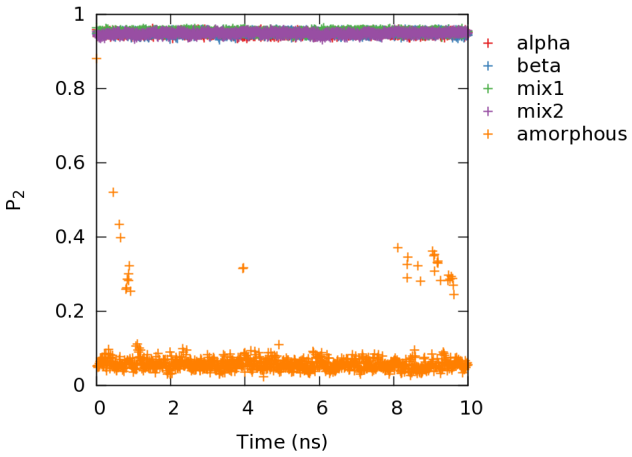

Figure 4.3.: The time evolution of Order parameter P_2 for five different states. α, β, "mix1", "mix2" phases are all close to 1, showing no difference; only amorphous is around 0.

```
MOLECULES ...
MOL1=1,5
MOL2=2,6
MOL3=3,7
(⋮)
MOL576=716,720
LABEL=m3
... MOLECULES

p2: POLYMER_ANGLES SPECIES=m3 LOWMEM SWITCH={RATIONAL R_0=0.75}
MEAN
PRINT STRIDE=1 ARG=p2.mean FILE=colvar
```

"MOLECULES" is an action for calculating the vectors. Above, there are 576 vectors stored in "m3". Then calculate local order parameter for each vector with a cutoff of 0.75 nm. In the end, print the average of all values of local order parameters.

For each phase, we plot the averaged local order parameters P_2 as a function of time. Figure 4.3 shows that except amorphous (close to 0), other phases are all close to 1. There is no difference among these phases. In fact, this is not surprising. From Figure 4.2, we can see all these four states share one chain conformation, and the difference between them only lies in the transversal surface. Since P_2 only refers to the vectors along the chain, it clearly cannot differ any ordered states, including mixture phases. Thus P_2 is a good parameter for detecting crystal growth, but inadequate for telling different crystal phases in our system.

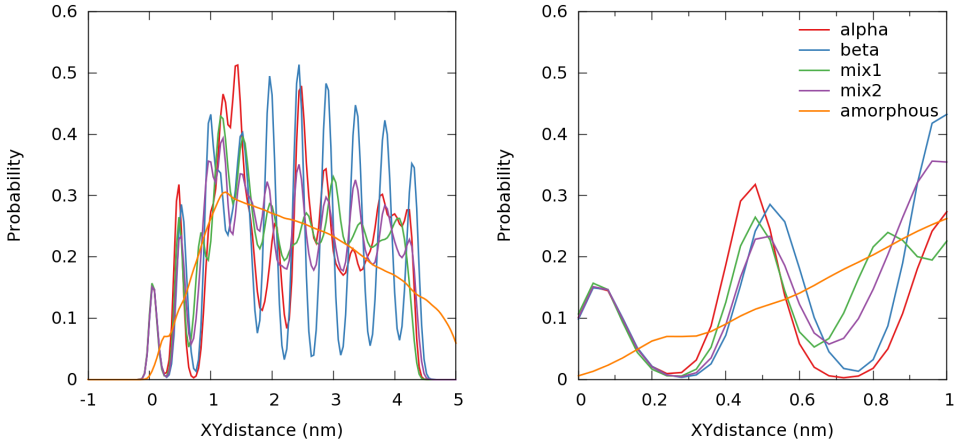

Figure 4.4.: The distribution of XYdistance. XYdistance calculate the distance between a pair of atoms in XY-plane, neglecting the Z-component. Left: the whole distribution; Right: a part of distribution between 0 and 1.

4.2. XYdistance

Since the difference between these ordered states only lies in the transversal surface, we consider the projection of all CG beads onto this surface (XY-plane), neglecting the direction along the chains (Z-axis).

To characterize the difference in the transversal surface, we check the distribution of pair distances for each phase in this XY-plane, called "XYdistance". In Figure 4.4, it exhibits multiple peaks along the XYdistance in different phases, except amorphous. The peaks in β phase are all steep, making a difference from other phases. From these many peaks, however, it is difficult to extract information to differ these phases. Thus we make a filter of the XYdistance (less than 0.75 nm) and then take the average of the distances left, as following commands

```
xydist: XYDISTANCES GROUP=1-720:2
hh: HISTOGRAM DATA=xydist GRID_MIN=-1 GRID_MAX=5 GRID_BIN=150 BAND-
WIDTH=0.05 STRIDE=10
DUMPGRID GRID=hh FILE=histo
xydist1: MFILTER_LESS DATA=xydist SWITCH={GAUSSIAN D_0=0.75 R_0=0.00001}
MEAN
PRINT ARG=xydist1.mean FILE=colvar
```

"GROUP=1-720:2" means we extract every two "atoms" (i.e., bead A) to calculate the distances. All distance values are stored in label "xydist". "HISTOGRAM" and "DUMPGRID" actions can help us plot the distribution histograms, and "MFILTER_LESS" can filter the distances which less than 0.75 nm and stored in "xydist1".

Figure 4.5 shows the average of the filtered XYdistance of bead A. With this CV, we now can see a little difference between α and β, but still cannot tell β and two mixture

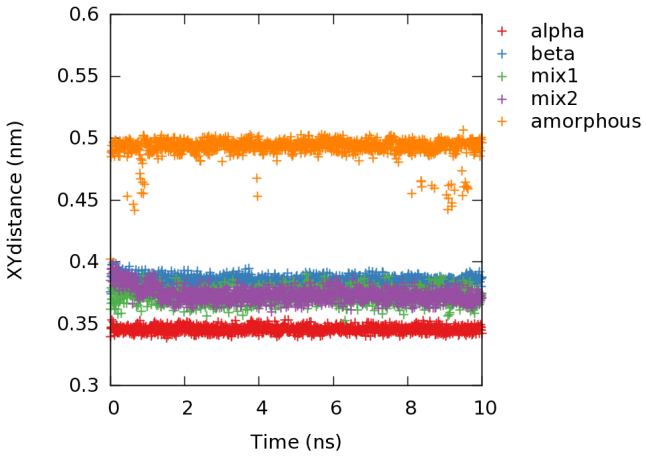

Figure 4.5.: The time evolution of XYdistance.

phases. Clearly, it is not good choice to distinguish different forms due to its complicated distributions.

4.3. Coordination number

Next, we introduce a more general collective variable — coordination number. It is defined as

$$s_{ij} = \frac{1 - \left(\frac{r_{ij} - d_0}{r_0}\right)^n}{1 - \left(\frac{r_{ij} - d_0}{r_0}\right)^m}. \tag{4.4}$$

The function s is approximately 1 for $r - d_0 < r_0$ and goes to zero for large r. Generally, we set $d_0 = 0$, and $n = 6, m = 12$, which is used for tuning the smoothness of the function and its asymptotic behavior for large r.

In fact, using this variable can be considered as a way of indirectly biasing radial distribution functions. Usually, the coordination number is used to detect the presence of bonds in chemical reactions [111, 112], or to count the hydrogen bonds or the hydrophobic contacts [113–115]. In our case, the distances between beads of A type are characterized. To set a proper r_0, we first plot the radial distribution function of bead A (see Figure 4.6). Except amorphous phases, the second peaks for the other four phases are all around 0.5 nm, but they have different heights. Thus we calculate coordination number as follows:

```
cn: COORDINATIONNUMBER SPECIES=1-720:2 SWITCH={RATIONAL R_0=0.5
D_MAX=0.75} MEAN
hh: HISTOGRAM DATA=cn GRID_MIN=0 GRID_MAX=10 GRID_BIN=150 BAND-
WIDTH=0.05 STRIDE=10
DUMPGRID GRID=hh FILE=histo
PRINT ARG=cn.mean FILE=colvar
```

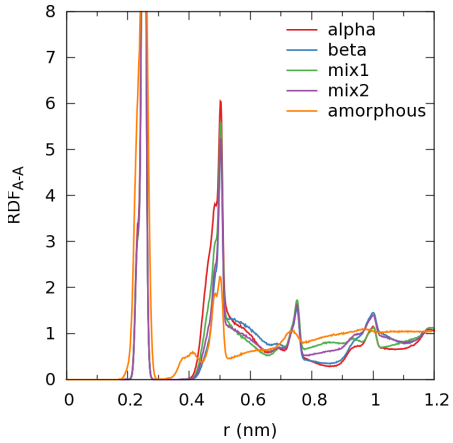

Figure 4.6.: The radial distribution function for bead A, which is for finding a proper r_0.

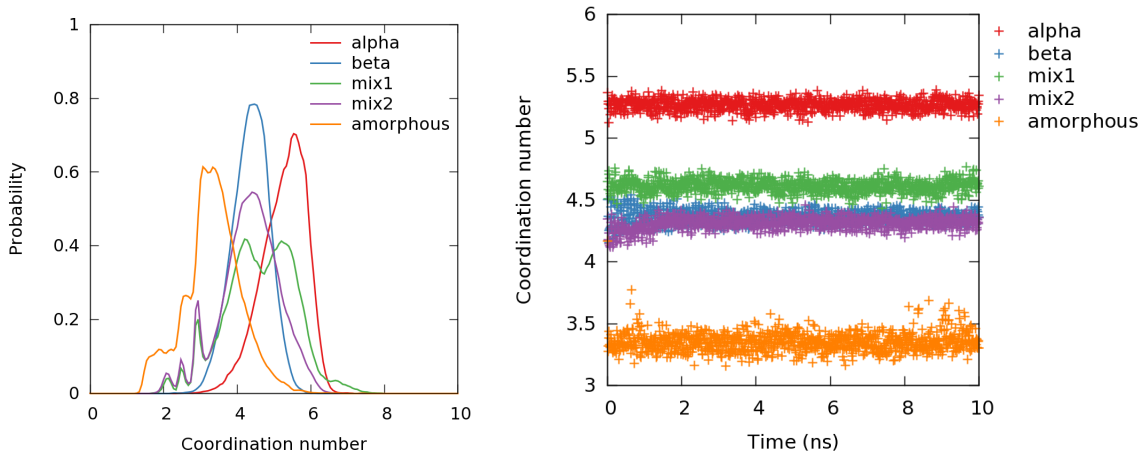

Figure 4.7.: Left: the distribution of coordination number; Right: the time evolution of coordination number.

Here, we set $r_0 = 0.5$ nm and a cutoff at 0.75 nm for each bead A.

With these commands, we get the distribution and the time evolution of averaged coordination number. In Figure 4.7 (left), α, β and amorphous phases have only one main peak at different values. However, there are large overlaps among these phases, especially for β and two mixture phases. After taking the mean of the distributions at each time step, we plot the time evolution of averaged coordination number. Compared to Figure 4.5, coordination number differs α and β much better than XYdistance. Also, the "mix1" phase is separated a bit from β and "mix2" phases. However, it is not sufficient to distinguish all phases. One can imagine, even combining all CVs mentioned above, β and "mix1" phases still cannot be separated.

4.4. Steinhardt parameter Q_6

Steinhardt parameters [116, 117] are order parameters that can describe the spherical symmetry of the system. They quantify orientational order using spherical harmonics computed on the polar angles of each "bond" in the system. Here, the bond is not a covalent bond but simply a vector connecting two beads within a pre-defined coordination radius. This kind of order parameters has been applied in many simulations, spanning from the phase transition of colloidal particles [118] to the nucleation of ice [119] and Lennard-Jones nucleation [120].

In fact, the Steinhardt parameter Q_6 for each particle is a vector whose components are calculated using the following formula:

$$\boldsymbol{q}_{6m}(i) = \frac{\sum_j \sigma(r_{ij}) \boldsymbol{Y}_{6m}(\mathbf{r}_{ij})}{\sum_j \sigma(r_{ij})}, \tag{4.5}$$

where $\{\boldsymbol{Y}_{6m}\}$ are the 6th order spherical harmonics and m runs from -6 to $+6$. With Steinhardt parameter, we do not associate a direction with a particular "bond", but project all vectors onto even spherical harmonics. In Q_6, the vectors are divided into 13 components, and each component is still a vector responding to one harmonic.

These resulting vectors can be used to measure the degree of order in a variety of different ways. The simplest way is to take the norm of these vectors directly:

$$Q_6(i) = \sqrt{\sum_{m=-6}^{6} \boldsymbol{q}_{6m}(i) * \boldsymbol{q}_{6m}(i)}. \tag{4.6}$$

Figure 4.8 shows the distributions of Q_6 calculated in this simple way. The peaks are all too close to tell the difference among the phases. Apparently, their mean values do not provide a way to differentiate the different structural phases.

Thus, instead, we calculate the mean of the vectors $\boldsymbol{q}_{6m}(i)$ and then take the norm of the resulting mean vector, which is called "vmean":

```
q6: Q6 SPECIES=1-720:4 SWITCH={RATIONAL D_0=1.3 R_0=0.2 D_MAX=3.0}
VMEAN
PRINT ARG=q6.vmean FILE=colvar
```

Figure 4.9 shows that with vmean of Q_6, we can separate amorphous and mixture phases from α and β phases. Unfortunately, α and β phases seem to have the same degree of symmetry and cannot be distinguished.

Another way to improve the distinguishing ability of Q_6 is to calculate local Q_6 by taking the dot products between the vector $\boldsymbol{q}_{6m}(i)$ on the reference bead and the vector $\boldsymbol{q}_{6m}(j)$

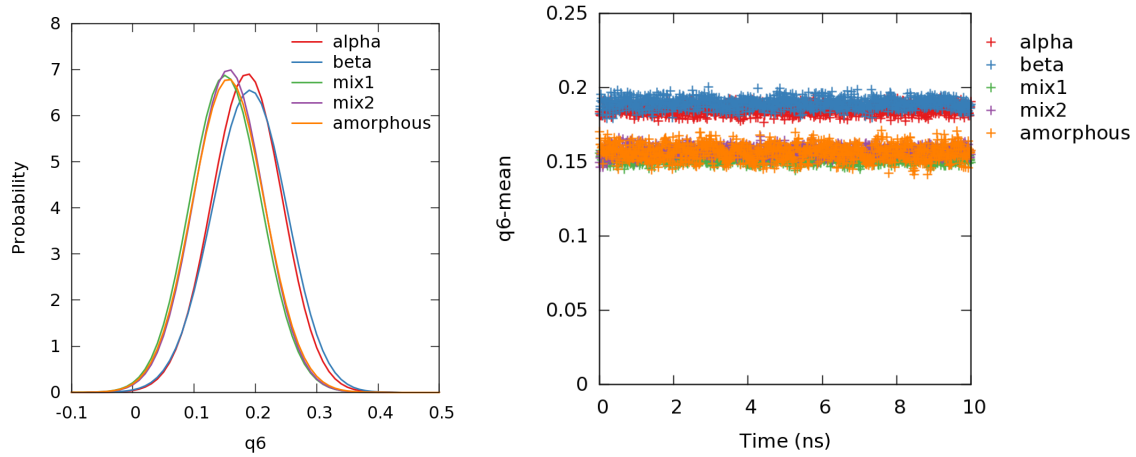

Figure 4.8.: Left: the distribution of mean of Q_6; Right: The time evolution of mean of Q_6, in which the norm of the vectors are taken directly before averaged.

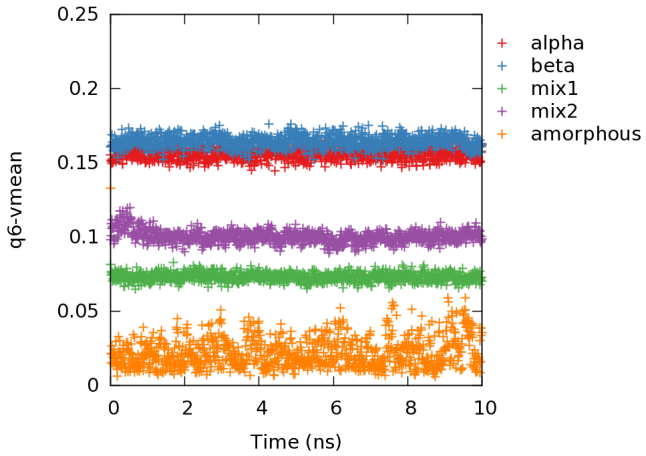

Figure 4.9.: The time evolution of Q_6 vmean, i.e., taking the norm of the mean vector.

on the other beads within the cutoff radius:

$$lq_6(i) = \frac{\sum_j \sigma(r_{ij}) \sum_{m=-6}^{6} \boldsymbol{q}_{6m}(i) * \boldsymbol{q}_{6m}(j)}{\sum_j \sigma(r_{ij})}. \tag{4.7}$$

The result $lq_6(i)$ will be a scalar, not vector any more. The commands for local Q_6 is as following:

```
q6: Q6 SPECIES=1-720:4 SWITCH={RATIONAL D_0=1.3 R_0=0.2 D_MAX=3.0}
lq6: LOCAL_Q6 SPECIES=q6 SWITCH={RATIONAL D_0=1.3 R_0=0.2 D_MAX=3.0}
MEAN
PRINT ARG=lq6.mean FILE=colvar
```

With local Q_6, we can also get a better separation of phases than the first simple one (see Figure 4.10). However, similar to Q_6 vmean, it cannot distinguish between the most important two phases, α and β. Furthermore, due to double neighboring list calculation in Equation 4.5 and Equation 4.7, this local Q_6 is extremely time-consuming in PLUMED ($<$ 1 ns per day even for a small system with only hundreds of monomers) so that we cannot apply it in practice. On the whole, the Steinhardt parameter Q_6 is much more expensive than other CVs, thus here every two bead A (i.e., SPECIES=1-720:4 in the command) is considered to reduce the computation time.

In fact, Q_6 can be considered as an extension of order parameter P_2. P_2 characterize the system restricted in only one component, while Q_6 extend the characterization to 13 components. Q_6 not only measure the order degree of chain direction, but also of the transversal surface. The mixture phases can be seen ordered in chain direction but disordered in the transversal surface, whereas α and β forms show equivalent high ordered in all directions. Hence Q_6 can differ half-ordered phases (two mixture phases) from perfectly-ordered phases (α and β), but cannot further separate them respectively.

As Q_6 cannot distinguish the most important two phases, α and β, that means it will not work if used alone. Even combined with coordination number, one can image the different mixture phases are still ambiguous in CV space. If we want to explore the pathway between α and β, we still need more CVs to distinguish them better and also clearly separate different mixs.

4.5. SMAC

Now we attempt to extract the features of phases in a direct way. Let us carefully observe the transversal surfaces of the α and β forms again. In Figure 4.11, we characterize the orientation of the side chains by the vector from bead A to bead B (taking the center of mass of Bs in two sides), which is named as "molecular vector" in the following. In the perfect α phase the angle between two nearest vectors are always 120°, while the perfect

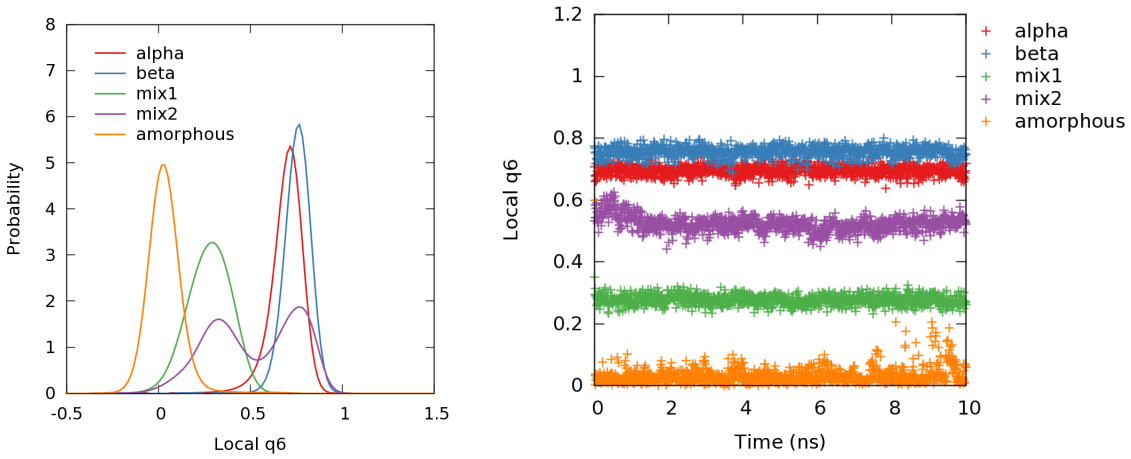

Figure 4.10.: Left: the distribution of Local Q_6; Right: The time evolution of mean of Local Q_6.

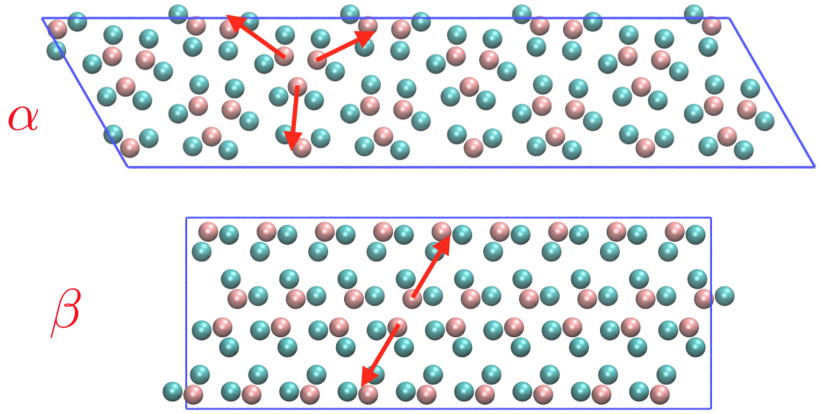

Figure 4.11.: Here shows perfect α and β phases. The vectors represent the orientation of the side chains, pointing from bead A to bead B, called as "molecular vector".

β phase shows 180°.

To make use of these different angles, we introduce another CV, called SMAC [121]:

$$s_i = \frac{\left\{1 - \Psi\left[\sum_{j\neq i}\sigma(r_{ij})\right]\right\}\sum_{j\neq i}\sigma(r_{ij})\sum_n K_n(\theta_{ij}-\theta_n)}{\sum_{j\neq i}\sigma(r_{ij})}, \tag{4.8}$$

where K_n functions are a series of Gaussian functions centered at θ_n.

$$K_n(\theta_{ij}-\theta_n) = e^{-\left((\theta_{ij}-\theta_n)^2/2\sigma_n^2\right)}, \tag{4.9}$$

When all possible angles are at θ_n, K_n will be equal to 1. Thus this CV can be physically interpreted as the fraction of molecules that are locally ordered according to the series of reference angles. We know $\sigma(r_{ij})$ is a switching function for calculation cutoff. In fact, Ψ

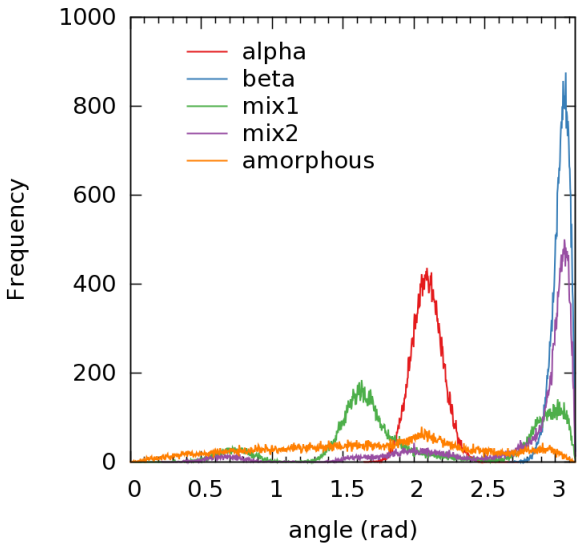

Figure 4.12.: The angle distributions for tuning parameters in SMAC. These angles are the ones between pairs of molecule vectors.

is also a switching function to ensure that those molecules are attached to a reasonably large number of molecules, and here we set this to 3 nm.

To set a proper parameter for SMAC, we first plot the angle distributions for all phases (see Figure 4.12). Note that the angle here is a bending angle between a pair of molecular vectors, while the original SMAC in PLUMED calculates torsion angle. From the figure, α and β forms have only one peak respectively and separately, while amorphous phase is almost flat. The angle distribution of "mix2", close to β form, mostly lie around 3, while "mix1" have two main peaks, center at 1.6 and 3 (rad). Figure 4.2 shows "mix1" is closer to α form, exhibiting many triplets. However, Figure 4.12 shows that the angles of triplets are not perfectly at 120° but around 90°.

Based on Figure 4.12, we first set two Gaussians (i.e., two angle values) in one CV — 1.5 and 3 with sigma 0.2. Commands are as following:

```
c1: CENTER ATOMS=3,7,11,15,19
c2: CENTER ATOMS=2,4,6,8,10,12,14,16,18,20
c3: CENTER ATOMS=23,27,31,35,39
c4: CENTER ATOMS=22,24,26,28,30,32,34,36,38,40
(:)
c71: CENTER ATOMS=703,707,711,715,719
c72: CENTER ATOMS=702,704,706,708,710,712,714,716,718,720

MOLECULES ...
MOL1=c1,c2,c1
MOL2=c3,c4,c3
(:)
MOL36=c71,c72,c71
LABEL=m3
... MOLECULES

SMAC ...
SPECIES=m3 LOWMEM
KERNEL1={GAUSSIAN CENTER=3 SIGMA=0.2} KERNEL2={GAUSSIAN CEN-
TER=1.5 SIGMA=0.2}
SWITCH={RATIONAL R_0=0.75} MEAN SWITCH_COORD={EXP R_0=3.0}
LABEL=s1
... SMAC
PRINT STRIDE=1 ARG=s1.mean FILE=colvar
```

It is worth mentioning that each vector stored in "m3" is an average for the whole molecule, not for one monomer. For convenience, we average the coordinations of beads by "CENTER" action, and then measure the vectors by "MOLECULES" action. In this way, we can avoid calculating the angle between the vectors along the chain, which is redundant and wasteful, and so improve the efficiency of computation. Note that with these averaged "molecular vector", when making a cutoff, one should neglect the distances along chain directions (z-component) and calculate the pair distances only in the transversal surface (i.e., XY-plane). The cutoff is 0.75 nm for only including the nearest pairs.

With these two Gaussians, the resulting SMAC is showed in Figure 4.13. α and β phases are now separated in two ends, and other mixture and amorphous phases in between. It is the first time that amorphous phase lie between α and β phases. It can increase possibility to find new pathways among the phases. For instance, the direct transition between mixture and amorphous phases, which is very likely to occur. Another possibility is that the transition between α and β may only be observed through amorphous phases. It is unclear before performing Metadynamics simulations, thus we have to ensure that the CV space involves all possible processes. However, with only one SMAC, mixture phases are still very close in CV space.

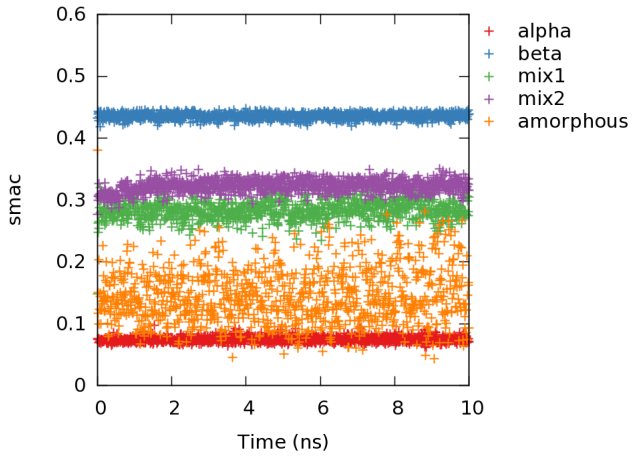

Figure 4.13.: The time evolution of SMAC with two Gaussians at 1.5 and 3 (rad).

We found that setting more Gaussians in one SMAC cannot improve the separation ability, as more Gaussians means that we identify more phases (located in these Gaussians) as the same state. Insight from this, we attempt to calculate individual SMAC for each phase. Here, we choose two phases, α and β, which are more important ones. We set one Gaussian centered at 3 (in radian, for β form), while another one centered at 2.1 (in radian, for α form). Then, instead of setting two Gaussians in one SMAC, we take the difference between these two SMACs, named as "delta" SMAC.

```
SMAC ...
SPECIES=m3 LOWMEM
KERNEL1={GAUSSIAN CENTER=3 SIGMA=0.2}
SWITCH={RATIONAL R_0=0.75} MEAN SWITCH_COORD={EXP R_0=3.0}
LABEL=s1
... SMAC

SMAC ...
SPECIES=m3 LOWMEM
KERNEL1={GAUSSIAN CENTER=2.1 SIGMA=0.2}
SWITCH={RATIONAL R_0=0.75} MEAN SWITCH_COORD={EXP R_0=3.0}
LABEL=s2
... SMAC

delta: COMBINE ARG=s1.mean,s2.mean COEFFICIENTS=1,-1 PERIODIC=NO
PRINT STRIDE=1 ARG=delta FILE=colvar
```

With these commands, for the perfect α, s1 should be 0 and s2 should be 1, while the perfect β is on the contrary. In the end, delta has a range from -1 to 1, where -1 corresponds to α and 1 to β.

In Figure 4.14, this delta parameter shows much better separation of different phases. Note that due to the switching function Ψ, the perfect α and β do not lie in -1 and 1.

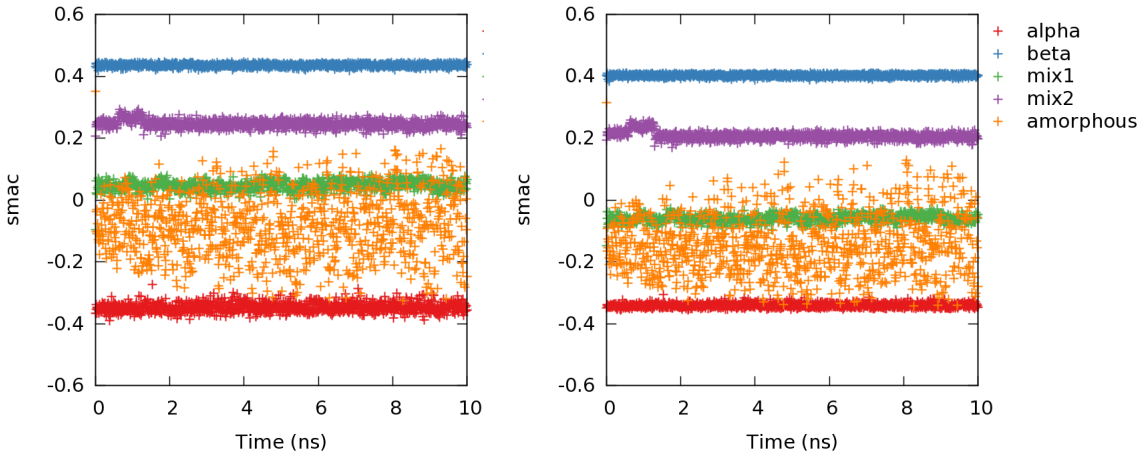

Figure 4.14.: The time evolution of the delta of two SMACs, one is at 3 (rad), another at 2.1 (rad). Left: set two sigmas to 0.2; Right: set two sigmas to 0.45.

When we set Ψ smaller, the delta value will be more close to -1 and 1. Ψ is more like a scaling factor and have no improvement for the distinguishability. Hence we just keep a larger Ψ for controlling the whole system. Here we choose two different sigmas for Gaussian functions. The figure indicates that broader sigma is better, as "mix1" is close to α phase and the delta of "mix1" should be negative. More comparison between these two sigmas during Metadynamics will be shown in Section 5.1.

It is clear that the "delta" SMAC can significantly distinguish the four crystalline phases, which can play a vital role in observing the pathway between α and β phases. It seems adequate if we combine this delta with Q_6, as Q_6 can separate the mixture phases from amorphous. However, we find a "hysteretic behavior" when biasing Metadynamics with these two CVs (more details shown in Section 5.1). In the beginning of this chapter, from Figure 4.1 we conclude that if a "hysteretic behavior" is observed in the free energy reconstruction, it may signal the lack of a relevant CV. Similar to the example in Figure 4.1, all phases can be separated by the combination of Q_6 and the "delta" SMAC, but this CV-space may still lose sight of some important "slow" processes. Thus we will introduce one more CV we used in next section.

4.6. Polymer angle

As mentioned above, we need to find the hidden but key barriers between α and β phases, which leads a "hysteretic behavior". Still, We try to extract the information from "molecular vectors", whose features are more distinct and unambiguous. We consider dealing with these vectors in a way similar to P_2:

$$s_{ij} = \frac{3}{2}(\mathbf{e}_i \cdot \mathbf{e}_j)^2 - \frac{1}{2}. \tag{4.10}$$

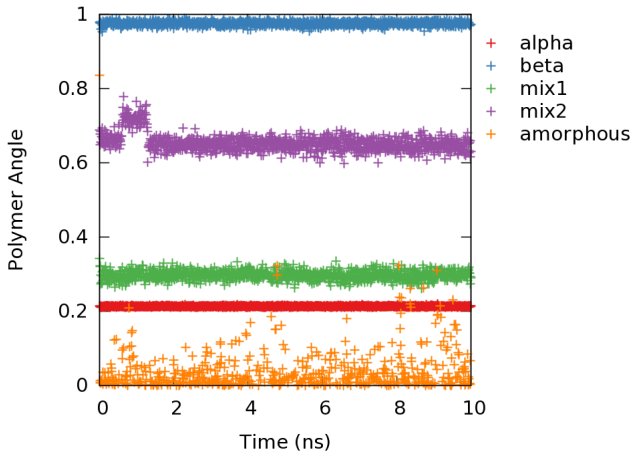

Figure 4.15.: The time evolution of polymer angle.

Note that in this equation, instead of using vectors along the chains, we use "molecular vector" as the vector $\mathbf{e}_i$. In PLUMED file, we use the same "MOLECULES" list with SMAC (denoted as "m3"). The cutoff for these vectors is also calculated in XY-plane, as they are averaged vectors for the whole molecules. "POLYMER_ANGLE" command is also similar to P_2, except the cutoff is set to 3 nm.

```
pa: POLYMER_ANGLES SPECIES=m3 LOWMEM SWITCH={RATIONAL R_0=3.0}
MEAN
PRINT STRIDE=1 ARG=pa.mean FILE=colvar
```

Figure 4.15 shows the time evolution of polymer angle for each phase. Along this CV, the amorphous is at the bottom zero, which is same with Q_6, while mixture phases are between α and β phases, similar to SMAC. But there is a large space for β and β-like (mix2) phases, and a very small difference between α and α-like (mix1) phases. Before running Metadynamics, this large space between β and "mix2" phases was reckoned unnecessary and redundant. However, in next chapter, we will show that it turn out to be a key CV to solve the "hysteretic" problem.

Above, six collective variables have been evaluated. Due to the complexity of the system, it is not surprising that a single CV is difficult to clearly distinguish all phases. Even if it can separate them to some degree, a large barrier which may hide in other dimensions will lead a "hysteretic behavior". In next chapter, we will further evaluate the ability of different combinations of CVs to drive Metadynamics simulations.

5. Probing the free-energy landscape of polymorphs by Metadynamics

In Chapter 3, we have attempted to explore the polymorphism of syndiotactic polystyrene (sPS) using the parallel tempering (PT) method. However, limitations of this method ware identified in this work, especially for large systems. This method show insufficient to overcome high free-energy barriers between polymophs, making it hard to conclude the relative stability of these different forms. Hence we consider another enhanced sampling method, Metadynamics [55, 56], which builds an adaptive bias potential working on the selected CVs and drives the system to overcome possibly high barriers between the states of interest. Note that for now all Metadynamics simulations are performed at CG level, while atomistic Metadynamics simulations are not shown in this thesis and will be considered in our future work.

5.1. Two-dimensional of collective variables

In Chapter 4, we have emphasized the importance of the choice of collective variables (CVs) in Metadynamics simulations and presented three requirements for building a proper CV space. In practice, there is no a priori instruction for choosing the CVs. We have to make a number of trials, and test them one by one in the simulations.

We introduced 6 different CVs and preliminarily evaluated their ability to distinguish five representative phases in equilibrium. In this system, any single CV cannot clearly distinguish all five phases, but some combinations can. However, due to the complexity of the system, other intermediate phases may be discovered during Metadynamics. It is unclear whether these CVs can still recognize them very well during Metadynamics.

Moreover, the second requirement of the CVs (mentioned in Chapter 4) will become more important when driving the system — the CV-space cannot contain hidden barriers. In fact, it is not pre-known where the barriers hide in the system, and thus this requirement can only be checked after the trials of CVs in Metadynamics. We perform Metadynamics with these CV combinations to see if the transitions between the main phases can be observed. As mentioned in Chapter 4, if we find "hysteretic behavior" (no or little transitions) during the simulations, the CV-space is considered unsatisfactory. Hence we

can denote the second requirement as "drivability", which is the property we will mainly focus on in this section.

Here we show three kinds of two-dimensional CV-space: coordination number & SMAC, Q_6 & SMAC, and polymer angle & SMAC. The combinations of three or more CVs are not employed in this work, as it may take more time to fill out the whole CV-space. Another reason is that more CVs will require exceeded memories of computer. To solve this problem, other extended methods (e.g., Bias-exchange Metadynamics [115, 122, 123]) need to be applied.

Note that, to test these CV-space, Well-tempered Metadynamics simulations [58] (See Section 1.2.3) were performed at 200 K starting from α and β forms. During the simulations, more crystalline phases were observed, but no amorphous phase exists. All these simulations were performed using GROMACS 5.1 [124] with PLUMED 2.4 [107]. Here is an example of the commands in "plumed.dat" file:

```
cell: CELL
aaa: COMBINE ARG=cell.ax POWERS=2 PERIODIC=NO
bbb: COMBINE ARG=cell.by POWERS=2 PERIODIC=NO
ccc: COMBINE ARG=cell.cz POWERS=2 PERIODIC=NO
UPPER_WALLS ARG=aaa,bbb,ccc AT=10,10,8 KAPPA=200.0,200.0,200.0 EXP=2,2,2
EPS=1,1,1 OFFSET=0,0,0 LABEL=uwall
LOWER_WALLS ARG=aaa,bbb,ccc AT=5,5,6 KAPPA=200.0,200.0,200.0 EXP=2,2,2
EPS=1,1,1 OFFSET=0,0,0 LABEL=lwall

METAD ...
LABEL=metad
ARG=delta,pa
PACE=500
HEIGHT=3
SIGMA=0.01,0.005
FILE=HILLS
GRID_MIN=-1,-0.2
GRID_MAX=1,1
GRID_BIN=500,500
REWEIGHTING_NGRID=500,500
REWEIGHTING_NHILLS=20
BIASFACTOR=20
TEMP=200
WALKERS_MPI
... METAD

PRINT STRIDE=1000 ARG=delta,pa,metad.* FILE=COLVAR
```

The first part here is to control the box in a reasonable range. In GROMACS, we set anisotropic pressure coupling for the system, thus we have to add an additional control

to make the system stable during Metadynamics.

The second part is to set the parameters for Metadynamics by the "METAD" action. Note that the definition commands for these CVs (See Chapter 4) should be encoded before "METAD" action. Here "BIASFACTOR" and "TEMP" are γ (in Section 1.2.3) and T for Well-tempered Metadynamics. "PACE" is the frequency for Gaussian hill addition, while "HEIGHT" and "SIGMA" is the height and the width of the Gaussian hill, respectively. These Gaussian hills will be recorded in "HILLS" file.

Importantly, "WALKERS_MPI" here illustrates that "multiple walkers" [125] method is used in this simulation. In Metadynamics, we refer to the Gaussian function that explores the CV-space as a walker, while "multiple walkers" means several Gaussians explore simultaneously the same free energy landscape. This method can significantly speed up the convergence of the simulations, as all walkers contribute to a single, combined free energy landscape. In this section, with "WALKERS_MPI" action, 2 walkers were performed in parallel and recorded in the same "HILLS" file. Besides, "REWEIGHTING_NGRID" and "REWEIGHTING_NHILLS" are used to calculate the reweighting factor $c(t)$ for reconstructing a time-independent free energy [60] later. We will discuss more details of these methods in Section 5.2.

5.1.1. Coordination number & SMAC

The first combination we consider is coordination number & "delta" SMAC. In Section 4.5 (Figure 4.14), the "delta" SMAC has been verified to characterize the α, β and mixture phases very well. Thus during the Metadynamics simulations, we can directly recognize the phases from the value of "delta" SMAC (Figure 5.1 (b)).

However, we found that the value of the coordination number becomes more ambiguous in Metadynamics. In fact, Figure 4.7 has shown that in equilibrium the distributions of coordination number already have large overlaps among these phases, but at least it can differ α from others when taking the means of the distributions. From equilibrium, we assume that the mean of coordination number in α form should be $\sim$5.3, while other crystalline phases should be $\sim$4.5. During Metadynamics, however, these reference values are not useful. In Figure 5.1 (a), for example, the α form is between 4 and 5 (walker 0 from 20 ns to 40 ns), while the mixture phase is between 5 and 6 (walker 1 from 60 ns to 80 ns). It hints that in Metadynamics, the coordination number cannot satisfy the first requirement —distinguishability.

Moreover, these ambiguous values will lead to a uninformative free energy landscape — no distinct, separated regions are observed in this CV space (Figure 5.1 (c)). Also, when checking the trajectories, we observe a number of defects in the resulting configurations after 80 ns (Figure 5.1 (d)), which should not be the most stable phases. This is a typical example that shows how an inappropriate CV set will affect the reliability of the free

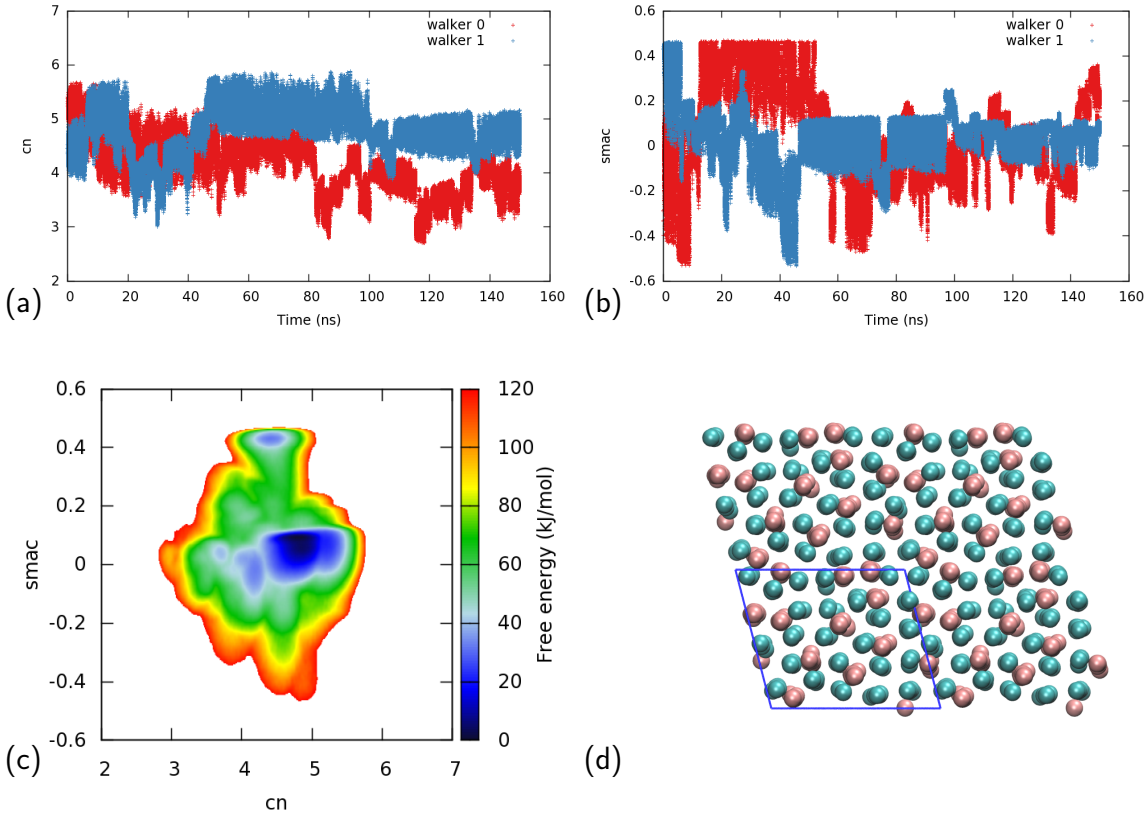

Figure 5.1.: Two-dimensional CV-space: Coordination number & "delta" SMAC. The time evolution of the CVs during the Metadynamics simulations: (a) coordination number; (b) SMAC. (c) Two-dimensional free energy landscape calculated from the simulations. (d) A representative snapshot from the simulations. A number of defects exist in the configurations.

energy calculation in Metadynamics.

5.1.2. Q_6 & SMAC

The second combination is Q_6 & SMAC. To reduce the computation time, we use Q_6 vmean instead of the local Q_6 here (More details in Section 4.4).

To make a comparison, first we show the combination of Q_6 and "old" SMAC, which is the one with two Gaussians at 1.5 and 3 (rad). Figure 5.2 (a) shows the free energy landscape in terms of Q_6 and "old" SMAC. Combining Figure 4.13 and Figure 4.9, we conclude that β form should be at around (0.15,0.4), while α form around (0.15,0.1). When checking the trajectories, however, we found that after 32 ns, walker 1 stay in α form, while these two CVs (Figure 5.2 (b)(c)) do not always locate in the value where they should be at.

Besides, we extract two snapshots from walker 0 (d) and walker 1 (f) at around 45 ns, clearly exhibiting different phases. However, the two walkers have equivalent values for

each CV (Q_6 is between 0.05 and 0.1, while "old" SMAC between 0.3 and 0.4). As mentioned above, walker 1 is in α form here. If one carefully observe the triplets in Figure 5.2 (d), one can find some angles in the triplets are not 120°, but around 90° or 180°. Clearly, this configuration is an α-like form with all triplets, but identified to be a mixture phase in this CV-space.

In Section 4.5, we have shown that the "delta" SMAC can distinguish α and mixture phases much better than the "old" SMAC. In Figure 5.3 (a), the α, β and mixture phases are indeed separated clearly. However, no transitions between α and β forms are observed with this CV-space (Figure 5.3 (b)(c)). In fact, we ran the simulations for 400 ns, but still failed to observe any transitions. This phenomenon is a "hysteretic behavior", similar to the example shown in Figure 4.1. As mentioned above, it means this CV-space is not proper, with a hidden significant barriers neglected.

In the Metadynamics simulations with Q_6 and "old" SMAC, the transition from β to α form was observed (only one transition in 50 ns and no transition from α to β form). In fact, we performed the Metadynamics simulations with Q_6 and polymer angle, but still no transitions were observed. Eventually, we achieved the transitions with the combination of Polymer angle and "delta" SMAC.

5.1.3. Polymer angle & SMAC

Figure 5.4 shows that with the combination of polymer angle and "delta" SMAC, the transitions between α and β form can be achieved. In Section 4.5, two different Gaussian sigmas in "delta" SMAC have been compared preliminarily. The broader sigma show a bit better distiguishability of mixture phases. We found that in the mixture phases, some local regions are similar to α form (triplets), but the angle is not perfectly at 120°. The broader sigma can count in these α-like regions.

Here we further assess the different sigmas during Metadynamics (Figure 5.4). When setting sigmas to 0.2, we observe the first transition from β to α at 200 ns and α to β at 360 ns. When sigmas are 0.45, the first transition is at 60 ns and 120 ns, respectively. From this figure, we can conclude that broader sigmas can improve the phase transitions.

To explain why the combination of polymer angle and SMAC can drive the system more efficiently than others, we performed a longer simulation at 300 K and show the free energy landscape in terms of these two CVs. In this CV space, β form is at $(0.4, 1)$ and α form at $(-0.4, 0.2)$. From Figure 5.5, we can roughly see a kinetic path between α and β forms. Clearly, the path is not linear to the SMAC, and a significant barrier lie at 0.5 along polymer angle, that makes the polymer angle play an undetectable role in Metadynamics.

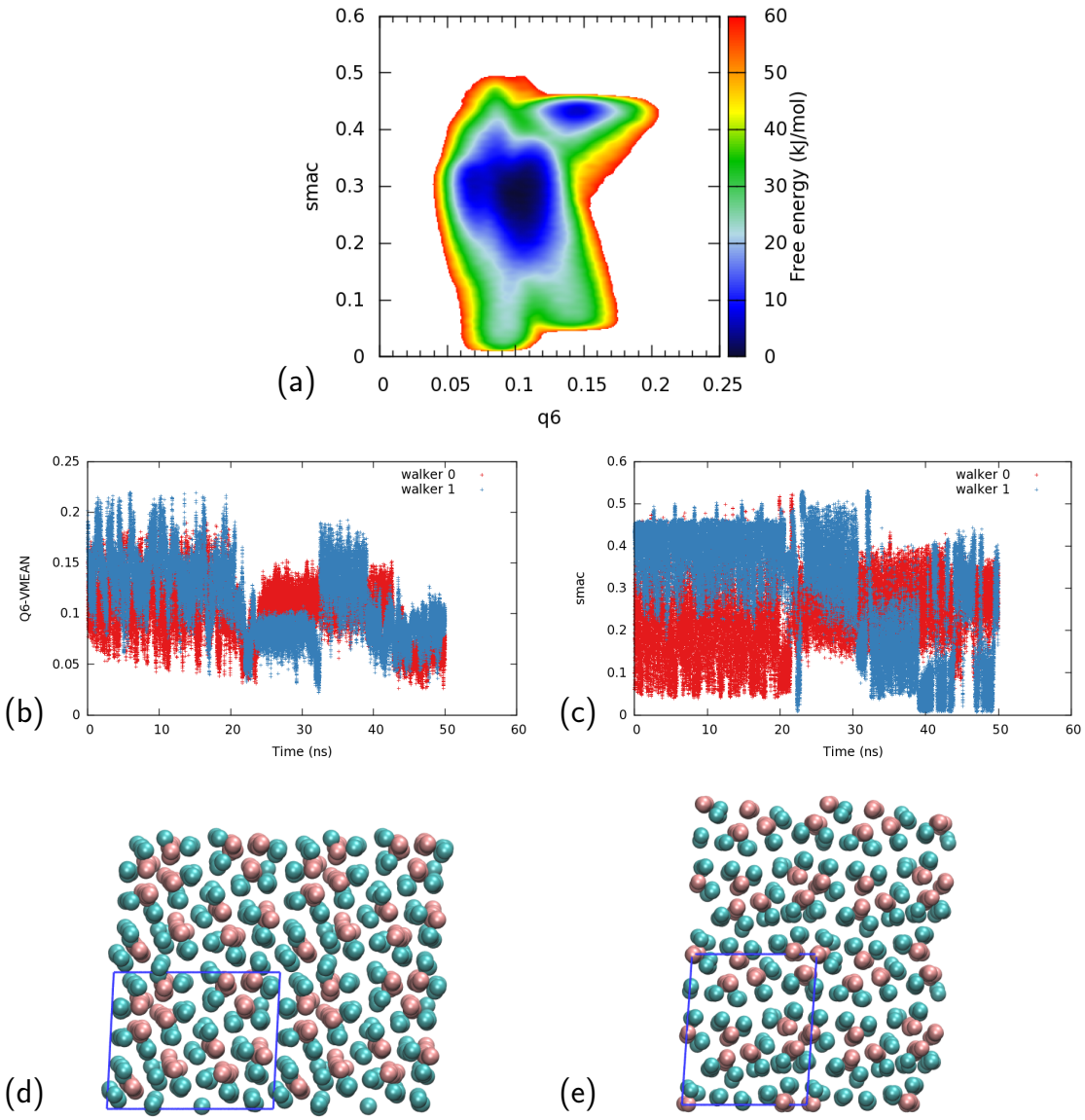

Figure 5.2.: Two-dimensional CV-space: Q_6 & "old" SMAC. (a) Two-dimensional free energy landscape calculated from the Metadynamics simulations. The time evolution of the CVs during the simulations: (b) Q_6; (c) "old" SMAC. Two snapshots from the Metadynamics simulations at around 45 ns: (d) walker 0; (f) walker 1.

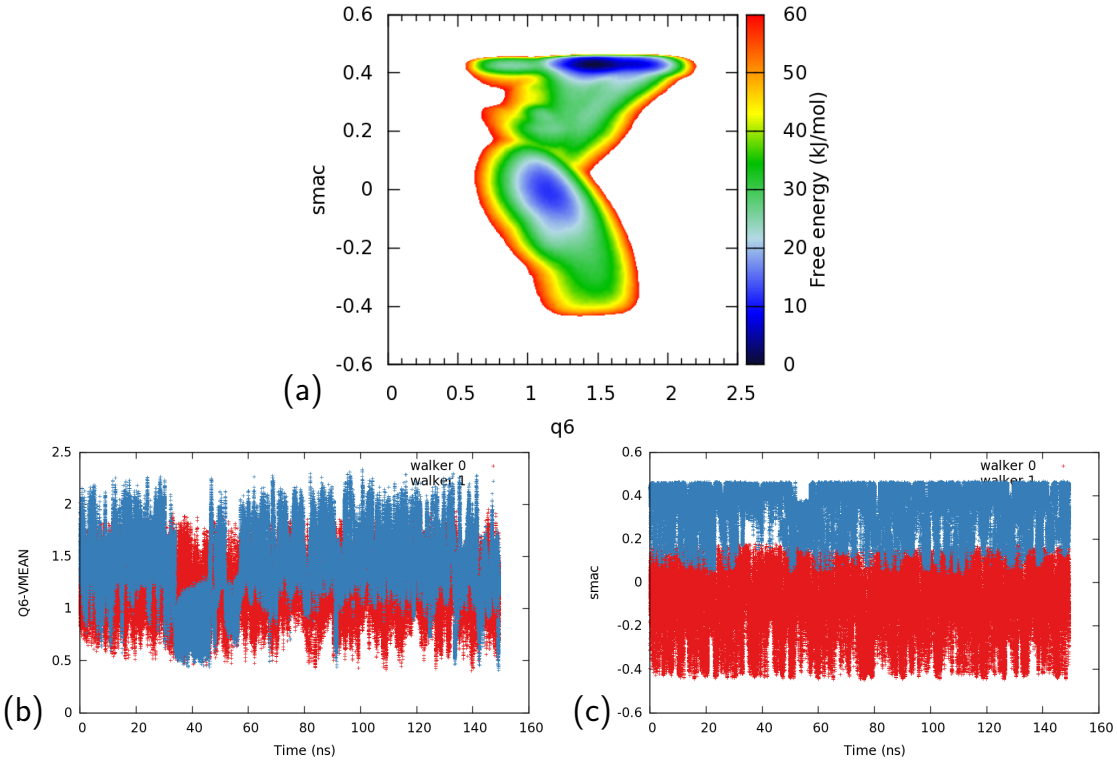

Figure 5.3.: Two-dimensional CV-space: Q_6 & "delta" SMAC. (a) Two-dimensional free energy landscape calculated from the Metadynamics simulations. The time evolution of the CVs during the simulations: (b) Q_6; (c) "delta" SMAC. There is no transition between α and β forms.

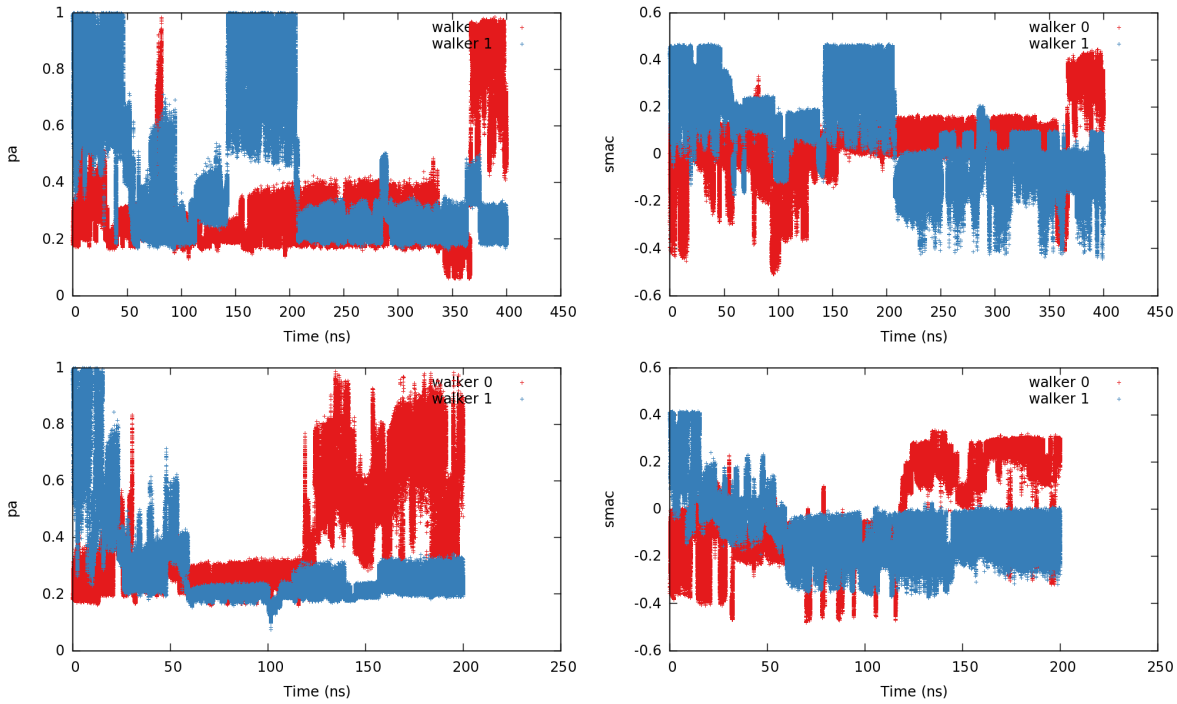

Figure 5.4.: The time evolution of the CVs during Metadynamics with the CV-space: Polymer angle & "delta" SMAC. Top: sigmas are 0.2; Bottom: sigmas are 0.45.

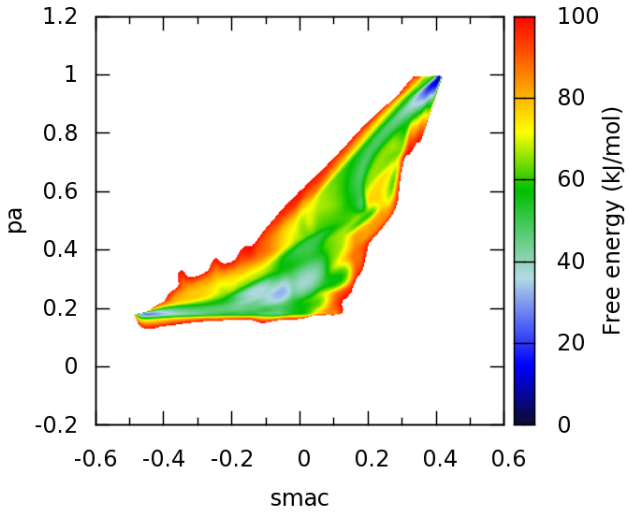

Figure 5.5.: The free energy landscape calculated from Metadyanmics simulations at 300 K.

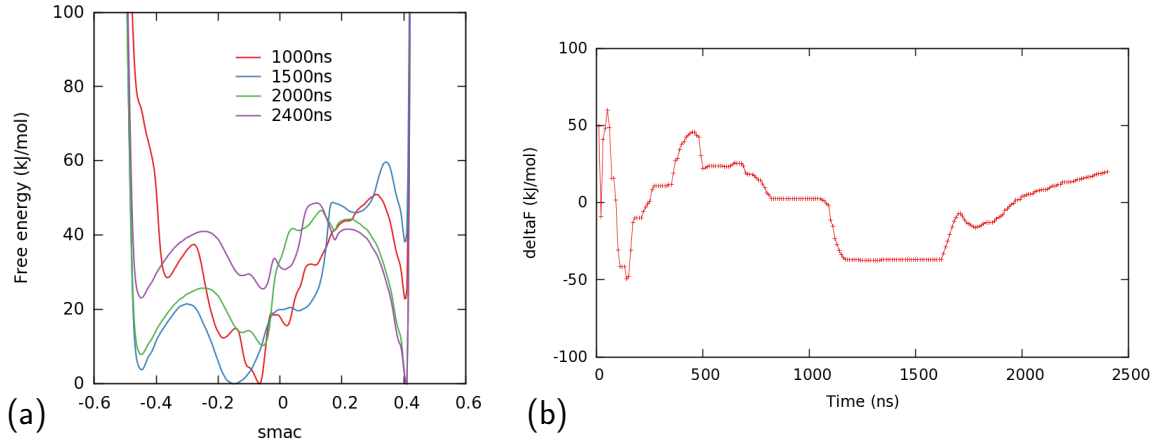

Figure 5.6.: (a) The free energy landscape as a function of SMAC calculated from Metadynamics simulations at different simulating time. (b) the free-energy difference between α and β forms in the free energy surface along SMAC as a function of simulation time.

5.2. Free energy reconstruction

Above, we have found a proper CV-space (polymer angle & "delta" SMAC), which can drive the system to cross the free energy barriers and sample the transitions between α and β forms. In Metadynamics, it is easy to construct free energies by accumulating the Gaussian hills. Figure 5.5 has shown the two-dimensional free energy landscape calculated from the Metadynamics.

In fact, it is also possible to integrate it into a one-dimensional free energy. Here, to assess the convergence of the simulations, we calculate the free energy as a function of SMAC at different simulation time. From Figure 5.6 (a), we can observe that the profiles of free energy are changing with the simulation time and fail to efficiently converge.

To make a clearer assessment, we further calculate the difference of free energy between α and β forms. Figure 5.6 (b) shows the free energy difference as a function of time, which still has large fluctuations even after several microseconds. With the large fluctuations, we cannot conclude the relative stability of polymorphs.

5.2.1. Multiple walkers

To speed up the convergence of Metadynamics, we consider using more walkers in Metadynamics.

Figure 5.7 shows the comparison between 2 walkers and 4 walkers at different temperatures. From the right column (the free energy differences with time), we find that it is

easier to converge for the simulations at higher temperatures (400 K), as the free energy barriers at a high temperature will be smaller than at low temperature.

However, even at 400 K, the fluctuations of the free energy difference are larger than the height of the barriers. It shows the difficulty in reconstructing a steady, reasonable free energy surface. In practice, an important problem which often arises in Metadynamics is to decide when to stop the run, as the resulting free energies from the accumulated Gaussian hills will always fluctuate with the time, even with Well-tempered extension.

5.2.2. Reweighting methods

To make a time-independent free energy reconstruction for Metadynamics, one should use reweighting methods (See Section 1.2.3). Here, we use a reweighting method from Tiwary [60] in PLUMED, Calculating the unbiased statistics by Equation 1.98:

$$P(\boldsymbol{z}) = P_b(\boldsymbol{z}) e^{-\beta[V(\boldsymbol{z},t)-c(t)]}, \tag{5.1}$$

As mentioned in Section 5.1, the reweighting factor $c(t)$ should be calculated during Metadynamics (Equation 1.97):

$$c(t) = \frac{1}{\beta} \log \frac{\int \mathrm{d}\boldsymbol{z} \exp\left[\frac{\gamma}{\gamma-1}\beta V(\boldsymbol{z},t)\right]}{\int \mathrm{d}\boldsymbol{z} \exp\left[\frac{1}{\gamma-1}\beta V(\boldsymbol{z},t)\right]}, \tag{5.2}$$

Then we can reweight the free energy with the values "metad.rbias" recorded in COLVAR files:

```
delta: READ FILE=COLVAR IGNORE_TIME VALUES=delta
mtd: READ FILE=COLVAR IGNORE_TIME VALUES=metad.rbias
weights1: REWEIGHT_BIAS TEMP=300 ARG=mtd.rbias

HISTOGRAM ...
ARG=delta
GRID_MIN=-1
GRID_MAX=1
GRID_BIN=500
BANDWIDTH=0.01
LOGWEIGHTS=weights1
LABEL=deltahist
... HISTOGRAM

CONVERT_TO_FES GRID=deltahist TEMP=300 LABEL=deltafes
DUMPGRID GRID=deltafes FILE=fes_delta_reweight.dat
```

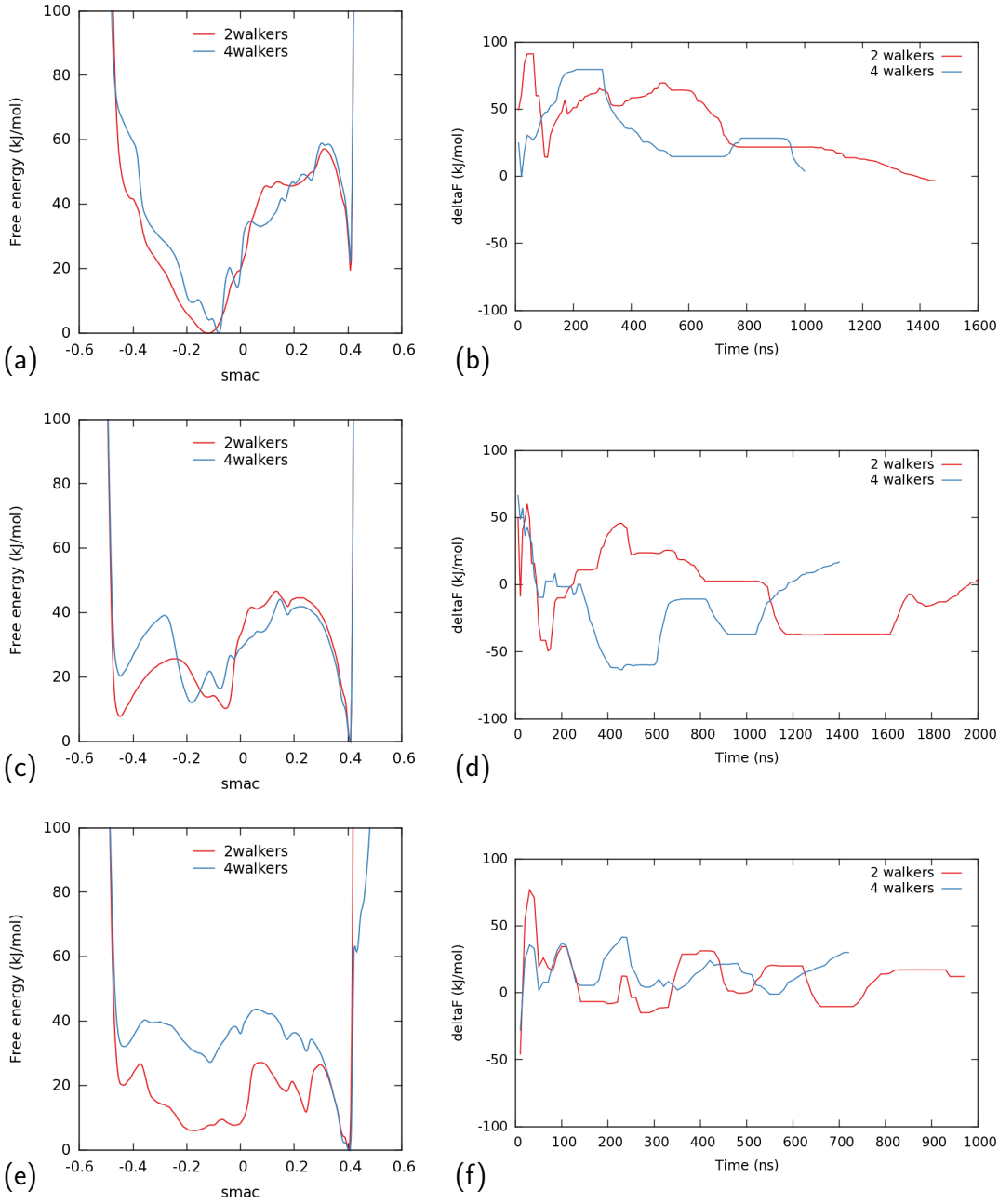

Figure 5.7.: The comparison between 2 walkers and 4 walkers at different temperatures: Top: 200 K; Middle: 300 K; Bottom: 400 K. Left: The free energy landscape as a function of SMAC. Right: the free-energy difference between α and β forms in the free energy surface along SMAC as a function of simulation time.

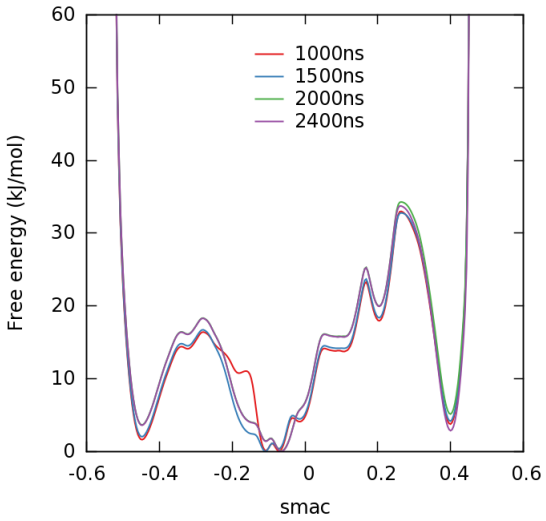

Figure 5.8.: The free energy landscape as a function of SMAC reconstructed through the reweighting method at different simulation time.

Here metad.rbias $= V(\boldsymbol{z}, t) - c(t)$. Figure 5.8 shows that with reweighting, the profiles of free energy barely change after 1500 ns. Compared with the free energy directly from bias potential (Figure 5.6), the reweighting results are converged and thus more reliable. With this converged results, we now can observe the relative stability of phases along SMAC. These will be discussed in Section 5.3.

However, when checking the reweighting result for different numbers of walkers and at different temperatures, we still observe the convergence problem at high temperatures (Figure 5.9), especially for 4 walkers. From (c), we can see that the free energy profile calculated from 4 walkers (at 300 K) is extremely different from others. An abnormal time evolution of free energy difference is exhibited in (d) for 4 walkers. Similar behavior is shown at 400 K.

To find the reason, we checked the trajectories of the simulations and expectedly, the system will attempt to explore more regions during Metadynamics, and also reach amorphous phase. When they are forced to transition back to the crystalline phases, the chain directions are changed to another direction, not our default one (along z-component), shown in Figure 5.10. It leads to artifacts in the CV analysis, as the SMAC and polymer angle are all using cutoff only in XY-plane. It has been mentioned in Section 4.5 that the "molecular vectors" are averaged over the whole molecules, in which we use a plane cutoff and ignore the distance along the chain direction. With this setting, we can significantly speed up the CV calculations. With the averaging protocol, polymer angle still can distinguish the amorphous phases from others. However, when the system is in the crystalline states, we should make sure that the chains always direct along the z-component, because it is not convenient to change the cutoff setting during the simulations. One possible way to solve this problem is controlling the system by adding a new restraint CV, which does

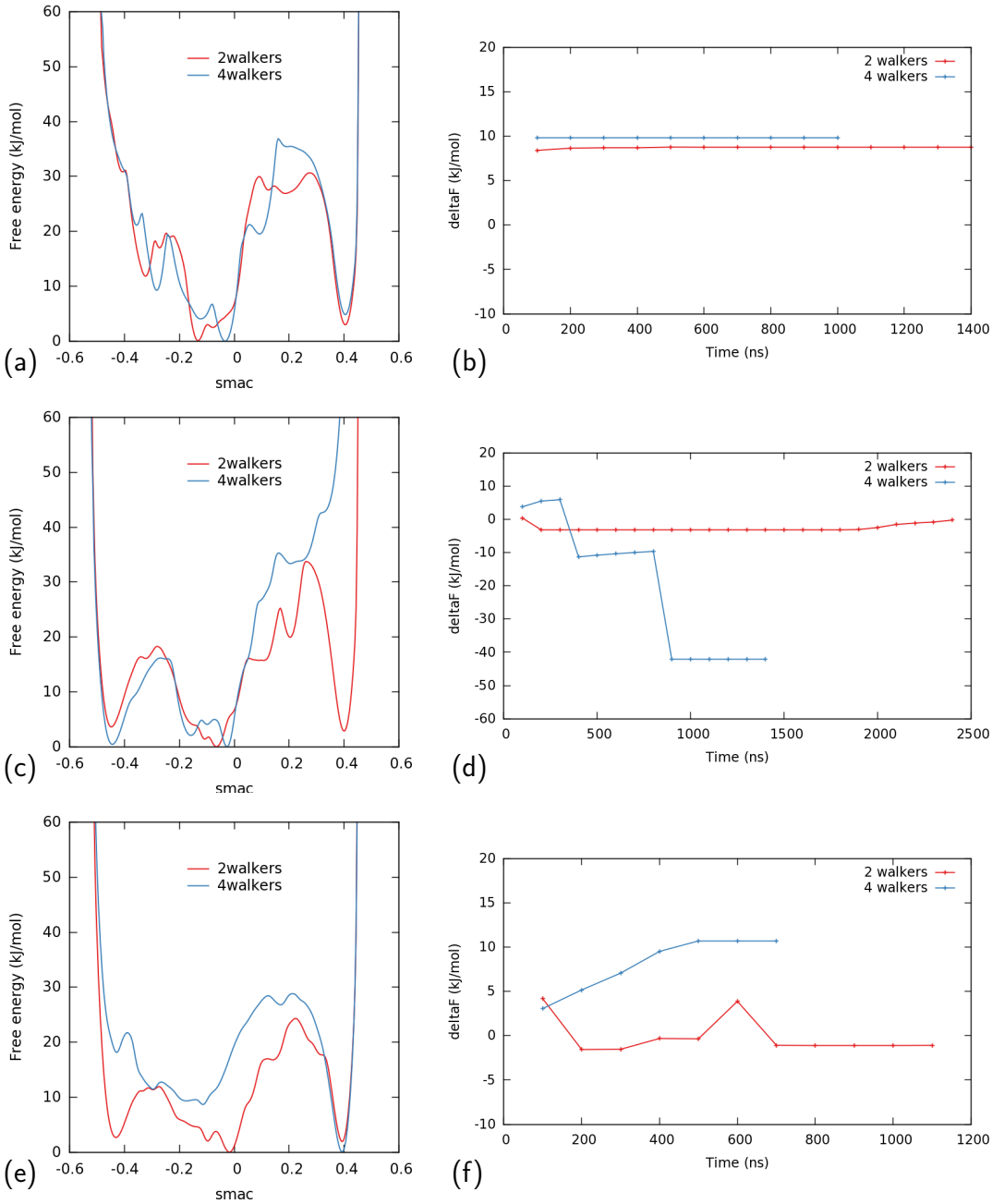

Figure 5.9.: Free energy reconstruction through reweighting. The comparison between 2 walkers and 4 walkers at different temperatures: Top: 200 K; Middle: 300 K; Bottom: 400 K. Left: The free energy landscape as a function of SMAC. Right: the free-energy difference between α and β forms in the free energy surface along SMAC as a function of simulation time.

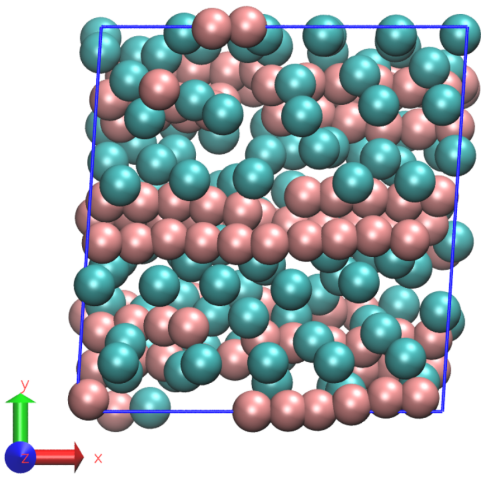

Figure 5.10.: A representative snapshot to show how the chains direct along y-component, which leads a wrong result.

not work for driving Metadynamics but only restrain the system at a certain range. (will be discussed in next Section 5.2.3).

It is worth mentioning that this abnormal behavior is only detected by reweighting, as it is a smarter way to reconstruct the free energy. By directly summing the hills, the strong fluctuations of the resulting free energies makes the problem hidden. In addition, as the system stays in crystalline phases at 200 K, the chains always direct along z-component, and thus the result seem to converge when reweighting. However, the temperature of 200 K is too low to compared with experimental data. Moreover, the low temperature may lead to an incomplete sampling of the CV-space, even if it seems converged. Using this low temperature help ensure that the system stays in crystalline phases and make it more convenient to evaluate the CVs. In next Section 5.2.3, we will focus on higher temperatures with an additional control of the chain directions.

5.2.3. Additional restraint CV

Above, it has been shown that the wrong chain directions will lead to an unreasonable free energy landscape, due to the incorrect calculation of SMAC and polymer angles with wrong cutoff. Here, we show another example at 400 K in Figure 5.11. Without controlling the chain directions, the values of SMAC and polymer angle may be wrong. In the CV-space, there should not exist any metastable phases at (0,1) or (0.3,0.2). SMAC at 0 means mixture or amorphous phases, which cannot get a value of 1 in polymer angle, while SMAC at 0.3 means β-like phases, which should get a value around 1 in polymer angle.

To solve this severe problem, we have to find a way to control the chain directions. We

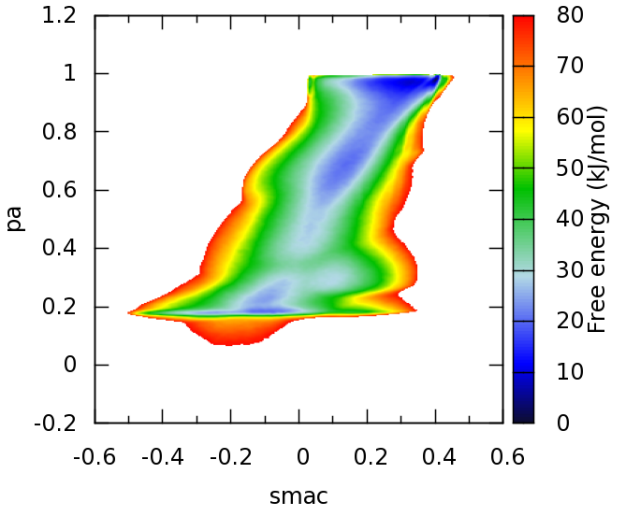

Figure 5.11.: The free energy landscape calculated from Metadyanmics simulations at 400 K. Without an additional control, the result is extremely abnormal.

first use P_2 order parameter to control the system. We expect that if we can control the system not to explore the amorphous regions, then the chains will stay in the same direction. In fact, the free energy reconstructions at 400 K shown in Figure 5.7 and 5.9 result from P_2 control. It is why 400 K show a bit better convergence than 300 K, which is without any additional control. In the simulations at 400 K, we attempt to restraint P_2 larger than 0.6. The P_2 control works in the 2-walker simulations but fails in the 4-walker simulations, probably because the 4-walker simulations have a faster exploration of a CV-space, making the system faster to obtain amorphous phase and then go to wrong directions. The P_2 only control the order degree of the system and cannot make sure that the chain directions are along z-component.

In the end, we found another CV which can directly control the chain directions — Zangle. This CV calculates the angles between the vectors and the z-component. Thus we can calculate the vectors along the chains and restrain them at the same direction with z-component, i.e., restrain the angles to 0. The following are the command lines for calculating the Zangle.

```
WHOLEMOLECULES ...
ENTITY0=1-20
ENTITY1=21-40
ENTITY2=41-60
(:)
ENTITY11=221-240
... WHOLEMOLECULES

ZANGLES ...
ATOMS1=1,19
ATOMS2=21,39
ATOMS3=41,59
(:)
ATOMS12=221,239
MEAN NOPBC
LABEL=za
... ZANGLES

PRINT STRIDE=1 ARG=za.mean FILE=COLVAR
```

Note that when calculating the Zangles, we ignore the periodic boundary conditions by "NOPBC" and use "WHOLEMOLECULES" to rebuild the molecules into complete ones. In this way, we define a vector pointing from the head to the tail for each molecule. Then take an average of all angles between the vectors and z-component.

Figure 5.12 shows the Zangle mean as a function of time, which is calculated from 4-walker simulations at 400 K with a control in P_2. It can clearly detect whether the chains are along z-component. From the figure, P_2 proves unable to control the chain directions. The walker 0 shows along another direction after 500 ns, which can be related to the divergent behavior in free energy difference shown in Figure 5.9 (d).

Hence in the following simulations, we add a restraint directly in Zangle:

```
UPPER_WALLS ARG=aaa,bbb,ccc,za.mean AT=9,9,8,0.5 KAPPA=200,200,200,200
EXP=2,2,2,2 EPS=1,1,1,1 OFFSET=0,0,0,0 LABEL=uwall
LOWER_WALLS ARG=aaa,bbb,ccc AT=5,5,6 KAPPA=200,200,200 EXP=2,2,2
EPS=1,1,1 OFFSET=0,0,0 LABEL=lwall
```

We set an "UPPER_WALLS" for the value of "za.mean" to constrain the mean of angle always smaller than 0.5, which shows much more efficient than P_2. Besides, it will not hinder the system to explore the amorphous phase, which makes the result more reasonable at high temperatures.

It is found that restraining the conformational space is necessary to lead to more stable simulations, even at higher temperatures (e.g., 500 K). Figure 5.13 shows the free energy landscape along SMAC by reweighting from the Metadynamics simulations with zangle

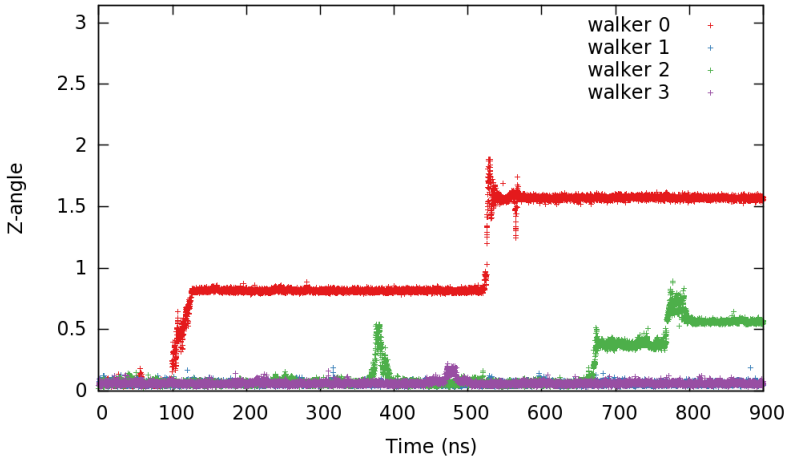

Figure 5.12.: The time evolution of Zangle mean calculated from the 4-walker simulations at 400 K with a control in P_2.

control. For now, these simulations are not converged yet due to the limited simulation time (around 500 ns), and the extension of these simulations will be the subject of future work.

At 400 K and 450 K, the highest barriers in the free energy landscape are almost equivalent for different numbers of walkers. At 300 K and 500 K, it shows highly differences between 2 walkers and 4 walkers. We infer that with 2 walkers, the systems get stuck in local minima, mixture and amorphous phases at 300 K and 500 K, respectively, while 4 walkers can enhance the exploration ability of CV-space and climb out of the local minima.

5.3. Crystal Stability

Due to the limited simulation time, we cannot obtain a totally converged free energy landscape, but it is expected to roughly show the stability of polymorphs. It has shown that Metadynamics can indeed work in this system, and our CVs can overcome the large free energy barriers and enhance the transition between different forms, which is difficult to be observed in standard MD simulations. On the whole, we can find that β form is likely to be more stable than α form, especially between 400 K and 450 K, which is consistent with the experimental results [126]. In addition, the heighest barriers along SMAC often locate in $\sim$0.2, which are between the mixture/amorphous phases and β form, while the barriers between the mixture/amorphous phases and α form are a bit lower. It can help us to understand the kinetic trap behavior of α form mentioned in experimental paper [126]. The β form is more stable in whole CV-space, but α form is easier to reach from the mixture or amorphous phases. It is worth mentioning that some

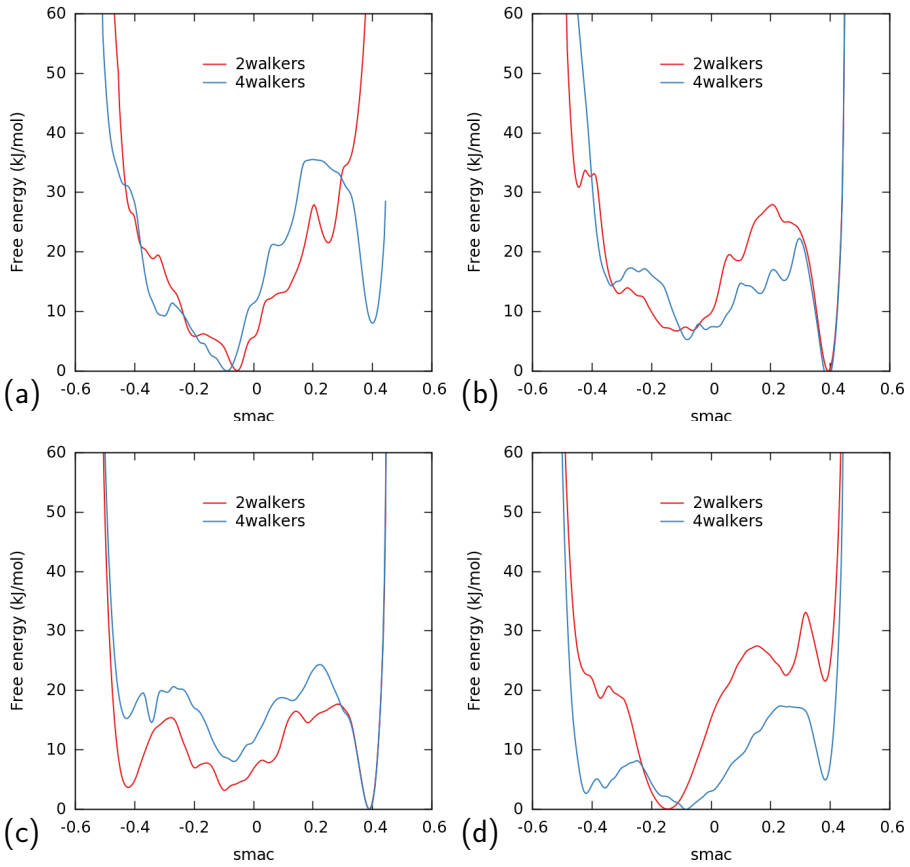

Figure 5.13.: The free energy landscape along SMAC by reweighting from the Metadynamics simulations with zangle control. (a) 300 K; (b) 400 K; (c) 450 K; (d) 500 K.

new results[1] calculated by density functional theory also support that β form is more stable than α form, and the free energy difference is 1-2 kJ/mol per monomer. It agrees qualitatively with our results from Metadynamics.

Moreover, during Metadynamics, we observe many metastable phases (Figure 5.14) which are not sampled in parallel tempering methods. (a)(b) show two β forms, which correspond to β'' and β' reported in experimental work [68, 78]. These are never observed in Parallel tempering simulations, instead, a β-like form is stable during the simulations (Figure 3.5(c)). (c)(d) show two α forms, which are also different from the one obtained in Parallel tempering simulations (Figure 3.3(b)). The triplets of α from are in the same directions during PT simulations, while in Metadynamics simulations, different directions of the triplets are observed. Considering the chain number in this Metadynamics simulation is 12, not a multiple of 9 (chain number in α unit cell), which make it difficult to identify the resulting configurations belong to α' or α''. From Metadynamics, we also found some interesting phases shown in (e)(f), which is not α or β forms, but also exbihits a long-range order, unlike normal mixture phases. All these phases are observed when checking the trajectories, and they are still undistinguishable in CV-space. In our future work, it will be intereting to find a way to further differ them and thus be able to assess their relative stabilities.

In addition, it is unclear that in metadynamics, whether the size and the chain number will affect the sampling of different forms and the real free energy reconstruction. We also attempt to perform large systems with 36 chains or 72 chains, but it is computationally expensive and far from convergence by now. Moreover, in large systems, the barriers are much higher than small systems ($\sim$100 kJ/mol in 36 chains and $\sim$200 kJ/mol in 72 chains), which makes the simulations much more difficult to converge.

[1] data is supported by Jan Gerit Brandenburg from Heidelberg University, unpublished.

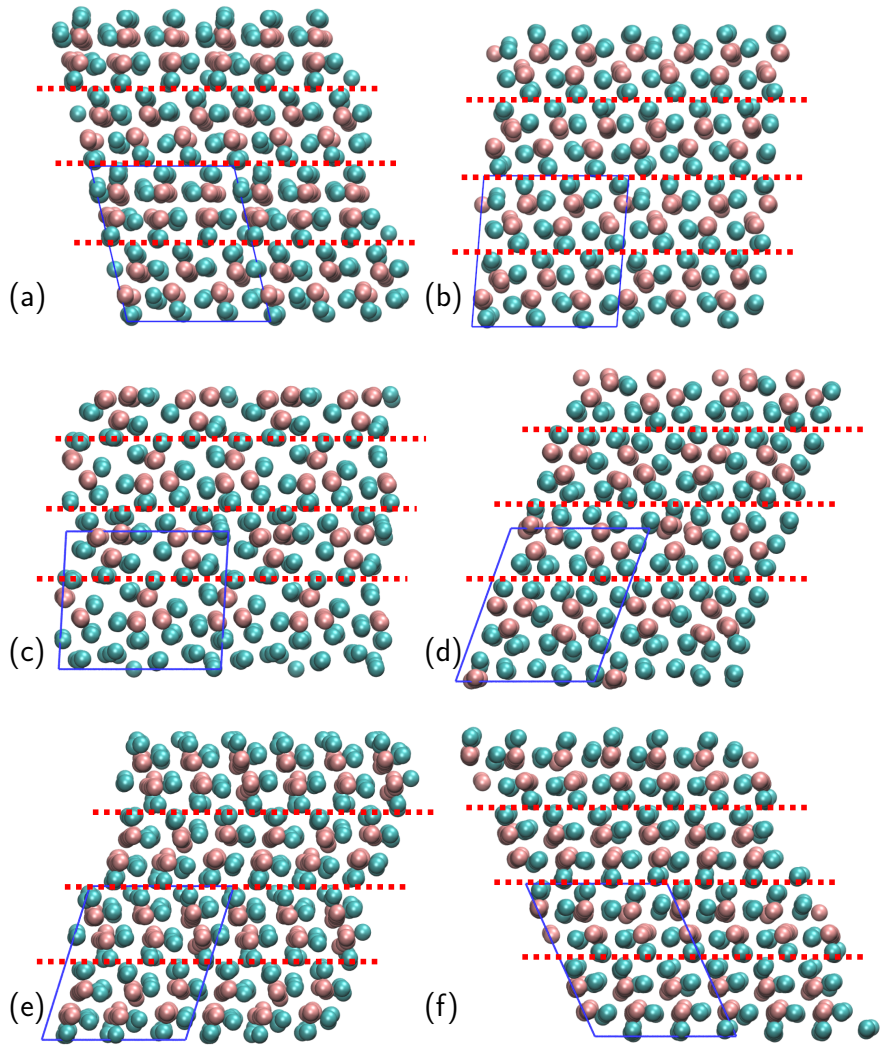

Figure 5.14.: six snapshots from Metadynamics. New metastable phases are observed.

6. Conclusions

In this thesis, we focus on using Molecular Dynamics simulations to study crystallization process and the relative stability of the polymorphs for syndiotactic polystyrene (sPS). Several simulations studies have been performed for understanding the nanoporous cavity structures and sorption of small molecules, which is more related to δ form or other helical forms. These simulations with atomistic (AA) model can only reach several nanoseconds and cannot observe self-assembly and spontaneous polymorph interconversion. This is the first attempt to employ coarse-grained (CG) model to study the polymorphism of sPS.

This CG model is derived by conditional reversible work (CRW) method, and has been validated for melt properties in Fritz work [42]. In this work, we firstly performed annealing simulations with this CG model to confirm that the system with this model can crystallize. Due to hysteretic behavior in annealing simulations, parallel tempering molecular dynamics simulations were then performed to obtain the melting curves of sPS. The CG simulations yield a transition temperature in remarkable agreement with the AA model. Furthermore, we find that the CG model stabilizes the main polymorphs α and β, while the δ form was not observed due to the lack of solvent. These results are in qualitative agreement with experiments. Although no uniform results are obtained from different simulations due to the finite-size effects and limited pressure coupling, we observed a kinetic-trap behavior of α form in specific box shapes, which is consistent with experimental results. We thus show that CG models are powerful tools to investigate the polymorphic behavior of polymers. This CG model derived from atomistic simulations in vacuum not only reproduces melt properties, but also transfers to the crystals. The choices of mapping scheme and force field are important to stabilize and distinguish the main polymorphs. In spite of remaining shortcomings, the ability of the CG model (without additional tuning) to reproduce the crystallization transition and polymorphism of polymer is remarkable.

Because the CG model can markedly speed up the simulations, it was then used to simulate significantly larger systems, which was expected better suited to study crystallization without finite-size effects. However, the obvious limitation of parallel tempering methods were observed in large systems. Hence another enhanced-sampling method, metadynamics, was considered to yield further insight into the thermodynamics of interconversion between polymorphs. This method, unlike parallel tempering, relies on collective variable (CV) biasing, which requires the preliminary identification of a set of CVs. An appropriate choice for CVs is necessary to analyze the nature of these metastable phases and the

transitions among them. However, there is no a priori instruction for finding the proper set of CVs. We identify the combination of two such CVs, SMAC and polymer angle, which satisfies basic requirements and drives the system to overcome the barriers between these metastable phases. Free energy landscapes then were reconstructed by reweighting methods. From the free energy landscape along SMAC, we can conclude that β form is at the global minimum, i.e., more stable than α form. Besides, the largest barrier also lies between β form and mixture phases, while the barrier between α and mixture phases are much smaller. This can further explain the kinetic-trap behavior of α form in experiments. Furthermore, with Metadynamics, we observe the exact β' and β'' forms which were reported in experiments but not found in parallel tempering simulations. These results help demonstrate that Metadynamics are a powerful tool to study polymorphism of sPS.

However, Metadynamics simulations are still expensive for large systems. In future work, we may consider other extended methods to speed up the convergence of simulations or use Markov State Models to further explore the detailed transition path among these phases.

A. Backmapping Procedure

Backmapping or "inverse mapping" is the term used to describe the re-introduction of atomistic detail into a given CG structure. In general, there is no unique solution to the task of finding a set of atomistic coordinates, whose mapping points coincide with the CG target structure, since every CG structure corresponds to an ensemble of atomistic microstates.

In early attempts for backmapping [127, 128], the general strategy was to use reasonably pre-sampled atomistic chain fragments to fit a single or a small set of CG beads. Then constructing these monomers (or beads) one by one until the end of chain. In this process, only geometric criteria are used, no force and potential energy calculations are involved. Then the resulting atomistic structure was relaxed by energy minimization and a short equilibration. In many cases, this strategy can easily work, especially for the polymer melts in equilibrium.

In some other cases, for example crystals (or liquid crystals) or some non-equilibrium system, the CG conformation needs to be strictly retained in the atomistic picture. If the CG polymer chains have very flexible units or if the CG structure includes small molecules, the atomistic structures may diffuse away from the CG target coordinates even in a very short equilibration time. The underlying reason is that the pre-sampled atomistic coordinates do not truly correspond to the parent CG conformation. The strategy in these cases is to constrain the atomistic coordinates to always satisfy the "mapping condition" [129, 130]. The resulting structures are relaxed with the restraint to make sure that the set of atomistic coordinated exactly reproduces the CG structure and also in a perfect equilibration.

In GROMACS [20], the constraints can be achieved by "virtual site restraining", i.e., an additional harmonic position-restraining potential is acting on groups of atoms during the relaxation simulation:

$$U_{\mathrm{pr}} = \frac{1}{2} k_{\mathrm{pr}} (\sum_i \mathbf{r}_i - \mathbf{R})^2. \tag{A.1}$$

In Peter's work [129], all atoms were constrained but the bond and bonded potentials was sequentially turned on through various steps of energy minimization, while Chen [130] turn on all potentials in the beginning, but set various partial position-restraint during the procedure until energy converges.

In our work, a similar way to Chen was performed. In the beginning, we equilibrated

the atomistic configuration for each isolated chain, with a weak constraint on the sets of atomistic coordinations corresponding to bead A. Then we constrained all atoms, still with a weak potential. After it, we strengthened the constraints. In the end, we performed energy minimum for total system with all constraints. With this procedure, we can use an initial atomistic configuration that was far from the target one. With this backmapping procedure, we can obtain the crystalline structures from CG simulation, which is hard to be generated in atomistic simulations. Then we can perform atomistic simulations starting from the crystalline structures to further assess the transferability of the CG model (See Chapter 2).

B. Form Distinguish Procedure

In analogy to the order parameter, form characterization in both AA and CG simulations is based on conformations at the CG level, and we take two monomers as one characterizing unit.

There are two types of single-chain conformations (see Figure B.1): trans-planar chains (α and β) and helical chains (γ, δ and ε). First, we identify these two different crystalline chain conformations from amorphous chains. In a polymer chain, for unit i, we identify a backbone vector $\mathbf{b}_i$ which points from bead A_2^i to bead A_1^i. When the angle between vector $\mathbf{b}_i$ and vector $\mathbf{b}_{i+1}$ is around 0°, the unit i and $i+1$ are trans-planar chain segments (see Figure B.1 (a)). When the angle between vector $\mathbf{b}_i$ and vector $\mathbf{b}_{i+1}$ is around 70° and the angle between vector $\mathbf{b'}_i$ (from bead A_1^{i+1} to bead A_2^i) and vector $\mathbf{b}_i$ is around 25°, the unit i and $i+1$ are helical chain segments (see Figure B.1 (b)). The remaining segments are considered amorphous.

For trans-planar chain segments, we discriminate crystal regions between different chain-stretching directions. Then in each region and each single layer, which is perpendicular to the chain stretching direction, we measure the distances between all beads of type A in the same layer. When the distances between two such beads is smaller than 0.6 nm, we associate them into the same group. In each group, we measure the orientations of side chains to identify α and β forms (see Figure B.1 (c) and (d)). If the orientations are all parallel, the group is a "full β" group; if the angles of the orientations are all around 120°, the group is a "full α" group. Some groups have features of both α and β forms, in which case we call them "mix" (see Figure 3.4). In case only a single characterizing unit is found in the group, we call it "defect".

In this work, we focus on the main α and β polymorphs found in annealing experiments, while all helical chain segments are herein called δ for convenience.

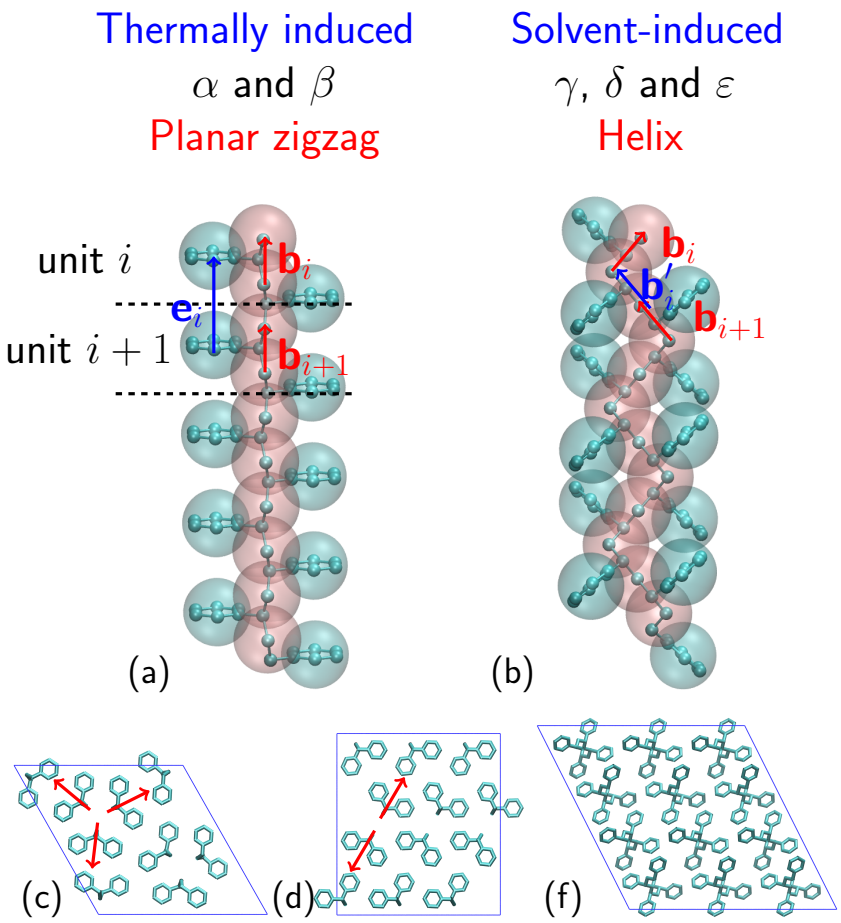

Figure B.1.: The procedure to distinguish the different chain conformations: (a) trans-planar chain and (b) helical chain, and the different transversal surfaces: (c) α form; (d) β form; (f) δ form.

List of Figures

List of Tables

Acknowledgments

Bibliography

[1] S. L. Price. “From crystal structure prediction to polymorph prediction: interpreting the crystal energy landscape”. In: *Physical Chemistry Chemical Physics* 10.15 (2008), pp. 1996–2009 (cit. on pp. 1, 28).

[2] S. L. Price. “Why don’t we find more polymorphs?” In: *Acta Crystallographica Section B: Structural Science, Crystal Engineering and Materials* 69.4 (2013), pp. 313–328 (cit. on pp. 1, 28).

[3] A. M. Reilly and A. Tkatchenko. “Role of dispersion interactions in the polymorphism and entropic stabilization of the aspirin crystal”. In: *Phys. Rev. Lett.* 113.5 (2014), p. 055701 (cit. on pp. 1, 28).

[4] H. J. Berendsen. *Simulating the physical world: hierarchical modeling from quantum mechanics to fluid dynamics*. Cambridge University Press, 2007 (cit. on pp. 1–3, 6, 8, 9, 23).

[5] J. W. Gibbs. *The collected works of J. Willard Gibbs*. Tech. rep. Yale Univ. Press, 1948 (cit. on pp. 2, 5).

[6] H. Goldstein. “Classical mechanics”. In: (1980) (cit. on p. 2).

[7] L. Landau and E. Lifshitz. *Mechanics, 3rd English edn.* 1982 (cit. on p. 2).

[8] C. E. Shannon. “A mathematical theory of communication”. In: *Bell system technical journal* 27.3 (1948), pp. 379–423 (cit. on p. 6).

[9] M. Aliabadi and D. Rooke. “Numerical Fracture Mechanics Kluwer Academic Publishers”. In: *Dordrecht, The Netherlands* (1991) (cit. on p. 9).

[10] F. Cleri, S. R. Phillpot, D. Wolf, and S. Yip. “Atomistic simulations of materials fracture and the link between atomic and continuum length scales”. In: *Journal of the American Ceramic Society* 81.3 (1998), pp. 501–516 (cit. on p. 9).

[11] F. Müller-Plathe. “Coarse-graining in polymer simulation: from the atomistic to the mesoscopic scale and back”. In: *ChemPhysChem* 3.9 (2002), pp. 754–769 (cit. on pp. 9, 10).

[12] T. D. de la Rubia and V. V. Bulatov. “Materials research by means of multiscale computer simulation”. In: *MRS bulletin* 26.3 (2001), pp. 169–175 (cit. on p. 9).

[13] K. Kremer and F. Müller-Plathe. “Multiscale problems in polymer science: simulation approaches”. In: *MRS bulletin* 26.3 (2001), pp. 205–210 (cit. on p. 9).

[14] C. Peter and K. Kremer. “Multiscale simulation of soft matter systems”. In: *Faraday Discuss.* 144 (2010), pp. 9–24 (cit. on p. 9).

[15] D. Frenkel and B. Smit. *Understanding molecular simulation: From algorithms to applications*. 2002 (cit. on p. 10).

[16] J. Meiss. “Symplectic maps, variational principles, and transport”. In: *Reviews of Modern Physics* 64.3 (1992), p. 795 (cit. on p. 12).

[17] S. K. Gray, D. W. Noid, and B. G. Sumpter. “Symplectic integrators for large scale molecular dynamics simulations: A comparison of several explicit methods”. In: *The Journal of chemical physics* 101.5 (1994), pp. 4062–4072 (cit. on p. 12).

[18] L. Verlet. “Computer” experiments” on classical fluids. I. Thermodynamical properties of Lennard-Jones molecules”. In: *Physical review* 159.1 (1967), p. 98 (cit. on p. 12).

[19] R. W. Hockney and J. W. Eastwood. *Computer simulation using particles*. crc Press, 1988 (cit. on p. 13).

[20] B. Hess, C. Kutzner, D. Van Der Spoel, and E. Lindahl. “GROMACS 4: algorithms for highly efficient, load-balanced, and scalable molecular simulation”. In: *J. Chem. Theory Comput.* 4.3 (2008), pp. 435–447 (cit. on pp. 13, 41, 103).

[21] W. C. Swope, H. C. Andersen, P. H. Berens, and K. R. Wilson. “A computer simulation method for the calculation of equilibrium constants for the formation of physical clusters of molecules: Application to small water clusters”. In: *The Journal of Chemical Physics* 76.1 (1982), pp. 637–649 (cit. on p. 13).

[22] H. C. Andersen. “Molecular dynamics simulations at constant pressure and/or temperature”. In: *The Journal of chemical physics* 72.4 (1980), pp. 2384–2393 (cit. on p. 14).

[23] S. Nosé. “A unified formulation of the constant temperature molecular dynamics methods”. In: *The Journal of chemical physics* 81.1 (1984), pp. 511–519 (cit. on p. 14).

[24] W. G. Hoover. “Canonical dynamics: Equilibrium phase-space distributions”. In: *Physical review A* 31.3 (1985), p. 1695 (cit. on p. 15).

[25] H. J. Berendsen, J. v. Postma, W. F. van Gunsteren, A. DiNola, and J. Haak. “Molecular dynamics with coupling to an external bath”. In: *J. Chem. Phys.* 81.8 (1984), pp. 3684–3690 (cit. on p. 15).

[26] M. Parrinello and A. Rahman. “Polymorphic transitions in single crystals: A new molecular dynamics method”. In: *Journal of Applied physics* 52.12 (1981), pp. 7182–7190 (cit. on p. 15).

[27] G. A. Voth. *Coarse-graining of condensed phase and biomolecular systems*. CRC press, 2008 (cit. on p. 16).

[28] W. Noid. “Systematic methods for structurally consistent coarse-grained models”. In: *Biomolecular Simulations*. Springer, 2013, pp. 487–531 (cit. on p. 17).

[29] W. Noid. “Perspective: Coarse-grained models for biomolecular systems”. In: *The Journal of chemical physics* 139.9 (2013), 09B201_1 (cit. on p. 17).

[30] J. F. Rudzinski and W. Noid. “Coarse-graining entropy, forces, and structures”. In: *The Journal of chemical physics* 135.21 (2011), p. 214101 (cit. on p. 17).

[31] J. F. Rudzinski and W. G. Noid. “The role of many-body correlations in determining potentials for coarse-grained models of equilibrium structure”. In: *The Journal of Physical Chemistry B* 116.29 (2012), pp. 8621–8635 (cit. on p. 18).

[32] C. R. Ellis, J. F. Rudzinski, and W. G. Noid. “Generalized-Yvon–Born–Green Model of Toluene”. In: *Macromolecular Theory and Simulations* 20.7 (2011), pp. 478–495 (cit. on p. 18).

[33] R. Henderson. “A uniqueness theorem for fluid pair correlation functions”. In: *Physics Letters A* 49.3 (1974), pp. 197–198 (cit. on p. 18).

[34] W Tschöp, K. Kremer, J Batoulis, T. Bürger, and O Hahn. “Simulation of polymer melts. I. Coarse-graining procedure for polycarbonates”. In: *Acta Polymerica* 49.2-3 (1998), pp. 61–74 (cit. on p. 19).

[35] D. Reith, M. Pütz, and F. Müller-Plathe. “Deriving effective mesoscale potentials from atomistic simulations”. In: *Journal of computational chemistry* 24.13 (2003), pp. 1624–1636 (cit. on p. 19).

[36] F. Ercolessi and J. B. Adams. “Interatomic potentials from first-principles calculations: the force-matching method”. In: *EPL (Europhysics Letters)* 26.8 (1994), p. 583 (cit. on p. 19).

[37] S. Izvekov and G. A. Voth. “Multiscale coarse graining of liquid-state systems”. In: *The Journal of chemical physics* 123.13 (2005), p. 134105 (cit. on p. 19).

[38] S. Izvekov and G. A. Voth. “A multiscale coarse-graining method for biomolecular systems”. In: *The Journal of Physical Chemistry B* 109.7 (2005), pp. 2469–2473 (cit. on p. 19).

[39] W. Noid, P. Liu, Y. Wang, J.-W. Chu, G. S. Ayton, S. Izvekov, H. C. Andersen, and G. A. Voth. “The multiscale coarse-graining method. II. Numerical implementation for coarse-grained molecular models”. In: *The Journal of chemical physics* 128.24 (2008), p. 244115 (cit. on p. 20).

[40] W. Noid, J.-W. Chu, G. S. Ayton, and G. A. Voth. “Multiscale coarse-graining and structural correlations: Connections to liquid-state theory”. In: *The Journal of Physical Chemistry B* 111.16 (2007), pp. 4116–4127 (cit. on p. 20).

[41] E. Brini, E. A. Algaer, P. Ganguly, C. Li, F. Rodríguez-Ropero, and N. F. van der Vegt. “Systematic coarse-graining methods for soft matter simulations–a review”. In: *Soft Matter* 9.7 (2013), pp. 2108–2119 (cit. on pp. 21, 22).

[42] D. Fritz, V. A. Harmandaris, K. Kremer, and N. F. van der Vegt. "Coarse-grained polymer melts based on isolated atomistic chains: simulation of polystyrene of different tacticities". In: *Macromolecules* 42.19 (2009), pp. 7579–7588 (cit. on pp. 21, 22, 36–38, 41, 43, 45, 101).

[43] E. Brini, V. Marcon, and N. F. van der Vegt. "Conditional reversible work method for molecular coarse graining applications". In: *Phys. Chem. Chem. Phys.* 13.22 (2011), pp. 10468–10474 (cit. on pp. 21, 22, 36, 40).

[44] J. D. McCoy and J. G. Curro. "Mapping of explicit atom onto united atom potentials". In: *Macromolecules* 31.26 (1998), pp. 9362–9368 (cit. on p. 22).

[45] H. Fukunaga, J.-i. Takimoto, and M. Doi. "A coarse-graining procedure for flexible polymer chains with bonded and nonbonded interactions". In: *The Journal of chemical physics* 116.18 (2002), pp. 8183–8190 (cit. on p. 22).

[46] S. Kirkpatrick, C. D. Gelatt, and M. P. Vecchi. "Optimization by simulated annealing". In: *science* 220.4598 (1983), pp. 671–680 (cit. on p. 23).

[47] U. H. Hansmann. "Parallel tempering algorithm for conformational studies of biological molecules". In: *Chemical Physics Letters* 281.1-3 (1997), pp. 140–150 (cit. on pp. 23, 42).

[48] Y. Sugita and Y. Okamoto. "Replica-exchange molecular dynamics method for protein folding". In: *Chem. Phys. Lett.* 314.1-2 (1999), pp. 141–151 (cit. on p. 23).

[49] Y. Sugita and Y. Okamoto. "Replica-exchange multicanonical algorithm and multicanonical replica-exchange method for simulating systems with rough energy landscape". In: *Chemical Physics Letters* 329.3-4 (2000), pp. 261–270 (cit. on p. 24).

[50] D. M. Zuckerman and E. Lyman. "A second look at canonical sampling of biomolecules using replica exchange simulation". In: *Journal of chemical theory and computation* 2.4 (2006), pp. 1200–1202 (cit. on pp. 24, 62).

[51] J. G. Kirkwood. "Statistical mechanics of fluid mixtures". In: *The Journal of Chemical Physics* 3.5 (1935), pp. 300–313 (cit. on p. 24).

[52] O. Valsson, P. Tiwary, and M. Parrinello. "Enhancing important fluctuations: Rare events and metadynamics from a conceptual viewpoint". In: *Annual review of physical chemistry* 67 (2016), pp. 159–184 (cit. on p. 25).

[53] G. M. Torrie and J. P. Valleau. "Nonphysical sampling distributions in Monte Carlo free-energy estimation: Umbrella sampling". In: *Journal of Computational Physics* 23.2 (1977), pp. 187–199 (cit. on p. 25).

[54] S. Kumar, J. M. Rosenberg, D. Bouzida, R. H. Swendsen, and P. A. Kollman. "The weighted histogram analysis method for free-energy calculations on biomolecules. I. The method". In: *Journal of computational chemistry* 13.8 (1992), pp. 1011–1021 (cit. on p. 25).

[55] A. Laio and M. Parrinello. “Escaping free-energy minima”. In: *Proceedings of the National Academy of Sciences* 99.20 (2002), pp. 12562–12566 (cit. on pp. 25, 63, 81).

[56] A. Barducci, M. Bonomi, and M. Parrinello. “Metadynamics”. In: *Wiley Interdisciplinary Reviews: Computational Molecular Science* 1.5 (2011), pp. 826–843 (cit. on pp. 25, 63, 81).

[57] C. Abrams and G. Bussi. “Enhanced sampling in molecular dynamics using metadynamics, replica-exchange, and temperature-acceleration”. In: *Entropy* 16.1 (2014), pp. 163–199 (cit. on pp. 26, 62).

[58] A. Barducci, G. Bussi, and M. Parrinello. “Well-tempered metadynamics: a smoothly converging and tunable free-energy method”. In: *Physical review letters* 100.2 (2008), p. 020603 (cit. on pp. 26, 82).

[59] J. F. Dama, M. Parrinello, and G. A. Voth. “Well-tempered metadynamics converges asymptotically”. In: *Physical review letters* 112.24 (2014), p. 240602 (cit. on p. 26).

[60] P. Tiwary and M. Parrinello. “A time-independent free energy estimator for metadynamics”. In: *The Journal of Physical Chemistry B* 119.3 (2014), pp. 736–742 (cit. on pp. 27, 83, 90).

[61] D. Polino and M. Parrinello. “Combustion chemistry via metadynamics: Benzyl decomposition revisited”. In: *The Journal of Physical Chemistry A* 119.6 (2015), pp. 978–989 (cit. on p. 27).

[62] F. Doro, G. Saladino, L. Belvisi, M. Civera, and F. L. Gervasio. “New insights into the molecular mechanism of E-cadherin-mediated cell adhesion by free energy calculations”. In: *Journal of chemical theory and computation* 11.4 (2015), pp. 1354–1359 (cit. on p. 27).

[63] J. Iglesias-Fernández, L. Raich, A. Ardèvol, and C. Rovira. “The complete conformational free energy landscape of β-xylose reveals a two-fold catalytic itinerary for β-xylanases”. In: *Chemical science* 6.2 (2015), pp. 1167–1177 (cit. on p. 27).

[64] C De Rosa, G Guerra, V Petraccone, and P Corradini. “Crystal structure of the α-form of syndiotactic polystyrene”. In: *Polym. J.* 23.12 (1991), p. 1435 (cit. on pp. 28, 53).

[65] P. Corradini, C. De Rosa, G. Guerra, R. Napolitano, V. Petraccone, and B. Pirozzi. “Conformational and packing energy of the crystalline α modification of syndiotactic polystyrene”. In: *Eur. Polym. J.* 30.10 (1994), pp. 1173–1177 (cit. on p. 28).

[66] C. De Rosa. “Crystal structure of the trigonal modification (α form) of syndiotactic polystyrene”. In: *Macromolecules* 29.26 (1996), pp. 8460–8465 (cit. on pp. 28, 49, 51).

[67] L. Cartier, T. Okihara, and B. Lotz. "The α ""Superstructure" of Syndiotactic Polystyrene: A Frustrated Structure". In: *Macromolecules* 31.10 (1998), pp. 3303–3310 (cit. on p. 28).

[68] C De Rosa, M Rapacciuolo, G Guerra, V Petraccone, and P Corradini. "On the crystal structure of the orthorhombic form of syndiotactic polystyrene". In: *Polymer* 33.7 (1992), pp. 1423–1428 (cit. on pp. 28, 53, 99).

[69] Y. Chatani, Y. Shimane, T. Ijitsu, and T. Yukinari. "Structural study on syndiotactic polystyrene: 3. Crystal structure of planar form I". In: *Polymer* 34.8 (1993), pp. 1625–1629 (cit. on pp. 28, 49, 55).

[70] P. Rizzo, M. Lamberti, A. R. Albunia, O. Ruiz de Ballesteros, and G. Guerra. "Crystalline orientation in syndiotactic polystyrene cast films". In: *Macromolecules* 35.15 (2002), pp. 5854–5860 (cit. on p. 28).

[71] P. Rizzo, A. R. Albunia, and G. Guerra. "Polymorphism of syndiotactic polystyrene: γ phase crystallization induced by bulky non-guest solvents". In: *Polymer* 46.23 (2005), pp. 9549–9554 (cit. on p. 28).

[72] C. De Rosa, G. Guerra, V. Petraccone, and B. Pirozzi. "Crystal structure of the emptied clathrate form (δe form) of syndiotactic polystyrene". In: *Macromolecules* 30.14 (1997), pp. 4147–4152 (cit. on pp. 28, 49).

[73] G. Milano, V. Venditto, G. Guerra, L. Cavallo, P. Ciambelli, and D. Sannino. "Shape and volume of cavities in thermoplastic molecular sieves based on syndiotactic polystyrene". In: *Chem. Mater.* 13.5 (2001), pp. 1506–1511 (cit. on p. 28).

[74] E. B. Gowd, N. Shibayama, and K. Tashiro. "Structural changes in thermally induced phase transitions of uniaxially oriented δe form of syndiotactic polystyrene investigated by temperature-dependent measurements of X-ray fiber diagrams and polarized infrared spectra". In: *Macromolecules* 39.24 (2006), pp. 8412–8418 (cit. on p. 28).

[75] P. Rizzo, C. D'Aniello, A. De Girolamo Del Mauro, and G. Guerra. "Thermal transitions of ε crystalline phases of syndiotactic polystyrene". In: *Macromolecules* 40.26 (2007), pp. 9470–9474 (cit. on p. 28).

[76] V. Petraccone, O. Ruiz de Ballesteros, O. Tarallo, P. Rizzo, and G. Guerra. "Nanoporous polymer crystals with cavities and channels". In: *Chem. Mater.* 20.11 (2008), pp. 3663–3668 (cit. on p. 28).

[77] O. Tarallo, M. M. Schiavone, V. Petraccone, C. Daniel, P. Rizzo, and G. Guerra. "Channel clathrate of syndiotactic polystyrene with p-nitroaniline". In: *Macromolecules* 43.3 (2010), pp. 1455–1466 (cit. on p. 28).

[78] G. Guerra, V. M. Vitagliano, C. De Rosa, V. Petraccone, and P. Corradini. "Polymorphism in melt crystallized syndiotactic polystyrene samples". In: *Macromolecules* 23.5 (1990), pp. 1539–1544 (cit. on pp. 28, 53, 99).

[79] Y. S. Sun and E. Woo. "Relationships between polymorphic crystals and multiple melting peaks in crystalline syndiotactic polystyrene". In: *Macromolecules* 32.23 (1999), pp. 7836–7844 (cit. on pp. 28, 53, 55).

[80] E. M. Woo, Y. S. Sun, and M. L. Lee. "Crystal forms in cold-crystallized syndiotactic polystyrene". In: *Polymer* 40.15 (1999), pp. 4425–4429 (cit. on pp. 28, 53, 55).

[81] R. Lin and E. Woo. "Melting behavior and identification of polymorphic crystals in syndiotactic polystyrene". In: *Polymer* 41.1 (2000), pp. 121–131 (cit. on pp. 28, 53).

[82] Y.-S. Sun and E. M. Woo. "Morphology and crystal structure of cold-crystallized syndiotactic polystyrene". In: *Polymer* 42.5 (2001), pp. 2241–2245 (cit. on pp. 28, 53).

[83] Y. Tamai and M. Fukuda. "Nanoscale molecular cavity in crystalline polymer membranes studied by molecular dynamics simulation". In: *Polymer* 44.11 (2003), pp. 3279–3289 (cit. on p. 30).

[84] G. Milano, G. Guerra, and F. Müller-Plathe. "Anisotropic diffusion of small penetrants in the δ crystalline phase of syndiotactic polystyrene: a molecular dynamics simulation study". In: *Chem. Mater.* 14.7 (2002), pp. 2977–2982 (cit. on p. 30).

[85] Y. Tamai and M. Fukuda. "Fast one-dimensional gas transport in molecular capillary embedded in polymer crystal". In: *Chem. Phys. Lett.* 371.1-2 (2003), pp. 217–222 (cit. on p. 30).

[86] Y. Tamai and M. Fukuda. "Reorientational dynamics of aromatic molecules clathrated in δ form of crystalline syndiotactic polystyrene". In: *Chem. Phys. Lett.* 371.5-6 (2003), pp. 620–625 (cit. on p. 30).

[87] Y. Tamai, Y. Tsujita, and M. Fukuda. "Reorientational relaxation of aromatic molecules in the molecular cavity of crystalline syndiotactic polystyrene studied by molecular dynamics simulation". In: *J. Mol. Struct.* 739.1-3 (2005), pp. 33–40 (cit. on p. 30).

[88] S. Figueroa-Gerstenmaier, C. Daniel, G. Milano, G. Guerra, O. Zavorotynska, J. G. Vitillo, A. Zecchina, and G. Spoto. "Storage of hydrogen as a guest of a nanoporous polymeric crystalline phase". In: *Phys. Chem. Chem. Phys.* 12.20 (2010), pp. 5369–5374 (cit. on p. 30).

[89] S. Figueroa-Gerstenmaier, C. Daniel, G. Milano, J. G. Vitillo, O. Zavorotynska, G. Spoto, and G. Guerra. "Hydrogen Adsorption by δ and ε crystalline phases of syndiotactic polystyrene aerogels". In: *Macromolecules* 43.20 (2010), pp. 8594–8601 (cit. on p. 30).

[90] L. Sanguigno, F. Cosentino, D. Larobina, and G. Mensitieri. "Molecular simulation of carbon dioxide sorption in nanoporous crystalline phase of sydiotactic polystyrene". In: *Soft Mater.* 9.2-3 (2011), pp. 169–182 (cit. on p. 30).

[91] C. Liu, K. Kremer, and T. Bereau. "Polymorphism of syndiotactic polystyrene crystals from multiscale simulations". In: *Advanced Theory and Simulations* 1.7 (2018), p. 1800024 (cit. on pp. 31, 49).

[92] Q. Sun and R. Faller. "Systematic coarse-graining of atomistic models for simulation of polymeric systems". In: *Computers & chemical engineering* 29.11-12 (2005), pp. 2380–2385 (cit. on p. 33).

[93] G. Milano and F. Müller-Plathe. "Mapping atomistic simulations to mesoscopic models: A systematic coarse-graining procedure for vinyl polymer chains". In: *J. Phys. Chem. B* 109.39 (2005), pp. 18609–18619 (cit. on pp. 33, 34).

[94] H.-J. Qian, P. Carbone, X. Chen, H. A. Karimi-Varzaneh, C. C. Liew, and F. Müller-Plathe. "Temperature-transferable coarse-grained potentials for ethylbenzene, polystyrene, and their mixtures". In: *Macromolecules* 41.24 (2008), pp. 9919–9929 (cit. on pp. 33, 34).

[95] Q. Sun and R. Faller. "Crossover from unentangled to entangled dynamics in a systematically coarse-grained polystyrene melt". In: *Macromolecules* 39.2 (2006), pp. 812–820 (cit. on p. 33).

[96] P. Carbone, H. A. K. Varzaneh, X. Chen, and F. Müller-Plathe. "Transferability of coarse-grained force fields: The polymer case". In: *The Journal of chemical physics* 128.6 (2008), p. 064904 (cit. on p. 34).

[97] V. Harmandaris, N. Adhikari, N. F. van der Vegt, and K. Kremer. "Hierarchical modeling of polystyrene: From atomistic to coarse-grained simulations". In: *Macromolecules* 39.19 (2006), pp. 6708–6719 (cit. on pp. 35, 41).

[98] V. A. Harmandaris, D. Reith, N. F. Van der Vegt, and K. Kremer. "Comparison Between Coarse-Graining Models for Polymer Systems: Two Mapping Schemes for Polystyrene". In: *Macromol. Chem. Phys.* 208.19-20 (2007), pp. 2109–2120 (cit. on pp. 35–38, 41).

[99] G. Rossi, L. Monticelli, S. R. Puisto, I. Vattulainen, and T. Ala-Nissila. "Coarse-graining polymers with the MARTINI force-field: polystyrene as a benchmark case". In: *Soft Matter* 7.2 (2011), pp. 698–708 (cit. on pp. 36, 37).

[100] S. J. Marrink, H. J. Risselada, S. Yefimov, D. P. Tieleman, and A. H. De Vries. "The MARTINI force field: coarse grained model for biomolecular simulations". In: *The journal of physical chemistry B* 111.27 (2007), pp. 7812–7824 (cit. on pp. 36, 37).

[101] F. Müller-Plathe. "Local structure and dynamics in solvent-swollen polymers". In: *Macromolecules* 29.13 (1996), pp. 4782–4791 (cit. on p. 36).

[102] E. Brini, C. R. Herbers, G. Deichmann, and N. F. van der Vegt. "Thermodynamic transferability of coarse-grained potentials for polymer–additive systems". In: *Physical Chemistry Chemical Physics* 14.34 (2012), pp. 11896–11903 (cit. on p. 41).

[103] V. Marcon, D. Fritz, and N. F. van der Vegt. "Hierarchical modelling of polystyrene surfaces". In: *Soft Matter* 8.20 (2012), pp. 5585–5594 (cit. on p. 41).

[104] O. M. Szklarczyk, E. Arvaniti, and W. F. van Gunsteren. "Polarizable coarse-grained models for molecular dynamics simulation of liquid cyclohexane". In: *J. Comput. Chem.* 36.17 (2015), pp. 1311–1321 (cit. on p. 55).

[105] E. B. Gowd, K. Tashiro, and C Ramesh. "Structural phase transitions of syndiotactic polystyrene". In: *Progress in Polymer Science* 34.3 (2009), pp. 280–315 (cit. on p. 56).

[106] A. Laio and F. L. Gervasio. "Metadynamics: a method to simulate rare events and reconstruct the free energy in biophysics, chemistry and material science". In: *Reports on Progress in Physics* 71.12 (2008), p. 126601 (cit. on pp. 63, 64).

[107] G. A. Tribello, M. Bonomi, D. Branduardi, C. Camilloni, and G. Bussi. "PLUMED 2: New feathers for an old bird". In: *Computer Physics Communications* 185.2 (2014), pp. 604–613 (cit. on pp. 65, 82).

[108] M. J. Ko, N. Waheed, M. S. Lavine, and G. C. Rutledge. "Characterization of polyethylene crystallization from an oriented melt by molecular dynamics simulation". In: *The Journal of chemical physics* 121.6 (2004), pp. 2823–2832 (cit. on p. 66).

[109] N. Waheed, M. J. Ko, and G. Rutledge. "Molecular simulation of crystal growth in long alkanes". In: *Polymer* 46.20 (2005), pp. 8689–8702 (cit. on p. 66).

[110] G. Reiter and G. R. Strobl. *Progress in understanding of polymer crystallization*. Vol. 714. Springer, 2007 (cit. on p. 66).

[111] M. Iannuzzi, A. Laio, and M. Parrinello. "Efficient exploration of reactive potential energy surfaces using Car-Parrinello molecular dynamics". In: *Physical Review Letters* 90.23 (2003), p. 238302 (cit. on p. 69).

[112] B. Ensing, A. Laio, F. L. Gervasio, M. Parrinello, and M. L. Klein. "A minimum free energy reaction path for the E2 reaction between fluoro ethane and a fluoride ion". In: *Journal of the American Chemical Society* 126.31 (2004), pp. 9492–9493 (cit. on p. 69).

[113] G Fiorin, A Pastore, P Carloni, and M. Parrinello. "Using metadynamics to understand the mechanism of calmodulin/target recognition at atomic detail". In: *Biophysical journal* 91.8 (2006), pp. 2768–2777 (cit. on p. 69).

[114] G. Bussi, F. L. Gervasio, A. Laio, and M. Parrinello. "Free-energy landscape for β hairpin folding from combined parallel tempering and metadynamics". In: *Journal of the American Chemical Society* 128.41 (2006), pp. 13435–13441 (cit. on p. 69).

[115] S. Piana and A. Laio. "A bias-exchange approach to protein folding". In: *The journal of physical chemistry B* 111.17 (2007), pp. 4553–4559 (cit. on pp. 69, 82).

[116] P. J. Steinhardt, D. R. Nelson, and M. Ronchetti. “Icosahedral bond orientational order in supercooled liquids”. In: *Physical Review Letters* 47.18 (1981), p. 1297 (cit. on p. 71).

[117] P. J. Steinhardt, D. R. Nelson, and M. Ronchetti. “Bond-orientational order in liquids and glasses”. In: *Physical Review B* 28.2 (1983), p. 784 (cit. on p. 71).

[118] U. Gasser, E. R. Weeks, A. Schofield, P. Pusey, and D. Weitz. “Real-space imaging of nucleation and growth in colloidal crystallization”. In: *Science* 292.5515 (2001), pp. 258–262 (cit. on p. 71).

[119] M. Matsumoto, S. Saito, and I. Ohmine. “Molecular dynamics simulation of the ice nucleation and growth process leading to water freezing”. In: *Nature* 416.6879 (2002), p. 409 (cit. on p. 71).

[120] F. Trudu, D. Donadio, and M. Parrinello. “Freezing of a Lennard-Jones fluid: From nucleation to spinodal regime”. In: *Physical review letters* 97.10 (2006), p. 105701 (cit. on p. 71).

[121] F. Giberti, M. Salvalaglio, M. Mazzotti, and M. Parrinello. “Insight into the nucleation of urea crystals from the melt”. In: *Chemical Engineering Science* 121 (2015), pp. 51–59 (cit. on p. 74).

[122] F. Marinelli, F. Pietrucci, A. Laio, and S. Piana. “A kinetic model of trp-cage folding from multiple biased molecular dynamics simulations”. In: *PLoS computational biology* 5.8 (2009), e1000452 (cit. on p. 82).

[123] F. Baftizadeh, P. Cossio, F. Pietrucci, and A. Laio. “Protein folding and ligand-enzyme binding from bias-exchange metadynamics simulations”. In: *Current Physical Chemistry* 2.1 (2012), pp. 79–91 (cit. on p. 82).

[124] M. J. Abraham, T. Murtola, R. Schulz, S. Páll, J. C. Smith, B. Hess, and E. Lindahl. “GROMACS: High performance molecular simulations through multi-level parallelism from laptops to supercomputers”. In: *SoftwareX* 1 (2015), pp. 19–25 (cit. on p. 82).

[125] P. Raiteri, A. Laio, F. L. Gervasio, C. Micheletti, and M. Parrinello. “Efficient reconstruction of complex free energy landscapes by multiple walkers metadynamics”. In: *The journal of physical chemistry B* 110.8 (2006), pp. 3533–3539 (cit. on p. 83).

[126] E. M. Woo, Y.-S. Sun, and C.-P. Yang. “Polymorphism, thermal behavior, and crystal stability in syndiotactic polystyrene vs. its miscible blends”. In: *Progress in polymer science* 26.6 (2001), pp. 945–983 (cit. on p. 97).

[127] M Kotelyanskii, N. Wagner, and M. E. Paulaitis. “Building large amorphous polymer structures: Atomistic simulation of glassy polystyrene”. In: *Macromolecules* 29.26 (1996), pp. 8497–8506 (cit. on p. 103).

[128] W Tschöp, K. Kremer, O Hahn, J. Batoulis, and T Bürger. “Simulation of polymer melts. II. From coarse-grained models back to atomistic description”. In: *Acta Polymerica* 49.2-3 (1998), pp. 75–79 (cit. on p. 103).

[129] C. Peter, L. Delle Site, and K. Kremer. “Classical simulations from the atomistic to the mesoscale and back: coarse graining an azobenzene liquid crystal”. In: *Soft Matter* 4.4 (2008), pp. 859–869 (cit. on p. 103).

[130] X. Chen, P. Carbone, G. Santangelo, A. Di Matteo, G. Milano, and F. Müller-Plathe. “Backmapping coarse-grained polymer models under sheared nonequilibrium conditions”. In: *Physical Chemistry Chemical Physics* 11.12 (2009), pp. 1977–1988 (cit. on p. 103).